

12-2014

Variations in $\text{Fe}^{3+}/\Sigma\text{Fe}$ of Mariana Arc Basalts and Mantle Wedge $f\text{O}_2$

M. N. Brounce

K. A. Kelley

University of Rhode Island, kelley@uri.edu

E. Cottrell

Follow this and additional works at: <https://digitalcommons.uri.edu/gsofacpubs>

The University of Rhode Island Faculty have made this article openly available.
Please let us know how Open Access to this research benefits you.

This is a pre-publication author manuscript of the final, published article.

Terms of Use

This article is made available under the terms and conditions applicable towards Open Access Policy Articles, as set forth in our [Terms of Use](#).

Citation/Publisher Attribution

M. N. Brounce, K. A. Kelley and E. Cottrell. (2014). "Variations in $\text{Fe}^{3+}/\Sigma\text{Fe}$ of Mariana Arc Basalts and Mantle Wedge $f\text{O}_2$." *Journal of Petrology*. 55(12): 2513-2536.

Available at: <https://doi.org/10.1093/petrology/egu065>

This Article is brought to you for free and open access by the Graduate School of Oceanography at DigitalCommons@URI. It has been accepted for inclusion in Graduate School of Oceanography Faculty Publications by an authorized administrator of DigitalCommons@URI. For more information, please contact digitalcommons@etal.uri.edu.

Variations in $\text{Fe}^{3+}/\Sigma\text{Fe}$ of Mariana Arc basalts and mantle wedge $f\text{O}_2$

M.N. Brounce^{1,2*}, K.A. Kelley¹ and E. Cottrell²

¹Graduate School of Oceanography, University of Rhode Island, Narragansett Bay Campus, Narragansett, RI 02882, USA

²Department of Mineral Sciences, Smithsonian Institution, National Museum of Natural History, Washington, DC 20560, USA

*Corresponding author: Telephone (401) 674-6010. Fax: (401) 874-6811. E-mail: mbrounce@my.uri.edu

ABSTRACT

Arc basalts are more oxidized than mid-ocean ridge basalts, but it is unclear whether this difference is due to differentiation processes in the Earth's crust or to a fundamental difference in the oxygen fugacity of their mantle sources. Distinguishing between these two hypotheses is important for understanding redox-sensitive processes related to arc magmatism, and thus more broadly how Earth materials cycle globally. We present major, volatile, and trace element concentrations in combination with $\text{Fe}^{3+}/\Sigma\text{Fe}$ ratios determined in olivine-hosted glass inclusions and submarine glasses from five Mariana arc volcanoes and two regions of the Mariana trough. For individual eruptions, $\text{Fe}^{3+}/\Sigma\text{Fe}$ ratios vary along liquid lines of descent that are either slightly oxidizing (olivine + clinopyroxene + plagioclase fractionation, $\text{CO}_2 \pm \text{H}_2\text{O}$ degassing) or reducing (olivine + clinopyroxene + plagioclase \pm magnetite fractionation, $\text{CO}_2 + \text{H}_2\text{O} + \text{S}$ degassing). Mariana samples are consistent with a global relationship between calc-alkaline affinity and both magmatic H_2O and magmatic oxygen fugacity, where wetter, higher oxygen fugacity magmas display greater affinity for calc-alkaline differentiation. We find, however, that low-pressure differentiation cannot explain the majority of variations observed in $\text{Fe}^{3+}/\Sigma\text{Fe}$ ratios for Mariana arc basalts, requiring primary differences in magmatic oxygen fugacity. Calculated oxygen fugacities of primary mantle melts at the pressures and temperatures of melt segregation

are significantly oxidized over mid-ocean ridge basalts (\sim QFM), ranging from QFM+1.0 – QFM+1.6 for Mariana arc basalts, while back-arc related samples record primary oxygen fugacities that range from QFM+0.1 – QFM+0.5. This Mariana arc sample suite comprises a diversity of subduction influences, from lesser influence of a homogeneous H₂O-rich component in the back-arc, to sediment melt- and fluid-dominated influences along the arc. Primary melt oxygen fugacity does not correlate significantly with sediment melt contributions (e.g., Th/La), nor can it be attributed to previous melt extraction in the back-arc. Primary melt oxygen fugacity correlates strongly with indices of slab fluids (e.g., Ba/La) from the Mariana trough through the Mariana arc, increasing by 1.5 orders of magnitude as Ba/La increases by a factor of 10 over mid-ocean ridge basalts. These results suggest that contributions from the slab to the mantle wedge may be responsible for the elevated oxygen fugacity recorded by Mariana arc basalts and that slab fluids are potentially very oxidized.

Key words: differentiation; Mariana arc; melt inclusions; oxygen fugacity; redox; subduction

INTRODUCTION

Oxygen fugacity ($f\text{O}_2$) is a fundamental thermodynamic property that governs reduction-oxidation (redox) equilibria in solid Earth systems. It controls material transfer from the interior to the exterior of the Earth by setting the speciation of multi-valent elements (e.g., Fe, S, V, C), which in turn controls their crystal/melt partitioning behaviors (e.g., Canil, 2002), their physical state and mobility in the mantle (e.g., Rohrbach & Schmidt, 2011), and their solubility in silicate melts (e.g., Jugo *et al.*, 2010). Despite its power in dictating chemical exchange in the Earth however, the $f\text{O}_2$ of the upper mantle and whether it varies through space and geologic time is

widely debated (e.g., Ballhaus, 1993, Bezos & Humler, 2005, Bryndzia & Wood, 1990, Carmichael, 1991, Christie *et al.*, 1986, Cottrell & Kelley, 2011, Cottrell & Kelley, 2013, Kelley & Cottrell, 2009, Kelley & Cottrell, 2012, Lee *et al.*, 2005, Lee *et al.*, 2012, Lee *et al.*, 2010, Parkinson & Arculus, 1999, Rowe *et al.*, 2009, Trail *et al.*, 2011, Wood *et al.*, 1990).

Oceanic crust ages and oxidizes as it moves from spreading centers to subduction zones, where it is recycled into the mantle, and material from the down-going slab contributes chemically to the mantle source of arc magmas (e.g., Alt & Teagle, 2003, Elliott *et al.*, 1997, Lecuyer & Ricard, 1999, Plank & Langmuir, 1993). Arc basalts have a higher proportion of oxidized (Fe^{3+}) relative to reduced (Fe^{2+}) iron, expressed as the $\text{Fe}^{3+}/\Sigma\text{Fe}$ ratio (i.e., $\text{Fe}^{3+}/[\text{Fe}^{2+}+\text{Fe}^{3+}]$), than do MORB (Carmichael, 1991). There is disagreement as to whether this arises due to differentiation processes (e.g., crystal fractionation, crustal assimilation, degassing) in the arc crust or to differences in the $f\text{O}_2$ of the mantle source. Experimentally calibrated trace element proxies for mantle $f\text{O}_2$, which are potentially more immune to differentiation processes in the arc crust, suggest that the $f\text{O}_2$ of arc mantle is similar to the MORB primary magmas (Lee *et al.*, 2005, Lee *et al.*, 2012, Lee *et al.*, 2010). Magmatic oxidation may perhaps be influenced by later stage crustal processes, such as the extensive fractionation of Fe^{2+} -bearing minerals (e.g., olivine) or by the assimilation of oxidized crustal material, although such relationships have not yet been observed or quantitatively modeled.

Yet, a global study of basaltic glasses shows that those magmas most heavily influenced by subduction have higher $\text{Fe}^{3+}/\Sigma\text{Fe}$ ratios than MORB (Kelley & Cottrell, 2009). Moreover, olivine-hosted melt inclusions from a single eruptive event from Agrigan volcano in the Marianas show that the least differentiated melts have the highest $\text{Fe}^{3+}/\Sigma\text{Fe}$ ratios, and the $\text{Fe}^{3+}/\Sigma\text{Fe}$ ratios of reconstructed primary melts correspond to a source mantle that is oxidized 1 –

1.6 orders of magnitude over the MORB source (Kelley & Cottrell, 2012). In addition, a paired study of whole rock $\text{Fe}^{3+}/\Sigma\text{Fe}$ ratios determined by wet chemical methods and $f\text{O}_2$ calculated from magnetite-ilmenite mineral pairs demonstrates that andesites from the Mexican volcanic belt experienced no net change in bulk $\text{Fe}^{3+}/\Sigma\text{Fe}$ ratios despite significant changes in volatile content and extent of crystal fractionation (Crabtree & Lange, 2011). These observations suggest that low-pressure crystallization and degassing do not significantly oxidize arc magmas and instead indicate that high $\text{Fe}^{3+}/\Sigma\text{Fe}$ ratios recorded by arc magmas reflect a mantle source that has higher $f\text{O}_2$ than MORB source mantle.

Outside of mid-ocean ridge settings, Fe redox studies that specifically address the effects of differentiation on Fe speciation have thus far been limited. For example, elevated magmatic water contents, derived from the subducting plate, may suppress plagioclase saturation and decrease the temperature difference between the appearance of silicates and magnetite on the liquidus (Sisson & Grove, 1993), potentially influencing whether a basaltic magma follows a calc-alkaline (Fe-depleted) or tholeiitic (Fe-enriched) differentiation path (e.g., Zimmer *et al.*, 2010). Yet, magmatic H_2O and $\text{Fe}^{3+}/\Sigma\text{Fe}$ ratios are strongly correlated (Kelley & Cottrell, 2009), and high magmatic $f\text{O}_2$ also enhances the appearance of oxides relative to silicates on the basalt liquidus (Botcharnikov *et al.*, 2008, Osborn, 1959). The effects of $f\text{O}_2$ and H_2O on magmatic differentiation may thus be difficult to segregate. Magnetite fractionation in a system closed to oxygen is also expected to reduce magmatic $\text{Fe}^{3+}/\Sigma\text{Fe}$ ratios, but this phenomenon has not been observed directly in the natural rock record. If source mantle $f\text{O}_2$ at convergent margins is elevated over MORB, the cause of this oxidation and the extent to which it varies are central to developing models for the structure and growth of arc crust, and of the oxygen evolution of Earth

through time. Does primary fO_2 change as subduction influence varies or diminishes? What effect do variable extents of fluid or sediment melt infiltration have on primary fO_2 ?

To answer these questions, we examine the relationships between crystal fractionation, degassing, mantle source composition, subduction influence, and magmatic or mantle fO_2 along the entire Mariana subduction zone. With this work, we investigate a variety of crystal fractionation and degassing processes recorded by arc and back-arc basaltic glasses and examine the relationships between these processes and magmatic Fe redox. We present new major, trace, and volatile element concentrations as well as $Fe^{3+}/\Sigma Fe$ ratios in olivine-hosted melt inclusions from single eruptive events at five sub-aerial volcanic centers along the Mariana arc (Sarigan, Guguan, Alamagan, Pagan, and Agrigan), in addition to submarine glasses from NW Rota-1 and Pagan volcanoes (Tamura *et al.*, 2013, Tamura *et al.*, 2011) and the Mariana trough back arc spreading center (Fig. 1). After assessing the effects of differentiation on magmatic redox, we use major element trends defined by the data to reconstruct primary melt compositions and mantle source fO_2 conditions. We then pair these with key trace element ratios (Ba/La, Th/La, and Zr/Y) to assess the extent to which different slab derived materials may influence the fO_2 of the mantle wedge.

GEOLOGIC SETTING

The Mariana subduction system is a well-studied ocean-ocean convergent margin with an active sub-aerial and submarine arc made up of ~40 volcanic centers and the Mariana trough, an actively extending back-arc basin (Fig. 1; Bloomer *et al.*, 1989, Fryer, 1996, Hickey-Vargas & Reagan, 1987, Stern, 1979, Tollstrup & Gill, 2005, Woodhead, 1989). The arc is split into three distinct segments, the Northern Seamount Province, the Central Island Province, and the

Southern Seamount Province. The Central Island and Southern Seamount Provinces are both built on oceanic lithosphere previously rifted by the opening of the Mariana trough and the Parece-Vela basin (Fryer, 1996). The composition of erupted products along these arc volcanic centers are well studied and are primarily basaltic in composition (Bloomer *et al.*, 1989, Kelley *et al.*, 2010, Martindale *et al.*, 2013, Meijer & Reagan, 1981, Pearce *et al.*, 2005, Shaw *et al.*, 2008, Wade *et al.*, 2005). The northern to central Mariana trough, here termed collectively the northern Mariana trough, is opening asymmetrically in an east-west direction and generally mimics the arcuate shape of the volcanic front (Fryer, 1996). The volcanic arc follows the strike of the Mariana trench north of $\sim 13^{\circ}\text{N}$. South of this latitude, the trench curves sharply to an east-west orientation. In this area, both arc and back-arc volcanism approach the trench and the subducting Pacific plate is shallower beneath this magmatically active area (Ribeiro *et al.*, 2013, Syracuse & Abers, 2006). Taken together, the oceanic upper plate, mafic magmatism, and the presence of a mature back-arc spreading center make the Mariana arc an ideal setting for studying the competing effects of source $f\text{O}_2$ and shallow crustal processes on the $\text{Fe}^{3+}/\Sigma\text{Fe}$ ratios of arc and back-arc basalts.

SAMPLES AND METHODS

Mariana arc tephra samples

Olivine hosted melt inclusions were targeted for this study for several reasons. First, suites of melt inclusions from a single eruptive event at a volcano potentially display a range of variable, pre-eruptive magmatic compositions that correspond to the changing compositions of a differentiating magma. Olivine is an early fractionating phase in the evolution of basaltic magma, such that melt inclusions hosted in olivine often record early stages of differentiation

compared to plagioclase- or clinopyroxene-hosted inclusions, and so their compositions may be closer to the composition of parental magmas than the final erupted lavas. Finally, melt inclusions have also been shown to preserve less degassed volatile concentrations than erupted lavas, allowing the study of the effects of volcanic degassing along with crystal fractionation on Fe redox in subduction zone magmas.

The glass inclusions analyzed in this study were picked from nine Mariana arc tephra samples originating from five volcanoes from the Central Island province of the Mariana arc (numbers indicate disparate eruptions): Sarigan (Sari15-04), Guguan (Gug11 and Gug23-02), Alamagan (Ala02 and Ala03; Shaw *et al.*, 2008), Pagan (Paga8), and Agrigan (Agri07, Agri05 and Agri04, Fig. 1). These samples were collected by a MARGINS-NSF field expedition to the Mariana arc in 2004 and donated to this study by T. Plank (<http://sio.ucsd.edu/marianas>; Figure 1). Each tephra sample was washed in de-ionized water and sieved, taking care to avoid any samples with clasts larger than two centimeters to ensure that all material had a short cooling history upon eruption (e.g., Lloyd *et al.*, 2012). Olivine crystals were either hand-picked from sieved size fractions or separated using lithium poly-tungstate heavy liquid separation, using modified techniques from Luhr (2001). Large (0.5 -1 mm), euhedral olivines or olivine fragments were immersed in mineral oil to identify glass inclusions, which were selected for analysis if they were >50 μm in diameter, completely glassy, without daughter or co-entrapped minerals, fully contained by the host olivine, and contained no more than one vapor bubble. Representative photomicrographs are shown in Figure 2. Photomicrographs of every inclusion are shown in electronic appendix K.

Submarine glass samples

Glassy pillow lavas from the southernmost Mariana trough (Malaguana-Gadao ridge) were dredged from the seafloor between 12.5° - 13.2°N, during expedition TN273 of the R.V *Thomas G. Thompson* in 2011-2012 (Southern Mariana trough, Fig. 1). Glassy pillow lavas from submarine volcanic exposures at Pagan and NW Rota-1 volcanoes were provided by Yoshi Tamura (Tamura *et al.*, 2013, Tamura *et al.*, 2011). Glass chips were chiseled and hand picked from the freshest pillow lavas in each dredge and washed in de-ionized water prior to preparation for analysis. We also incorporate previously published data for submarine glass samples from the northern Mariana trough (18.1° - 20.9°N; Kelley & Cottrell, 2009, Newman *et al.*, 2000, Pearce *et al.*, 2005, Stolper & Newman, 1994; Fig. 1)

Analytical methods

Electron Microprobe Analysis

Submarine glass chips and glass inclusions were exposed on a single side and polished for electron microprobe analyzer (EMPA) analysis on a JEOL-8900 5 spectrometer microprobe at the Smithsonian Institution. During major element analysis, the beam was operated at 10nA, an accelerating voltage of 15 kV and 10 µm beam diameter. Sodium and potassium were measured first with 20 second peak count times to minimize alkali loss. Subsequently, Si, Ti, Al, Fe*, Mn, Ca and P were measured with 30-40 second peak count times. All data were subject to ZAF correction procedures. Primary calibration standards include VG-2 glass, Kakanui hornblende, anorthite, microcline, ilmenite, and apatite (Jarosewich *et al.*, 1980). The VG-2 and VG-A99 glasses were monitored as secondary standards during each run (Jarosewich *et al.*, 1980). Sulfur and chlorine were measured separately using a beam operated at 80 nA, an accelerating voltage of 15 kV and 10 µm beam diameter. Scapolite was used as the primary calibration standard (0.529 wt% S, 1.49 wt% Cl). The VG-2 (1320 ppm S, 300 ppm Cl) and

NIST 620 (1121 ppm S) glasses were used as secondary standards in each run (Jarosewich *et al.*, 1980, Carroll & Rutherford, 1988, Wallace & Carmichael, 1991).

The major element compositions of the olivine hosts were measured adjacent to the glass inclusions as well as at the rims of the olivines to eliminate zoned hosts that reflect potentially complex magmatic histories. A focused electron beam was operated at 10 nA and an accelerating voltage of 15 kV. San Carlos olivine and fayalite were used as primary calibration standards, San Carlos olivine and Springwater olivine were used as secondary standards during each run (Jarosewich *et al.*, 1980). Significant olivine zoning was not observed for any samples in this study and the olivine compositions reported in electronic appendix E are average values of all three to six analysis spots on each olivine.

FTIR Analysis

After EMPA analysis of melt inclusions, all sample pits were polished away, being careful to account for possible electronic damage within the activation volume of each EMPA spot. Melt inclusions were then polished from the opposite side until doubly exposed, and submarine glasses were wafered to a nominal thickness of 80 μm (though some were as thin as 20 μm) to create wafers with analyzable pools of optically clear glass. All wafered samples were washed gently with acetone to remove all epoxy residues. Dissolved H_2O and CO_2 concentrations in glasses and glass inclusions were analyzed by Fourier-transform infrared (FTIR) spectroscopy at the Smithsonian Institution. All samples were analyzed using either a Bio-Rad MA-500 microscope attached to a Bio-Rad Excalibur FTS 3000 FTIR spectrometer or a Continuum microscope coupled with a Thermo-Nicolet 6700 FTIR spectrometer. Spectra for all samples were collected between 1000-6000 cm^{-1} using a tungsten-halogen source, KBr beamsplitter and a liquid-nitrogen cooled MCT-A detector. The bench, microscope, and samples

were continuously purged by air free of water and carbon dioxide using a Whatman purge-gas generator. Aperture dimensions were selected for each sample depending on the geometry of free glass pathways, ranging in size from 12 μm x 12 μm to as large as 60 μm x 60 μm . Dissolved total H_2O concentrations were determined using the 3530 cm^{-1} band where possible, although the elevated H_2O concentrations typical of arc glass inclusions frequently result in saturation at 3530 cm^{-1} . In these cases, the OH^- absorption (4500 cm^{-1}) and molecular H_2O absorption (1630, 5200 cm^{-1}) bands were summed to calculate total H_2O concentrations. In samples where the 3530 cm^{-1} band was not saturated, total H_2O concentrations calculated from the 4500 + 1630/5200 cm^{-1} bands agree within error (<10% relative) with those calculated from the 3530 cm^{-1} band. Dissolved CO_3^{2-} concentrations were determined by using the 1515 and 1435 cm^{-1} absorption bands (Dixon *et al.*, 1995). Thicknesses of each sample were measured using a piezometric digimatic indicator ($\sigma \pm 1 \mu\text{m}$). Glass densities and absorption coefficients relevant to each absorption band were calculated using methods from Dixon *et al.* (1995) and Luhr (2001).

XANES analysis

All samples were analyzed *in situ* for $\text{Fe}^{3+}/\Sigma\text{Fe}$ ratios via micro X-ray absorption near edge structure spectroscopy (μ -XANES) following the methods and techniques of Cottrell *et al.* (2009) at beamline X26A, National Synchrotron Light Source, Brookhaven National Laboratory. Spectra were collected in fluorescence mode from 7020 eV and 7220 eV using a Si [311] monochromator and a nominal beam size of 9x5 μm . A beryllium window over the detector was used to attenuate high count rates above the main Fe $K\alpha$ fluorescence peak. Reference glass LW-0 was monitored continuously during each experimental session to correct for instrument drift. Further details related to this correction can be found in Cottrell *et al.* (2009).

Spectra were scrutinized for any influence from host olivines, phenocrysts, or micro phenocrysts in the glass chips and inclusions. If crystal interference was found, these spectra were eliminated from further study. Examples of the influence of crystal interference on Fe-XANES spectra are provided in Electronic Appendix A (Fig. A1). Determination of $\text{Fe}^{3+}/\Sigma\text{Fe}$ ratios in basaltic glasses following the methods of Cottrell *et al.* (2009) have an associated precision of ± 0.005 .

LA-ICP-MS analysis

Abundances of 33 trace elements (Sc, V, Cr, Co, Ni, Cu, Zn, Rb, Sr, Y, Zr, Nb, Cs, Ba, La, Ce, Pr, Nd, Sm, Eu, Gd, Tb, Dy, Ho, Er, Tm, Yb, Lu, Hf, Ta, Pb, Th, U) were determined in submarine glasses and glass inclusions by laser-ablation inductively-coupled plasma mass spectrometry (LA-ICP-MS) at the Graduate School of Oceanography, University of Rhode Island on a Thermo X-Series II quadrupole ICP-MS coupled with a New Wave UP 213 Nd-YAG laser ablation system following techniques outlined by Kelley *et al.* (2003) and Lytle *et al.* (2012), normalizing to ^{43}Ca as the internal standard. The laser energy was 0.20-0.30 mJ at the sample surface for a reference spot (60 μm , 10 Hz) on NIST 612 glass and the repeat rate was decreased to 5 Hz in melt inclusions and thin glass wafers, to achieve a slow drilling rate of $\sim 1 \mu\text{m/s}$ through thin samples. Spot sizes ranged from 20-80 μm . United States Geological Survey glass standards BCR-2g, BHVO-2g, BIR-1g, and Max Planck Institute glass standards GOR-132-G, StHls-G, T1-G, ML3B-G and KL2-G were used to create linear calibration curves ($R^2 > 0.990$) for each analytical session (Jochum *et al.*, 2006, Kelley *et al.*, 2003). Melt inclusions were analyzed in single spot analyses. Counting statistics were examined carefully for each element and those elements that did not return strong signals for the entire length of the laser

ablation period were discarded. Submarine glasses were analyzed in triplicate and concentrations were reproducible to within 4% rsd for all elements.

RESULTS

In total, 113 olivine-hosted glass inclusions were prepared for analysis. Thirty-four of these inclusions were lost during various stages of preparation or did not return glassy XANES spectra, suggesting that they had an unfavorable geometry for XANES analysis or were otherwise devitrified. The remaining 79 inclusions were subject to data filtering procedures outlined below.

Inclusion/olivine equilibrium and post-entrapment crystallization

Melt inclusions are trapped in olivine phenocrysts at high temperatures. As inclusion and olivine cool during magmatic ascent and eruption, olivine may precipitate along the wall of the inclusion during post-entrapment crystallization (PEC). To screen for the effects of PEC, the predicted equilibrium olivine composition was calculated for each melt inclusion using Fe^{2+}/Mg $K_D^{\text{olv/liq}} = 0.3$ (Roeder & Emslie, 1970), and compared to the measured host forsterite contents (Fo ; $\text{Mg}/[\text{Fe}^{2+} + \text{Mg}]$) of the olivine host of each inclusion. If the predicted equilibrium $\text{Fo}_{\text{inclusion}}$ matched the measured Fo_{host} , equilibrium between inclusion and host was assumed and no action was taken. If the inclusion composition has been modified by PEC, the predicted equilibrium $\text{Fo}_{\text{inclusion}}$ should be lower than the measured Fo_{host} (e.g., Anderson, 1973). In these cases, calculated equilibrium olivine was added to the inclusion in 0.1% increments until the inclusion and host reached equilibrium. If the predicted equilibrium $\text{Fo}_{\text{inclusion}}$ was higher than the Fo_{host} (indicative of Fe loss, e.g., Danyushevsky et al., 2000) no action was taken. Those inclusions that required >2% PEC correction or whose $\text{Fo}_{\text{host}} - \text{Fo}_{\text{inclusion}}$ disagreed by more than 2% were excluded from further consideration or modeling, although their compositions are reported in

electronic appendix B. Furthermore, for each melt inclusion suite, the inclusion compositions were compared to published whole-rock and melt inclusion data for each volcano, with particular attention to variation in FeO^* vs MgO (Electronic Appendix A; Danyushevsky *et al.*, 2000). Inclusion compositions that fell outside of the data field defined by the published whole-rock data were excluded. This rigorous data filtering is meant to avoid melt inclusion compositions with complicated magmatic histories that may cloud the discussion of magmatic redox variations and source $f\text{O}_2$. The remaining discussion considers only the 48 melt inclusions that satisfy the requirements outlined here.

Compositions of Mariana arc and back-arc melt inclusions and glasses

In order to constrain the effects of fractional crystallization and volcanic degassing on $\text{Fe}^{3+}/\Sigma\text{Fe}$ ratios in natural basaltic magmas, we first identify the mineral and volatile phases that have fractionated, degassed, or diffused to create the variations in major element and volatile concentrations observed in melt inclusions and submarine glasses from the Mariana arc and trough. Fractional crystallization models that aimed to match the observed major element variations were generated using Petrolog3 (Fig. 3; Danyushevsky & Plechov, 2011) for all sample suites in this study. A single crystallization model was chosen for each geographic location and is compared with published natural sample compositions and data from this study in electronic appendix A. Each model follows the general pattern of olivine \pm clinopyroxene \pm plagioclase \pm magnetite fractionation. Individual model parameters, including mineral-melt models and pressure conditions that were chosen to generate each liquid line of descent (LLD) can be found in electronic appendix A. Volatile element behavior was investigated for each LLD by examining the behavior of volatile species (e.g., H_2O , CO_2 , S) relative to other volatiles (e.g., CO_2 vs H_2O). For all samples, we also compare major and volatile element variations to

previously published melt inclusion data from the same island (electronic appendix A, Fig. 4).

Here, we outline the magmatic processes that are captured by these samples and the magnitude and variations of their $\text{Fe}^{3+}/\Sigma\text{Fe}$ ratios.

Mariana volcanic arc

Agrigan volcano; We include melt inclusions from three eruptive events at Agrigan volcano (tephra layers Agri04, Agri 05, and Agri07). These melt inclusions are basaltic in composition and range in MgO concentration from 3.12 to 5.81 wt% (Fig. 3a-d, A2). The two inclusions with the highest H_2O concentrations in this study are from samples Agri07 and Agri04. The inclusion from Agri07 has a low CO_2 concentration that is inconsistent with closed system degassing behavior, where high pressure CO_2 volatilization and lower pressure H_2O volatilization should produce a near vertical relationship between CO_2 and H_2O on Figure 4a for an ascending, degassing magma (Dixon *et al.*, 1995). There is also no correlation between S and H_2O (Figure 4b). Taken together, neither H_2O - CO_2 nor H_2O -S variations are consistent with simple degassing processes, suggesting that the volatile contents of these inclusions represent complex degassing behaviors.

Agrigan melt inclusions have $\text{Fe}^{3+}/\Sigma\text{Fe}$ ratios that range from 0.217 to 0.344. The highest MgO sample in this suite (MgO = 5.82 wt%) has $\text{Fe}^{3+}/\Sigma\text{Fe} = 0.242$, which is more oxidized than the most oxidized MORB glass at a comparable MgO content ($\text{Fe}^{3+}/\Sigma\text{Fe} = 0.178$ at 6.18 wt% MgO) from Cottrell and Kelley (2011; Fig. 5). There is no correlation between H_2O concentrations and $\text{Fe}^{3+}/\Sigma\text{Fe}$ ratios among these inclusions, despite >4 wt% difference in the highest and lowest H_2O concentrations (Fig. 4c). Specifically, the two inclusions with the highest water contents of all samples in this study are not oxidized or reduced relative to the others in the same suite.

Pagan volcano; One glass inclusion and five submarine glasses from Pagan are basaltic in composition and have MgO concentrations ranging from 5.44 – 7.17 wt% (Fig. 3a-d). The single glass inclusion produced interference fringes in the FTIR spectra such that dissolved CO₂ was not detectable. Water and S concentrations in the inclusion are among the lowest concentrations observed in all glass inclusions from this study.

The melt inclusion Paga8-2 has an Fe³⁺/ΣFe ratio of 0.222 at MgO = 5.44 wt%. Submarine Pagan glasses have Fe³⁺/ΣFe ratios that range from 0.219 to 0.252 and MgO concentrations similar to those found in MORB glass (~7 wt% MgO). Like Agrigan melt inclusions, these samples are more oxidized than the most oxidized MORB glasses at a comparable MgO content, but their Fe³⁺/ΣFe ratios do not vary systematically with MgO concentrations. It is important to note that the composition and Fe³⁺/ΣFe ratio of the sole melt inclusion from Pagan volcano are consistent with values reported for melt inclusions from other volcanoes studied in this work. Furthermore, it is similar in MgO concentration and Fe³⁺/ΣFe ratio to submarine glasses from Pagan, demonstrating that melt inclusions have the potential to record similar compositional and redox information as submarine glasses (Fig. 5).

Alamagan volcano; Alamagan inclusions come from two separate eruptive events (tephra samples Ala02 and Ala03) that are basaltic in composition and have the widest range in MgO concentrations of any suite in this study (3.87 – 7.40 wt%). Alamagan inclusions have a range in CO₂ and H₂O concentrations that are consistent with CO₂ degassing (Fig. 4a, Dixon *et al.*, 1995). They exhibit a range of sulfur concentrations from 664 - 1544 ppm, which vary with H₂O and are broadly consistent with sulfur degassing (Fig. 4b; e.g., Sisson & Layne, 1993, Wade *et al.*, 2006). Melt inclusions from tephra layer Ala02 from this study overlap with the major element

and volatile compositions of melt inclusions from the same tephra layer from Shaw *et al.* (2008) (Fig. 4a, b, A4).

Alamagan inclusions have $\text{Fe}^{3+}/\Sigma\text{Fe}$ ratios that range from 0.207 – 0.267, with $\text{Fe}^{3+}/\Sigma\text{Fe} = 0.244$ in the inclusion with the highest MgO concentration (Ala02-15, 7.40 wt% MgO; Fig. 5), significantly more oxidized than MORB glasses with the same MgO concentration ($\text{Fe}^{3+}/\Sigma\text{Fe} = 0.16$; Cottrell & Kelley, 2011). The $\text{Fe}^{3+}/\Sigma\text{Fe}$ ratios of these inclusions generally decrease with MgO (Fig. 5). There is no systematic variation in $\text{Fe}^{3+}/\Sigma\text{Fe}$ ratios with variable H_2O concentrations (Fig. 4c).

Guguan volcano; Two Guguan glass inclusions are basaltic in composition and have MgO concentrations of 3.96 and 5.70 wt%. It is difficult to assess any compositional trends with only two samples, although both of these samples are consistent with published whole rock and melt inclusion data from Guguan volcano (Electronic Appendix A, Fig. A5). We thus consider their compositional differences within the context of the literature data. One inclusion yielded a resolvable CO_2 concentration, recording a $\text{H}_2\text{O}+\text{CO}_2$ pressure of entrapment of 4.3 kbar (Fig. 4a; Newman & Lowenstern, 2002). Sulfur and H_2O concentrations in these inclusions are consistent with sulfur degassing (Fig. 4b). These inclusions have $\text{Fe}^{3+}/\Sigma\text{Fe} = 0.257$ and 0.263, both more oxidized than the most oxidized MORB glasses, (Fig. 5; Cottrell & Kelley, 2011). Although these melt inclusions are sourced from a different tephra layer, their compositions and oxidation states are consistent with Guguan melt inclusions from Kelley and Cottrell (2009).

Sarigan volcano; Sarigan melt inclusions are basaltic and have a narrow range of MgO, from 5.20 - 6.96 wt%. They record pressures of entrapment between 0.87 – 3.4 kbar and demonstrate closed system $\text{H}_2\text{O}-\text{CO}_2$ degassing behavior (Fig. 4a; Newman & Lowenstern,

2002). They exhibit a range of sulfur concentrations from 1188 to 1614 ppm that suggest minimal sulfur degassing (Fig. 4b).

Sarigan inclusions capture a very narrow range of melt inclusion compositions, but exhibit a large range in $\text{Fe}^{3+}/\Sigma\text{Fe}$ ratios from 0.195 – 0.280, all of which are more oxidized than average MORB glasses with same MgO concentrations (Cottrell & Kelley, 2011). There are no systematic variations in $\text{Fe}^{3+}/\Sigma\text{Fe}$ ratios with indices of crystal fractionation, sulfur or H_2O concentrations (Fig. 5, Fig. 6, Fig. 4c, respectively).

NW Rota-1 volcano; Submarine glasses from NW Rota-1 submarine volcano are basaltic and have $\text{MgO} = 5.15\text{--}6.29$ wt%. These glasses have $\text{Fe}^{3+}/\Sigma\text{Fe}$ ratios between 0.190 – 0.237, all more oxidized than MORB glasses with the same MgO concentrations (Cottrell & Kelley, 2011). Like the submarine Pagan glasses, $\text{Fe}^{3+}/\Sigma\text{Fe}$ ratios do not vary systematically with MgO concentration.

Mariana trough

Northern Mariana trough; Submarine Mariana trough glasses are split into two geographical groups, the northern Mariana trough samples and the southern Mariana trough samples. Northern Mariana trough major element and volatile concentrations are taken from Pearce *et al.* (2005), Stolper and Newman (1994), and Newman *et al.* (2000). They are basaltic in composition and range in MgO from 3.87 – 7.72 wt%. Dissolved H_2O and CO_2 concentrations are consistent with the pressure of the water column at an eruption depth of approximately 4 km. Stolper and Newman (1994) and Newman *et al.* (2000) have shown that these glasses are the result of magmas that were variably saturated with a $\text{H}_2\text{O}\text{--}\text{CO}_2$ rich fluid upon eruption. The range in H_2O contents of these samples results from the variable influence of the subducting slab in the genesis of northern Mariana trough magmas (Stolper & Newman, 1994).

$\text{Fe}^{3+}/\Sigma\text{Fe}$ ratios for these glasses are reported by Kelley and Cottrell (2009) and examined here in the context of the Mariana subduction system. $\text{Fe}^{3+}/\Sigma\text{Fe}$ ratios range from 0.150 – 0.182, overlapping the MORB array in samples with <1.0 wt% H_2O , but vertically offset to ~1% higher $\text{Fe}^{3+}/\Sigma\text{Fe}$ ratios for samples with >1.0 wt% H_2O . There is a strong positive correlation between $\text{Fe}^{3+}/\Sigma\text{Fe}$ ratios and H_2O in the northern Mariana trough sample suite (Fig. 4c).

Southern Mariana trough; Southern Mariana trough glasses are more evolved than the northern submarine glasses, with SiO_2 ranging from 51.90 to 59.83 wt%, and MgO ranging from 2.15 – 5.87 wt%. Although separated geographically from Northern Mariana trough samples by greater than 700 km, major element variations for southern Mariana trough glasses are similar to those of the northern trough, but extend to more evolved compositions. Importantly, samples below 4 wt% MgO show evidence for magnetite saturation in both major element variations (Fig. 3e-h) and in select trace element contents (V, Cr; Fig. A9). This is also supported by the modeled LLD (black line, Fig. 3e-h).

Only two of these samples have resolvable CO_2 concentrations, but these yield saturation pressures that are consistent with their depths of collection (Fig. 4a; Newman & Lowenstern, 2002). Sulfur concentrations vary from 157 – 583 ppm, increasing with decreasing H_2O concentrations until $\text{H}_2\text{O} \sim 2$ wt%, at which point sulfur concentrations begin to decrease with decreasing H_2O concentrations. Samples from the southern portion of the Mariana trough display a range in $\text{Fe}^{3+}/\Sigma\text{Fe}$ ratios from 0.171 – 0.207, although in contrast to the northern Mariana trough glasses, these ratios do not correlate strongly with MgO, H_2O or S concentrations (Fig. 5a, 4c, 6, respectively).

DISCUSSION

Relationships of $\text{Fe}^{3+}/\Sigma\text{Fe}$ to magmatic differentiation processes

Fractional crystallization

If Fe^{3+} behaves simply as an incompatible element and magmatic $f\text{O}_2$ is not buffered, low pressure fractionation of olivine, clinopyroxene, and plagioclase from basaltic magmas should lead to an increase in the $\text{Fe}^{3+}/\Sigma\text{Fe}$ ratio of the magma. Data for MORBs are consistent with this behavior, showing slight oxidation during fractional crystallization (Cottrell & Kelley, 2011). In such a system that is closed to oxygen exchange with its surroundings, Fe^{2+} partitions into olivine and clinopyroxene, while Fe^{3+} remains in the melt. As fractionation proceeds, the total volume of liquid decreases, the Fe^{2+} content of the melt decreases, and the Fe^{3+} content of the melt increases, resulting in an increase in magmatic $\text{Fe}^{3+}/\Sigma\text{Fe}$ ratio. Each modeled LLD for the Mariana arc demonstrates these principles of crystal fractionation-induced oxidation (Fig. 5, electronic appendix A).

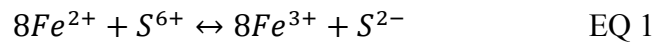
Major element variations of melt inclusion and submarine glass suites from the Mariana arc are consistent with the general pattern of olivine \pm clinopyroxene \pm plagioclase fractionation. In all cases, the $\text{Fe}^{3+}/\Sigma\text{Fe}$ ratios in both arc melt inclusions and submarine glasses are more oxidized than the most oxidized MORB glasses from Cottrell and Kelley (2011). Importantly, melt inclusions from Sarigan and Alamagan volcanoes and submarine glasses from Pagan and NW Rota-1 volcanoes are more oxidized than MORB glasses with similar MgO concentrations. This indicates that the composition and $\text{Fe}^{3+}/\Sigma\text{Fe}$ ratios of any arc melt inclusion or submarine glass in this study cannot be recreated simply by extensively fractionating a MOR-type primary melt (Fig. 5). In fact, low-pressure fractionation of olivine, clinopyroxene, and plagioclase in any combination cannot generate the observed variations in $\text{Fe}^{3+}/\Sigma\text{Fe}$ ratios in most of the Mariana arc samples. The exceptions to this are in two inclusions from Agrigan volcano, where an increase in $\text{Fe}^{3+}/\Sigma\text{Fe}$ ratios from 0.225 to 0.283 and 0.343 occurs approximately coincident with

the onset of abundant plagioclase fractionation. In our modeling, plagioclase represents ~2% of the total proportion of fractionating phases (olv~64%, cpx~34%) before this increase in magmatic $\text{Fe}^{3+}/\Sigma\text{Fe}$ ratios. At melt $\text{MgO} = 4.1$ wt%, the modal proportion of plagioclase increases to ~10% (olv~55%, cpx~35%), and continues to rise as fractionation continues. At the same time, the modal proportion of olivine decreases. The associated increase in $\text{Fe}^{3+}/\Sigma\text{Fe}$ ratios is predicted by the fractionation model (Fig. 5a) and arises as a result of the incompatibility of Fe^{3+} during crystallization, as described above. It is important to note that although plagioclase contains no Fe^{2+} or Fe^{3+} in our modeling, the decrease in total liquid volume associated with abundant plagioclase fractionation, combined with a slight decrease in Fe^{2+} in the liquid by continued olivine fractionation can result in a significant increase in magmatic $\text{Fe}^{3+}/\Sigma\text{Fe}$ ratios. Our data are consistent with this model prediction (Fig. 5a) and these two samples suggest that this increase in $\text{Fe}^{3+}/\Sigma\text{Fe}$ ratios may be as great as ~0.1 (absolute).

Spinel may fractionate at high-pressure in magmas. There is no evidence that these magmas were ever in equilibrium with a spinel phase, but if they were and $D_{\text{Fe}^{3+}}^{\text{spl/liq}} > 1$, in a system closed to oxygen the impact of spinel fractionation from the magma will reduce $\text{Fe}^{3+}/\Sigma\text{Fe}$ ratios in the magma. In this case, the $\text{Fe}^{3+}/\Sigma\text{Fe}$ ratios of the highest MgO melt inclusions in this study are minima. Magnetite ($\text{Fe}^{3+}_2\text{Fe}^{2+}\text{O}_4$) is the next solid phase with $D^{\text{Fe}^{3+}} > 1$ to fractionate from basaltic magmas. In a system closed to oxygen exchange with its surroundings, magnetite fractionation is expected to drive magmatic reduction through the preferential removal of Fe^{3+} from the liquid. In the modeled LLD for the Mariana back-arc samples, however, significant magmatic reduction does not occur at the point of magnetite-in (4 wt% MgO; Fig. 5a). Rather, magnetite fractionation in the model appears to combat the oxidizing effects of olivine \pm clinopyroxene \pm plagioclase such that the net effect is to maintain roughly constant magmatic

$\text{Fe}^{3+}/\Sigma\text{Fe}$ ratios after magnetite-in (Fig. 5; electronic appendix A). The $\text{Fe}^{3+}/\Sigma\text{Fe}$ ratios of Mariana back-arc samples are consistent with the predicted magmatic oxidation from the modeled LLD until ~ 5.5 wt% MgO (Fig. 5a), although at lower MgO concentrations, the $\text{Fe}^{3+}/\Sigma\text{Fe}$ ratios of Mariana trough samples are remarkably constant. It is possible that this reflects the combined effects of olivine + clinopyroxene + plagioclase + magnetite fractionation, as demonstrated by the modeled LLD (Fig. 5a), but geochemical evidence for magnetite saturation does not appear until ~ 4 wt% MgO, much lower MgO than the point where the natural data fall away from the modeled LLD (Fig. 3e-h, A9). Other processes, such as sulfide fractionation or sulfur degassing, may influence magmatic redox conditions for these samples.

Sulfide fractionation may impact magmatic $\text{Fe}^{3+}/\Sigma\text{Fe}$ ratios via the Fe-S redox couple:



For example, EQ 1 has been invoked to explain the stabilization of solid sulfide phases in oxidized, magnetite saturated magmas with relatively low S contents from the Pual Ridge in the Manus Basin (Jenner *et al.*, 2010). The saturation of magnetite from a basaltic melt will remove a greater proportion of Fe^{3+} than Fe^{2+} from a melt, provided the magnetite has a higher $\text{Fe}^{3+}/\Sigma\text{Fe}$ ratio than the melt. If the concentrations of both Fe^{2+} and Fe^{3+} are controlled only by crystal fractionation, when magnetite begins fractionating, EQ 1 will shift to the right to maintain the equilibrium constant, K_{eq} . This will reduce S^{6+} , producing S^{2-} and potentially promoting the saturation of a solid sulfide phase at relatively low dissolved sulfur concentrations. Importantly, this shift in equilibrium to the right of EQ 1 will also produce a new equilibrium proportion of Fe^{3+} . If EQ 1 is important in Fe and S bearing basaltic magmas, then S and Fe species cannot be treated as conservative during any volcanic process that may disturb the equilibrium.

Sulfur concentrations in Mariana trough glasses begin to decrease below 5 wt% MgO (not shown) and 2 wt% H₂O (Fig. 4b). Experimentally constrained estimates for the sulfur content at sulfide saturation (SCSS) for relevant pressures, temperatures, compositions, and fO_2 range from 950 ppm to >2000 ppm for all Mariana trough glasses (Jenner *et al.*, 2010, Jugo *et al.*, 2010, Liu *et al.*, 2007). The maximum sulfur content observed in these samples is only 553 ppm, suggesting that the Mariana trough magmas are not sulfide saturated. Instead, sulfur may have partitioned into a vapor phase, a process that has been shown to reduce magmas if the vapor phase is SO₂ (Fig. 4b; Kelley & Cottrell, 2012), although H₂S degassing could also oxidize magmas under the right conditions (Métrich *et al.*, 2009). It is difficult to assess the independent importance of sulfur degassing on the Fe³⁺/ΣFe ratios of these samples because of the evidence for simultaneous magnetite fractionation. The relative constancy of Fe³⁺/ΣFe ratios in Mariana trough samples with MgO < 5.5 wt% suggests that the redox equilibria illustrated by EQ 1 may have played an important role in controlling Fe³⁺/ΣFe ratios in these samples, particularly if both magnetite fractionation and S degassing reduce magmas. Further work in quantifying the relative reduction potentials of Fe and S in basaltic magmas will aid in understanding the evolution of Fe³⁺/ΣFe ratios during magmatic processes.

The effect of fO_2 on tholeiitic index

Magmatic differentiation may influence the Fe³⁺/ΣFe ratio, as discussed above, but magmatic fO_2 also plays an important role in determining the differentiation path of basaltic magmas, which may follow variably tholeiitic or calc-alkaline trends, depending on the extent of FeO* enrichment or depletion that occurs in the early stages of crystallization (Irvine & Baragar, 1971, Miyashiro, 1974, Zimmer *et al.*, 2010). Predominant models for generating these trends involve the interplay of plagioclase and magnetite fractionation and the petrological factors that

control these phases. The generation of calc-alkaline magmas (i.e., FeO* depleted) in subduction settings may be related to the high pre-eruptive water contents of arc magmas, which suppress plagioclase, but not magnetite, crystallization (Botcharnikov *et al.*, 2008, Sisson & Grove, 1993, Spulber & Rutherford, 1983). The tholeiitic index (THI) was introduced as a way to quantify the behavior of Fe during early magmatic differentiation, defined as the [FeO*] at MgO = 4.0 ± 1.0 wt% divided by the [FeO*] at MgO = 8.0 ± 1.0 wt% ($\text{FeO}^*_{4.0}/\text{FeO}^*_{8.0}$), such that a tholeiitic magma has a THI > 1.0, and a calc-alkaline magma has a THI < 1.0 (Zimmer *et al.*, 2010). Samples from both the Mariana arc and trough from this study are consistent with observations from Zimmer *et al.* (2010), where Mariana arc volcanoes display slightly calc-alkaline trends and also have higher pre-eruptive water contents (>1.5 wt%) than the Mariana trough, which falls distinctly in the tholeiitic field (THI > 1.2) and has lower pre-eruptive water contents (Fig. 7). Globally, the THI is also well correlated with magmatic $f\text{O}_2$, where arc samples are more oxidized than back-arc and MORB (Fig. 7). This suggests that the oxidized nature of arc basalts may also play an important role in the generation of calc-alkaline differentiation trends by promoting magnetite saturation over silicates (Osborn, 1959, Sisson & Grove, 1993). If magmatic $f\text{O}_2$ and H₂O contents are linked in global subduction settings, then magmas that are more calc-alkaline than Mariana arc basalts may also record higher magmatic $f\text{O}_2$ s. For example, magmas erupted from Augustine volcano have a THI of 0.65, lower than any of the predicted THI for the Mariana arc volcanoes in this study, and pre-eruptive H₂O contents above 6 wt% (Zimmer *et al.*, 2010). A single inclusion from Augustine volcano (Kelley & Cottrell, 2009) records a magmatic $f\text{O}_2$ of ~QFM+2.0 at reasonable conditions for magma storage (0.2 GPa, 1150°C), four times more oxidized than the most oxidized inclusion in this study (Fig. 7). These results are consistent with the hypothesis that, in addition to water, $f\text{O}_2$ may play a role in

generating calc-alkaline differentiation trends in arc magmas. Additionally, it may be difficult to isolate the specific roles of H₂O and fO_2 on the differentiation style of natural arc basalts because they are closely correlated in subduction zones.

The role of volatiles

Melt inclusions from Sarigan and Alamagan volcanoes each show evidence for ~2 wt% H₂O degassing, but show no corresponding variations in $Fe^{3+}/\Sigma Fe$ ratios (Fig 4). This demonstrates that H₂O degassing is not an oxidizing process in basaltic magmas, rather it is redox neutral (Carmichael, 1991, Cottrell & Kelley, 2011, Crabtree & Lange, 2011, Frost & Ballhaus, 1998). Water concentrations correlate strongly with $Fe^{3+}/\Sigma Fe$ ratios in northern Mariana trough samples, where they range from MORB-like (e.g., dry, reduced) to more oxidized as H₂O contents increase. Modeled mantle source H₂O contents for the northern Mariana trough lavas increase as fluid addition from the subducting slab increases (Newman *et al.*, 2000, Stolper & Newman, 1994). Using H₂O as a proxy for slab-derived influence on the arc and back-arc mantle sources, subduction influence has also been linked to magmatic and mantle source oxidation (e.g., Fig 4d; Kelley & Cottrell, 2009). It is important to note that H₂O itself does not drive oxidation of the mantle (Frost & Ballhaus, 1998), rather our observations in the Marianas indicate that slab fluids may be oxidized relative to ambient upper mantle and impart both elevated H₂O concentrations as well as their oxidized condition on the mantle source beneath the Mariana arc and trough (see below).

Kelley and Cottrell (2012) suggested that sulfur degassing played a dominant role in controlling $Fe^{3+}/\Sigma Fe$ ratios during the eruption recorded by Agrigan tephra 19-02. They outlined a simple model for electronic exchange between Fe and S during S degassing, where six moles of electrons are transferred to $Fe^{*}_{(melt)}$ for every one mole of $S^{2-}_{(melt)}$ that is degassed as $S^{4+}_{(vapor)}$

(black line, Fig. 6) as a possible explanation for magmatic reduction and associated S loss.

Figure 6 shows the relationship between sulfur concentrations and $\text{Fe}^{3+}/\Sigma\text{Fe}$ ratios, as observed in melt inclusion suites from Sarigan, Alamagan, Agrigan, and Guguan volcanoes. Sulfur degassing is likely recorded by Alamagan, Agrigan, and Guguan melt inclusions. Agrigan inclusions show a slight reduction in $\text{Fe}^{3+}/\Sigma\text{Fe}$ ratios with decreasing sulfur concentration that is consistent with the melt inclusion suite studied by Kelley and Cottrell (2012). In contrast, the two Guguan inclusions are different in their sulfur concentrations by >1000 ppm but do not vary significantly in their $\text{Fe}^{3+}/\Sigma\text{Fe}$ ratios, and there is no correlation between the sulfur concentrations and $\text{Fe}^{3+}/\Sigma\text{Fe}$ ratios of Alamagan inclusions, suggesting that reduction of Fe during S degassing is not a universal process for all arc volcanoes.

The effect of post entrapment processes

The large range in $\text{Fe}^{3+}/\Sigma\text{Fe}$ ratios (0.195-0.281, $\bar{x} = 0.243$) captured by melt inclusions from Sarigan volcano does not appear to be controlled by crystal fractionation or volcanic degassing. Here, we consider processes specific to melt inclusions that may impact the $\text{Fe}^{3+}/\Sigma\text{Fe}$ ratios of melt inclusions in this study. The $\text{Fe}^{3+}/\Sigma\text{Fe}$ ratios of hydrous melt inclusions have been postulated to be affected by hydrogen diffusion in to or out of an inclusion after entrapment as the host magma cools and/or degasses (e.g., Danyushevsky *et al.*, 2002). In the case of cooling, the pressure of the inclusion decreases and hydrogen fugacity in the inclusion may be lower than in the surrounding melt. This would result in hydrogen diffusion into the inclusion and potentially, the reduction of iron. Alternatively, in the case of degassing a host magma, hydrogen fugacity in the inclusion may be higher than in the surrounding melt, causing hydrogen to diffuse out of the melt inclusion and potentially oxidizing iron contained in the inclusion (Danyushevsky *et al.*, 2002). Experimental observations by Gaetani *et al.* (2012), however, have shown that

$\text{Fe}^{3+}/\Sigma\text{Fe}$ ratios in melt inclusions that have been dehydrated or hydrated are rapidly re-equilibrated with the $\text{Fe}^{3+}/\Sigma\text{Fe}$ ratios of the external melt. They hypothesize that point defects in host olivines on the metal sites (i.e., Fe^{2+} or Mg^{2+} deficiencies or similarly, O^{2-} excesses) diffuse on the same time scale as hydrogen in olivine and move in the opposite sense as hydrogen. For example, if hydrogen diffuses out of a melt inclusion, point defects in the host olivine diffuse towards the melt inclusion, effectively communicating the $f\text{O}_2$ of the external melt to the melt inclusion. Several lines of evidence suggest that H^+ diffusion does not explain the diversity of $\text{Fe}^{3+}/\Sigma\text{Fe}$ ratios in melt inclusions from this study. First, figure 4 demonstrates coherent trends with respect to H_2O degassing for Sarigan melt inclusions, diminishing the likelihood that this particular melt inclusion suite records massive diffusion. Second, the H_2O contents of inclusions from Pagan, Alamagan, Guguan, and Sarigan in this study are consistent with those of Shaw *et al.* (2008), who used hydrogen isotopes to conclude that post-entrapment hydrogen loss was not significant for carefully chosen melt inclusions. In the case of Alamagan inclusions, we studied inclusions from the same tephra sample as the inclusions from Shaw *et al.* (2008), enabling a direct comparison between studies. Additionally, similar heterogeneity in $\text{Fe}^{3+}/\Sigma\text{Fe}$ ratios that is uncorrelated with MgO is observed for submarine glasses from Pagan and NW Rota-1 volcanoes, suggesting that this heterogeneity is not simply a melt inclusion-related phenomenon (Fig. 5). There is also no relationship between the size of inclusion and major element compositions, measured $\text{Fe}^{3+}/\Sigma\text{Fe}$ ratios, or apparent disequilibrium between melt inclusion-olivine pairs, which suggests that the large melt inclusions in this study have not diffusively re-equilibrated (see electronic appendix A, Fig. A11). Finally, the trace element heterogeneity recorded in melt inclusion populations from Sarigan and Alamagan volcanoes show strong evidence of retaining magmatic trace element variability (see electronic appendix A, Fig. A10),

supporting the notion that the heterogeneity recorded in melt inclusion suites in this study reflect true magmatic heterogeneity rather than post-entrapment melt inclusion processes (Cottrell et al., 2002).

Why are arc basalts more oxidized than MORB?

Primary melt compositions and fO_2

Arc basalts are shown here to be more oxidized than MORB, even at comparable MgO concentrations. Additionally, we show that fractional crystallization and degassing processes are capable of both oxidizing and reducing $Fe^{3+}/\Sigma Fe$ ratios in arc basalts, although these effects are minor, and neither can explain the oxidation of Fe in arc basalts over MORB. This suggests a fundamental difference between the $Fe^{3+}/\Sigma Fe$ ratios of mantle-derived primary arc magmas and primary MORB magmas. To test this, primary melt compositions (i.e., in equilibrium with mantle olivine at Fo_{90}) were reconstructed using methods modified after Klein and Langmuir (1987), where modeled or data-defined LLDs provide constraints to account for the effects of fractional crystallization on magmatic composition. The fractionation models generated for each geographic location were used to calculate the primary magma composition for each sample with $MgO > 5$ wt%. Each composition was projected back to $MgO = 7.0$ wt% using the slope of the fractionation model between 5 and 7 wt% MgO for all major elements (excluding Fe). In some cases, the fractionation model was poorly fit to the most incompatible major elements (e.g., P_2O_5) and the slope of a line defined by the natural data was used for the calculation instead (Electronic Appendix E). For Fe, $FeO_{(actual)}$ and $Fe_2O_{3(actual)}$ concentrations were plotted versus MgO concentration and projected back along the slopes of lines defined by the natural data for each sample suite. The point of $MgO = 7.0$ wt% was chosen because data for the arc basaltic glasses above 7 wt% MgO are sparse, and selecting a higher MgO limit would be arbitrary. At or

above 7 wt% MgO, both the data-defined and modeled LLDs suggest that olivine or olivine + clinopyroxene are the only phases on the liquidus, due mostly to the suppression of plagioclase saturation in water rich magmas (Gaetani *et al.*, 1993, Kelley *et al.*, 2010, Parman *et al.*, 2010). Once at MgO = 7 wt%, each composition was subject to addition of equilibrium composition olivine in 0.1% increments until in equilibrium with Fo₉₀ olivine (Electronic Appendices A, E-G). Alternatively, clinopyroxene could be included along with olivine as a liquidus phase to higher MgO concentrations, although it is difficult to know when olivine becomes the only liquidus phase. Because of this uncertainty, we also used PetroLog to add clinopyroxene and olivine simultaneously back until achieving equilibrium with Fo₉₀ olivine. When applied to a suite of 20 melt inclusions from Sarigan volcano, this method returned nearly identical average primary melt $\text{Fe}^{3+}/\Sigma\text{Fe}$ ratios as the olivine only method (0.217 using PetroLog, 0.220 using the olivine only method) and because of differences in major element composition, a primary melt $f\text{O}_2 \sim 0.28$ log units below that of the method described above. This is within the ± 0.5 log unit uncertainty of the $\text{Fe}^{3+}/\text{Fe}^{2+}$ proxy for $f\text{O}_2$ (Kress & Carmichael, 1991), so we chose to use the olivine-only addition method described above because it can be applied consistently to all samples discussed below (MORB, BABB, and arc samples). An important conclusion drawn from this test is that the choice of correction method does not significantly impact the reconstructed primary oxygen fugacity. Temperatures and pressures of last equilibration with peridotite for each calculated primary melt composition were determined using the melt thermobarometer of Lee *et al.* (2009; Tables 1, 2). Primary $f\text{O}_2$ was calculated using the algorithm of Kress and Carmichael (1991; Tables 1, 2) relative to the QFM buffer calculated at pressure and temperature according to Frost (1991).

Mid-ocean ridge primary magmas have fO_2 similar to that of the QFM buffer (Fig. 8; Cottrell & Kelley, 2011). Northern Mariana trough primary melts overlap with the most oxidized MORB primary melts (\sim QFM+0.1 to QFM+0.3), but extend to QFM+0.8. Southern Mariana trough primary melts extend to QFM+0.5. Primary melts from the Mariana arc range between QFM+0.2 to QFM+1.8, which is 0.4 to 1.5 orders of magnitude more oxidized than the most oxidized MOR primary melts. After considering the effects of crystallization and degassing on magma composition and redox, it is evident that both Mariana arc and back-arc basalts are more oxidized than MORB due to a fundamental difference in fO_2 of the mantle source for these magmas.

The mantle wedge beneath Mariana arc volcanoes generates melts with fO_2 of \sim QFM+1., the average primary melt fO_2 calculated for melt inclusions and submarine glasses from arc volcanoes (including NW Rota-1) in this study. These oxidized magmas migrate into the arc crust and differentiate, possibly experiencing minor modifications to $Fe^{3+}/\Sigma Fe$ ratios due to the effects of crystallization or degassing (<0.05 , absolute). Similarly, the mantle wedge under the Mariana trough generates melts with fO_2 s that range from QFM+0.1 to QFM+0.8 in the north and from QFM+0.3 to QFM+0.5 in the south. These melts move into the crust and experience minor fractional crystallization-related Fe oxidation, or in the case of samples from the southern Mariana trough, maintain constant $Fe^{3+}/\Sigma Fe$ ratios despite evidence for sulfur degassing and magnetite fractionation. Mariana trough basalts erupt with $Fe^{3+}/\Sigma Fe$ ratios that range from MORB-like to significantly more oxidized than MORB.

There are several trace element proxies (e.g., V-based, Cu and Zn/Fe* ratios) for modeling mantle source fO_2 from the compositions of erupted basalts that can provide important additional constraints on the fO_2 of the mantle wedge in the Marianas. The application of these

models requires knowledge of the composition and mineral mode of the mantle source, the mechanisms for melt generation, and constraints on LLDs on a volcano-to-volcano basis (Lee et al., 2005, Lee et al., 2012, Lee et al., 2010). These parameters are not likely to be uniform from mid-ocean ridge settings to subduction zones, and all are challenging to constrain. A comparison between Fe redox and trace element proxies for mantle source fO_2 from this dataset is currently in progress.

The source of elevated fO_2 in the mantle wedge

Tracking sediment melt and slab fluid influences; Trace element and isotopic compositions of subduction related lavas are influenced by contributions from the downgoing slab that may include sediment melts, aqueous fluids, and slab melts. Key trace element ratios (e.g., Th/La, Ba/La) have been shown to record the contributions from these sources in lavas erupted within the arc and back-arc system of a convergent margin (e.g., Elliott *et al.*, 1997, Plank, 2005, Plank & Langmuir, 1993). Thorium is enriched in subducted terrigenous sediment and will become mobile when the sediments cross their solidi and begin to melt. Sediment melts move into the mantle wedge and contribute to the production of arc and back-arc magmas that have elevated Th/La ratios relative to MORBs. Barium, on the other hand, is mobilized preferentially over melt-mobile La via aqueous fluids that escape the subducting slab as it descends into the mantle, generating aqueous slab-derived fluids that are expected to have elevated Ba/La ratios (Johnson & Plank, 1999, Kessel *et al.*, 2005). In the Marianas in particular, the Ba/La ratio of the bulk subducting sediment package is low (Ba/La \sim 15, Plank & Langmuir, 1998), and thus sediment melts that move from the slab into the mantle wedge likely also have low Ba/La ratios. The high Ba/La ratios of Mariana arc lavas (commonly >20) require the presence of aqueous fluids to transport Ba preferentially over La into the mantle wedge. The

Marianas is a special case among global subduction settings in this respect, because trends between key trace element ratios require that separate sediment melts and aqueous fluids contribute to the composition of arc lavas (Elliott et al, 1997, Plank, 2005, Plank & Langmuir, 1998).

Arc and back-arc samples from the Marianas fall on a mixing line between mantle with $\text{Sm/La} \sim 1.35$ and $\text{Th/La} \sim 0.02$ and the bulk composition of sediments recovered from ODP Site 801, $\sim 1,100$ km east of the Mariana Islands (Fig. 9a; Plank, 2005). Some samples from Sarigan, Alamagan and Guguan volcano mix to slightly higher Th/La ratios, which may be more representative of the Th/La ratio of wind-blown sediments derived from the Asian continent that may be presently subducted beneath the Marianas, but not present at Site 801 (orange line, Fig. 9a; Plank *et al.*, 2007). Back arc samples deviate from the MORB array in Figure 9b towards a fluid with high Ba/La ratio, though lower Ba/La ratio than the fluid influencing the arc samples (Pearce *et al.*, 2005, Stolper & Newman, 1994). Mariana arc samples display a large range in Ba/La ratios that reflect significant slab fluid influence that varies in magnitude along the Mariana margin. NW Rota-1 is the least influenced by slab fluids, with Ba/La ratios similar to southern Mariana trough samples. This is an interesting observation considering its position relative to the trench, where it sits approximately 50 kilometers farther from the trench than the main subaerial arc, where the slab depth to slab is 50-100 km deeper (Syracuse & Abers, 2006). NW Rota-1 may thus receive a different style of slab fluid (or less of it) than the subaerial arc volcanic centers. Sarigan and Alamagan melt inclusions span a large portion of the entire range of Ba/La ratios observed for the arc, suggesting that there is trace element heterogeneity in parental magma compositions at Sarigan and Alamagan volcanoes.

Mantle wedge composition; In addition to containing geochemical signatures of the subducting slab, melts generated in the mantle wedge at the back-arc spreading center and under the volcanic arc may reflect variations in mantle source composition that is inherent to the mantle (Langmuir *et al.*, 2006) or generated by prior melt extraction (e.g., Kincaid, 2003, McCulloch & Gamble, 1991, Woodhead *et al.*, 1993). Here, we use the Zr/Y ratio to characterize mantle source composition. Zirconium and yttrium are not significantly fractionated during low-pressure crystal fractionation and, are expected to be relatively absent from slab-derived materials in the Marianas (Pearce & Parkinson, 1993, Pearce *et al.*, 2005). The Zr/Y ratios of arc and back-arc lavas are thus assumed to reflect the mantle source composition, independent of slab-derived additions to the mantle wedge. The Zr/Y ratio of the mantle source is, however, fractionated as the result of prior melting episodes because Zr is more incompatible than Y during mantle melting. Therefore, melts of fertile mantle will have high Zr/Y ratios, but progressive melting of the same parcel of mantle will generate subsequent melts with lower Zr/Y ratios. Mantle entering the wedge in the Marianas passes through the back-arc melting triangle and experiences melt extraction there before moving under the volcanic arc, such that the mantle under the arc is more depleted in trace elements due to melt extraction at the back-arc (Pearce *et al.*, 2005; Woodhead *et al.*, 1993). The Zr/Y ratios of Mariana trough and arc magmas reflect this contrast, with high Zr/Y ratios of Mariana trough basalts reflecting a relatively enriched MORB-type mantle (Fig. 9c; Table 1, 2; Langmuir *et al.*, 2006). The Zr/Y ratios of Mariana arc basalts are significantly lower, however, reflecting the more depleted arc mantle source, consistent with the predicted effects of back-arc spreading in mantle circulation and prior geochemical studies of the Mariana arc (Kelley *et al.*, 2010, McCulloch & Gamble, 1991, Pearce *et al.*, 2005). The Zr/Y ratios in the Marianas do not follow the mixing relationships between the estimated source

composition and the sediment materials (orange and green lines, Fig. 9c), supportive of the notion that Zr and Y do not travel with slab-derived materials into the mantle source.

Despite observed heterogeneity in trace element compositions discussed here, we emphasize that major element compositions are relatively narrow and uncorrelated with trace element ratios like La/Yb, which is greater than can be expected from simple fractionation of La from Yb during differentiation (Fig. A13). This suggests that while trace elements record the presence and mixing of several different parent magmas, mixing does not control the major element relationships in these magmas and major elements can reasonably be described by simple crystal fractionation (electronic appendix A).

Variations in fO_2 with mantle source-related variables; To assess the source of elevated fO_2 in the mantle wedge, we now examine relationships between tracers of mantle wedge composition (Zr/Y) and subduction influence (Th/La, Ba/La), and primary fO_2 . There are no systematic relationships between primary fO_2 and Zr/Y ratio within the arc or back-arc data (Fig. 10a), beyond a first-order contrast between the arc (higher fO_2 , lower Zr/Y) and the back-arc (lower fO_2 , high Zr/Y). Mariana trough Zr/Y ratios on average are higher than for mid-ocean ridge or arc samples, suggesting (a) that the Mariana trough taps an enriched mantle source (Langmuir *et al.*, 2006), and (b) that sub-arc mantle is more depleted than back-arc mantle by virtue of previous melt extraction in the back-arc melting regime. It is possible that melt extraction varies the activity of Fe^{3+} in mantle spinel phases. If melt extraction increases the activity of Fe^{3+} in spinel, then large degree melting and/or previous melt extraction could contribute to the oxidized nature of arc basalts relative to back-arc primary magmas (i.e., Parkinson & Arculus, 1999). Arc primary melts are offset towards more oxidized fO_2 s than the Mariana trough, and also record a more depleted mantle source, however there is no relationship

within either the Mariana trough or arc samples between extent of depletion and mantle source fO_2 . Moreover, MORBs encompass the full range in Zr/Y ratios observed at the Mariana arc and back-arc, with no coincident variation in fO_2 (Fig. 10a), suggesting that the observed oxidation in the Marianas is not solely a result of variable mantle source composition. We conclude that the mantle composition alone (as recorded by Zr/Y ratio) is not responsible for the elevated fO_2 of arc and back-arc basalts.

There is a weak relationship between primary fO_2 and Th/La ratio in the northern Mariana trough, but not among Mariana arc samples (Fig. 10b), and the Mariana arc and trough largely overlap in Th/La ratios. It is clear that the oxidized nature of the mantle source under the arc is unrelated to sediment melt influence, as indicated by Th/La ratio, because all of the arc samples have higher fO_2 than the northern Mariana trough samples within the same range of Th/La ratios (Fig. 10b). These observations indicate that melts of the sediments at this arc either (a) are not significantly oxidized relative to MOR source mantle, and/or (b) make up too small a proportion of total primary melt to impact mantle fO_2 . The northern Mariana trough samples range from having no detectable subduction component to moderate influence from the subducting slab. Those samples from the northern Mariana trough with higher Th/La ratios also have higher Ba/La ratios, which is in contrast to the arc, where high Th/La ratios correlate with low Ba/La ratios. The composition of the subduction component reaching the northern Mariana trough is likely to be significantly different than the compositions of the subduction components that reach the volcanic arc and may be neither a “sediment melt” or an “aqueous fluid”. This may give rise to the observed strong correlation between Th/La ratios and increasing source fO_2 for these samples, but no correlation within the arc samples, where sediment melts and slab fluids are clearly segregated by systematic co-variation of Ba/La and Th/La ratios.

There is a strong correlation between primary fO_2 and the extent of slab fluid influence, as recorded by the Ba/La ratio, within the MORB-Mariana back-arc-Mariana arc system (Fig. 10c, $R^2=0.86$, $P=0.01$). Samples within the MORB field are an exception, where lavas with elevated Ba/La ratios are relatively reduced, although the systematics within MORB are not attributed to modern subduction (Cottrell & Kelley, 2013). The northern Mariana trough has primary fO_2 that ranges from that of primary MORB mantle (QFM) where slab fluid influences are minor (Ba/La ~ 5), increasing as slab fluid influence increases, up to QFM+0.50 (Ba/La ~ 13). The southern Mariana trough has primary fO_2 that is slightly more oxidized than the northern Mariana trough (QFM+0.5), with evidence for greater slab fluid influence (Ba/La ~ 16). Primary melts from NW Rota-1 have $fO_2 \sim$ QFM+0.6, which is only slightly elevated over the southern Mariana trough primary fO_2 . Northwest Rota-1 also sits farther from the trench and the slab surface than the rest of the Mariana arc, and records a smaller slab fluid influence (Ba/La ~ 17). Within the arc, increasing Ba/La ratio correlates with increasing average primary fO_2 from NW Rota-1 to Guguan (Ba/La ~ 48 , QFM+1.6). A positive relationship between Ba/La ratio and fO_2 is also observed within individual calculated primary melts at Pagan volcano ($R^2 = 0.77$), although their fO_2 s overlap within uncertainty. These observations link oxidation to subduction influence, specifically with Ba-enriched fluids derived from the subducted slab. Small additions of slab fluids (or possibly different fluids) in the back-arc increase primary fO_2 in the mantle wedge up to 5 times that of MOR primary fO_2 . Elevated slab fluid additions under the volcanic arc increase primary fO_2 up to \sim QFM+1.6. These conclusions have several important implications for potential buffering assemblages in the mantle wedge and the fO_2 of slab fluids.

Taken together, these results suggest that slab-derived, Ba-rich fluids are significantly more oxidized than the upper mantle. There is strong evidence that the slab lithosphere is highly

serpentinized prior to subduction (Ivandic *et al.*, 2008, Ranero *et al.*, 2003, Savage, 2012, Van Avendonk *et al.*, 2011) and deserpentinization reactions (dehydrating serpentinite assemblages) in the subducting slab may contribute a significant proportion of the fluids that lead to the formation of arc magmas (Hacker, 2008, Schmidt & Poli, 1998, van Keken *et al.*, 2011).

Serpentinization reactions that occur on the seafloor prior to subduction involve the infiltration of fluids (e.g., seawater) into peridotite. Iron is oxidized, transforming Fe^{2+} contained in olivine into Fe^{3+} to form magnetite at the expense of oxygen contained in H_2O molecules. This reaction generates magnetite, brucite, and serpentine coexisting with reduced aqueous fluids (Frost, 1985) that are ultimately lost from the system, resulting in a net oxidation of the rock. When the slab travels along a prograde P-T path during subduction, serpentinite minerals become unstable at $\sim 600^\circ \text{C}$ and release aqueous fluids (e.g., Ulmer & Trommsdorff, 1995, Spandler *et al.*, 2014), which happens at 150-180 km depth for the southern Mariana subducting slab geotherm (van Keken *et al.*, 2011). The deserpentinization reactions over the P-T path of subducting slabs are complicated, but these may potentially consume magnetite and serpentine minerals to form olivine, which would reduce Fe and create oxidized fluids (e.g., Nozaka, 2005) or fluids carrying oxidized species (e.g., sulfate or SO_2 ; Alt *et al.*, 2013). These oxidized fluids must percolate through the subducting slab, where they may scavenge Ba from the altered oceanic crust and overlying sediment package, before ultimately entering the mantle wedge where they lower the peridotite solidus and generate oxidized hydrous melts with high Ba/La ratios under the volcanic arc. Additionally, there is a distinct contrast with the $f\text{O}_2$ of primary melts under the back-arc, where subduction influence is lower than the arc and the fluid composition is fundamentally different. This may be because 1) the influence from oxidized slab fluids is less and thus the oxidizing power of the slab fluids is diminished beneath the back-arc, and/or 2) the

fluids that are generated by the dehydrating slab that reach the back-arc have different sources from those fluids that contribute to arc volcanism and perhaps are not as oxidized. It is unlikely that fluids percolate through the entire volume of the mantle wedge. Rather, they may concentrate in rising diapirs or along interconnected networks (e.g., Hall & Kincaid, 2001, Marchall & Schumacher, 2012). This limits the proportion of mantle wedge that interacts with slab fluids significantly, and may make it possible for slab fluids to create oxidized primary melts that relate linearly to the extent of slab fluid influence. Fingerprinting the source of fluids from within the slab is a major challenge in subduction zone studies, and requires further investigation to test explicitly.

It is also possible that the mantle wedge contains important buffering assemblages that control the mantle source fO_2 for arc basalts, although the relationship between slab fluid influence (Ba/La) and primary fO_2 in Figure 10c indicates that there are no buffering species present in the mantle wedge in this range of fO_2 . Sulfur speciation is shown to be highly sensitive to changes in fO_2 between QFM and QFM+2.0 (Jugo, 2009, Jugo *et al.*, 2010). If a solid sulfide phase exists in the mantle wedge and is not exhausted during melting under the volcanic arc, the solid sulfide-sulfate phase boundary may serve to buffer the mantle wedge during melting, such that increasing the influence of oxidized slab fluids cannot increase primary fO_2 until either the sulfur phase is exhausted or another, more oxidized phase is added (e.g., Fe_2O_3 ; Mungall, 2002). The complete conversion of S^{2-} to S^{6+} does not occur until QFM+2 (Jugo *et al.*, 2010), about 5 times more oxidized than the most oxidized primary melts calculated in this work. In subduction zones where slab fluid influence is greater, slab fluids may be capable of oxidizing the mantle wedge up to the point of sulfide destabilization, at which point the fO_2 of the mantle wedge may be buffered until all sulfide is transformed to sulfate.

CONCLUSIONS

This combined study of submarine basaltic glasses and olivine hosted melt inclusions from six Mariana arc volcanoes and the Mariana trough examines the variations in $\text{Fe}^{3+}/\Sigma\text{Fe}$ ratios along several liquid lines of descent and across tectonic setting and slab contributions. Mariana arc glasses and melt inclusions preserve liquid lines of descent that take the general form of olivine \pm clinopyroxene \pm plagioclase crystallization with simultaneous $\text{CO}_2 \pm \text{H}_2\text{O} \pm \text{S}$ degassing. In all cases, arc melt inclusions and submarine glasses are more oxidized than MORB glasses with similar MgO contents. The composition and $\text{Fe}^{3+}/\Sigma\text{Fe}$ ratios of arc melt inclusions and submarine glasses cannot be recreated by simple fractional crystallization of a MOR-like primary melt. Sulfur degassing, where evidenced in this study, may play a role in reducing arc magmas during differentiation in the arc crust at Agrigan and Alamagan volcanoes, but not necessarily at other Mariana arc volcanoes. Submarine glasses from the Mariana trough preserve a liquid line of descent that takes the form of olivine \pm plagioclase \pm clinopyroxene \pm magnetite crystallization with simultaneous $\text{CO}_2 + \text{H}_2\text{O} \pm \text{S}$ degassing. Mariana trough glasses are slightly more oxidized than MORB with similar MgO contents, but are not as oxidized as arc samples. The calc-alkaline affinity and magmatic $f\text{O}_2$ s correlate between MORB, Mariana trough, and arc samples, suggesting that $f\text{O}_2$, as well as water, plays a role in influencing the differentiation style of basalts. Reconstructed primary melts for arc and back-arc basalts reveal that the mantle source $f\text{O}_2$ at both back-arc and arc volcanoes are elevated over MORB mantle source. The mantle source for arc volcanoes is on average, about one order of magnitude more oxidized than the mantle source for the back-arc, and about 1.3 orders of magnitude more oxidized than the mantle source for MORBs. Primary $f\text{O}_2$ correlates with slab fluid indices (Ba/La) from the back-arc to the arc, as well as between arc volcanic centers and among discrete samples from Pagan volcano,

linking the oxidized nature of back-arc and arc basalts to slab fluid influence. The arc source may be more oxidized than the back-arc source due to a greater role for subduction influence, and/or to variable fluid composition. It is possible that slab fluids are oxidized as a result of deserpentinization reactions in the subducting slab, although further data is necessary to test this hypothesis.

ACKNOWLEDGEMENTS

We are very grateful for thorough and thoughtful reviews from Carl Spandler, Ian Parkinson, Cyn-Ty Lee, and John MacLennan. These reviews improved this manuscript significantly. Terry Plank and Yoshi Tamura generously shared sample material used in this study. Tony Lanzirotti and Sue Wirick assisted in all aspects of beamline operations and analysis related to the collection of μ -XANES data. Marion Lytle and Tim Rose shared their expertise in LA-ICPMS and EPMA analysis, respectively. We would like to thank the captain and crew of the R/V Thomas G. Thompson for their efforts during the TN273 cruise. Access to the National Synchrotron Light Source, Brookhaven National Laboratory was supported by the US Department of Energy, Office of Science, Office of Basic Energy Sciences, under Contract No. DE-AC02-98CH10886. We acknowledge support from Smithsonian's Scholarly Studies Program (EC), NSF MARGINS-EAR-0841108 (KK), NSF OCE-0961559 (KK), and NSF MARGINS-EAR-0841006 (EC). NSF OCE-1258771 provides curatorial support for geological samples at the University of Rhode Island.

FIGURE CAPTIONS

Figure 1: Location map for samples used in this study. All colored symbols for Agrigan, Alamagan, Guguan, and Sarigan volcanoes, as well as the solid blue square for Pagan volcano represent olivine hosted melt inclusions. Checkered square for Pagan volcano, cross for NW Rota-1 volcano, and light grey inverted triangles along the Mariana trough represent submarine glasses. Dark grey triangles in the northern Mariana trough are seafloor glasses from Kelley and Cottrell (2009) and Newman *et al.* (2000). The basemap was created using GeoMapApp (<http://www.geomapapp.org>; Ryan *et al.*, 2009).

Figure 2: Representative photomicrographs of melt inclusions in this study. (a) Melt inclusion Gug23-02-01 is doubly polished and the photomicrograph is taken in cross polarized light. (b) Sari15-04-25, (c) Ala03-01, and (d) Agri07-06 are doubly exposed melt inclusions and photomicrographs are taken in transmitted light.

Figure 3: Major element variations for Mariana arc melt inclusions and submarine glasses (a-d) and back-arc submarine glasses (e-h). All symbols are as in Figure 1. Black line in panels e – h show the trajectory of $olv \pm plag \pm cpx \pm mgt$ fractionation, generated using Petrolog3 (Danyushevsky & Plechov, 2011) fractionating the composition of 80-1-3 (VG10498) at 1.5 kbar, using mineral melt models of Roeder and Emslie (1970), Danyushevsky (2001), and Ariskin and Barmina (1999) in a system closed to oxygen. FeO* is total Fe expressed as FeO. Error bars are shown in the lower left hand corner of each plot, in panels (a) through (d).

Figure 4: Volatile element variations for Mariana arc melt inclusions and back-arc submarine glasses. Textured regions in panels (a) and (b) are melt inclusion data from (Shaw *et al.*, 2008) and Kelley *et al.* (2010), shown for comparison. (a) Plot of H₂O vs. CO₂ variation. Isobars and open system degassing curve were calculated for a basalt at 1200°C using VolatileCalc (Newman & Lowenstern, 2002). Error associated with H₂O concentrations are ~0.25 wt% and

~75 ppm for CO₂ concentrations. (b) Plot of S vs. H₂O concentrations. Model curve for concomitant S and H₂O degassing are semi-empirical and taken from Wade *et al.* (2006, small cross) and Sisson and Layne (1993, black square). Dashed line represents the extension of the degassing trajectory to high sulfur concentrations. Black star represents an approximately degassed magma. (c) Fe³⁺/ΣFe ratios vs. H₂O concentrations for Mariana arc melt inclusions from this study as well as from Kelley and Cottrell (2012, light grey diamonds), and back-arc submarine glasses. Grey MORB field are data taken from Cottrell and Kelley (2011). Additional melt inclusions in this panel are from Kelley and Cottrell (2009), shown for comparison. Error bars are shown in the upper left hand corner of each plot.

Figure 5: (a) Fe³⁺/ΣFe ratios vs. MgO concentrations for Mariana arc melt inclusions from this study as well as from Kelley and Cottrell (2012, light grey diamonds), submarine glasses from Pagan and NW Rota-1 volcanoes, and submarine glasses from the Mariana trough. Grey field represents global MORB glass data from Cottrell and Kelley (2011). Black line is the trajectory of olv±plag±cpx±mgt fractionation, as in Figure 2. Dashed purple line is the trajectory of isobaric olv±cpx±plag fractionation from a starting composition similar to the composition of melt inclusion Agri04-05, generated using Petrolog3 (Danyushevsky & Plechov, 2011) at 1 kb, using mineral-melt models of Roeder and Emslie (1970) and Danyushevsky (2001) in a system closed to oxygen. (b) Magmatic *f*O₂, plotted relative to the QFM buffer vs. MgO for the same samples. Oxygen fugacities and the position of the QFM buffer (Frost, 1991) are calculated at the pressures and temperatures of melt inclusion entrapment using the algorithm of Kress and Carmichael (1991). Pressures for each melt inclusion suite are taken as the average pressure of entrapment recorded by CO₂-H₂O contents of the inclusions in the suite (Newman & Lowenstern, 2002). Temperatures for each melt inclusion suite are taken as the average olivine-

liquid temperature of the inclusions in the suite (Putirka *et al.*, 2007). The dashed black line marks the position of QFM. Error bars are shown in the lower left hand corner of each plot.

Figure 6: $\text{Fe}^{3+}/\Sigma\text{Fe}$ ratios vs. S concentrations for melt inclusions from Agrigan, Pagan, Guguan, Sarigan, and Alamagan volcanoes, as well as melt inclusions from Agrigan volcano from Kelley and Cottrell (2012, light grey diamonds). The black line with tick marks is a model for S degassing and associated Fe reduction, taken from Kelley and Cottrell (2012). Error bars are shown in the upper left hand corner.

Figure 7: Tholeiitic index (THI) versus (a) pre-eruptive H_2O content and (b) magmatic $f\text{O}_2$ relative to the QFM buffer. THI calculations, small circles in panel (a) and the black line are from Zimmer *et al.* (2010). The grey line marks the boundary between tholeiitic and calc-alkaline differentiation trends, as defined by Zimmer *et al.* (2010). Magmatic $f\text{O}_2$ s are calculated as in figure 5. Brown square represents the average of MORB data from Cottrell and Kelley (2011). Grey triangle represents both northern and southern Mariana trough samples from this study. Error bars for H_2O and magmatic $f\text{O}_2$ represent the standard deviation of the sample population from the average. Error bars for THI represent the minimum and maximum estimates of THI, based on the available data for each location.

Figure 8: Histogram showing calculated primary $f\text{O}_2$ (ΔQFM) for several tectonic regimes. MORB data are calculating by adding equilibrium olivine compositions in 0.1% increments to the compositions of MORB glasses with $\text{MgO} > 7$ wt%, data taken from Cottrell and Kelley (2011). Pressures and temperatures of melt generation were calculated using the Si-thermobarometer of Lee *et al.* (2009). Oxygen fugacities were calculated from $\text{Fe}^{3+}/\Sigma\text{Fe}$ ratios after Kress and Carmichael (1991). Gray bars with dashes represent primary $f\text{O}_2$ s for Agrigan volcano, calculated by Kelley and Cottrell (2012). The dashed line marks the position of QFM,

which is equal to the approximate primary fO_2 for MORB source mantle (Cottrell & Kelley, 2011).

Figure 9: (a) Th/La, (b) Ba/La, and (c) Zr/Y vs. Sm/La for melt inclusions, submarine glasses from Pagan and NW Rota-1 volcanoes, and southern Mariana trough submarine glasses. The grey field is Pacific MORB data from Niu and Batiza (1997), shown for comparison. Data for discrete materials from the Pacific plate taken from ODP sites 800 and 801 are shown as small black and white stars, respectively, and their calculated bulk compositions are shown as large black and white stars (Plank & Langmuir, 1998). Orange and green dashed lines show approximate mixing lines between the suggested arc mantle source composition (black circle; Plank, 2005) and various discrete components of the sediments at ODP Sites 800 and 801. The solid black line is an approximate mixing line between the suggested back-arc mantle source composition (grey circle; Stolper & Newman, 1994) and the bulk composition of sediments at ODP Site 801. Dashed black lines in panel (b) show approximate mixing trajectories to fluids of unconstrained composition.

Figure 10: Primary fO_2 (ΔQFM) vs. (a) Zr/Y, (b) Th/La, and (c) Ba/La for MORB (black circles), northern Mariana trough (dark grey triangles), southern Mariana trough (light grey triangle), NW Rota-1 submarine volcano (black cross), and Agrigan (purple diamond), Alamagan (green circle), Pagan (blue square), Sarigan (orange star), and Guguan (yellow hexagon) volcanoes. MORB data are from Cottrell and Kelley (2013). In (c), large saturated symbols represent the average calculated primary fO_2 and measured Ba/La ratio for each volcano. The error bars on these symbols represent the standard deviation of the population from the average value. The linear regression statistics for these average values are shown in black ($R^2 = 0.86$, $P < 0.01$). The linear regression statistics for the entire dataset are shown in gray ($R^2 =$

0.65, $P < 0.05$). The bold dashed line marks the position of QFM, which is equal to the approximate primary fO_2 for MORB source mantle (Cottrell & Kelley, 2011). Individual primary melt compositions for each location are shown as small symbols. The short-dashed, thin black line is a standard linear regression through the average fO_2 and Ba/La ratio for the MORB, all of the northern Mariana trough data, and the average fO_2 and Ba/La ratio for the southern Mariana trough and each of the volcanic centers.

REFERENCES CITED

- Alt, J. C., Schwarzenbach, E. M., Fröh-Green, G. L., Shanks, W. C., Bernasconi, S. M., Garrido, C. J., Crispini, L., Gaggero, L., Padrón-Navarta, J. A. & Marchesi, C. (2013). The role of serpentinites in cycling of carbon and sulfur: Seafloor serpentinization and subduction metamorphism. *Lithos* 178, 40-54.
- Alt, J. C. & Teagle, D. A. H. (2003). Hydrothermal alteration of upper oceanic crust formed at a fast-spreading ridge: mineral, chemical and isotopic evidence from ODP Site 801. *Chemical Geology* 201, 191-211.
- Anderson, A. T. (1973). Evidence for a Picritic, Volatile-rich Magma beneath Mt. Shasta, California. *Journal of Petrology* 15, 243-257.
- Ariskin, A. & Barmina, G. (1999). An empirical model for the calculation of spinel-melt equilibria in mafic igneous systems at atmospheric pressure: 2. Fe-Ti oxides. *Contributions to Mineralogy and Petrology* 134, 251-273.
- Ballhaus, C. (1993). Redox states of lithospheric and asthenospheric upper mantle. *Contributions to Mineralogy and Petrology* 114, 331-348.

- Bezos, A. & Humler, E. (2005). The $\text{Fe}^{3+}/\Sigma\text{Fe}$ ratios of MORB glasses and their implications for mantle melting. *Geochimica et Cosmochimica Acta* 2005, 711-725.
- Bloomer, S. H., Stern, R. J., Fisk, E. & Geshwind, C. H. (1989). Shoshonitic volcanism in the northern Mariana arc 1. Mineralogic and major and trace element characteristics. *Journal of Geophysical Research* 94, 4469-4496.
- Botcharnikov, R. E., Almeev, R. R., Koepke, J. & Holtz, F. (2008). Phase Relations and Liquid Lines of Descent in Hydrous Ferrobasalt--Implications for the Skaergaard Intrusion and Columbia River Flood Basalts. *Journal of Petrology* 49, 1687-1727.
- Bryndzia, L. T. & Wood, B. J. (1990). Oxygen thermobarometry of abyssal spinel peridotites: the redox state and C-O-H volatile composition of the Earth's sub-oceanic upper mantle. *American Journal of Science* 290, 1093-1117.
- Bucholz, C. E., Gaetani, G. A., Behn, M. D. & Shimizu, N. (2013). Post-entrapment modification of volatiles and oxygen fugacity in olivine-hosted melt inclusions. *Earth and Planetary Science Letters* 374, 145-155.
- Canil, D. (2002). Vanadium in peridotites, mantle redox and tectonic environments: Archean to present. *Earth and Planetary Science Letters* 195, 75-90.
- Carroll, M.R., & Rutherford, M. J. (1988). Sulfur speciation in hydrous experimental glasses by varying oxidation state: Results from measured wavelength shifts of sulfur X-rays. *American Mineralogist* 73, 845-849.
- Carmichael, I. S. E. (1991). The redox states of basic and silicic magmas: a reflection of their source regions? *Contributions to Mineralogy and Petrology* 106, 129-141.
- Christie, D. M., Carmichael, I. S. E. & Langmuir, C. H. (1986). Oxidation states of mid-ocean ridge basalt glasses. *Earth and Planetary Science Letters* 79, 397-411.

- Cottrell, E., Spiegleman, M. & Langmuir, C.H. (2002). Consequences of diffusive reequilibration for the interpretation of melt inclusions. *Geochemistry, Geophysics, Geosystems* **3**. doi: 10.1029/2001GC000205.
- Cottrell, E. & Kelley, K. A. (2011). The oxidation state of Fe in MORB glasses and the oxygen fugacity of the upper mantle. *Earth and Planetary Science Letters* **305**, 270-282.
- Cottrell, E. & Kelley, K. A. (2013). Redox heterogeneity in mid-ocean ridge basalts as a function of mantle source. *Science* **340**, 1314-1317.
- Cottrell, E., Kelley, K. A., Lanzirotti, A. & Fischer, R. A. (2009). High-precision determination of iron oxidation state in silicate glasses using XANES. *Chemical Geology* **268**, 167-179.
- Crabtree, S. M. & Lange, R. A. (2011). An evaluation of the effect of degassing on the oxidation state of hydrous andesite and dacite magmas: a comparison of pre- and post-eruptive Fe²⁺ concentrations. *Contributions to Mineralogy and Petrology* **163**, 209-224.
- Danyushevsky, L. V. (2001). The effect of small amounts of H₂O on crystallization of mid-ocean ridge and backarc basin magmas. *Journal of Volcanology and Geothermal Research* **110**, 265-280.
- Danyushevsky, L. V., Della-Pasqua, F. N. & Sokolov, S. (2000). Re-equilibration of melt inclusions trapped by magnesian olivine phenocrysts from subduction-related magmas: petrological implications. *Contributions to Mineralogy and Petrology* **138**, 68-83.
- Danyushevsky, L. V., McNeill, A. W. & V., S. A. (2002). Experimental and petrological studies of melt inclusions in phenocrysts from mantle-derived magmas: an overview of techniques, advantages and complications. *Chemical Geology* **183**, 5-25.
- Danyushevsky, L. V. & Plechov, P. (2011). Petrolog3: Integrated software for modeling crystallization processes. *Geochemistry Geophysics Geosystems* **12**, doi: 10.1029/2011gc003516.

- Dixon, J. E., Stolper, E. M. & Holloway, J. R. (1995). An Experimental Study of Water and Carbon Dioxide Solubilities in Mid-Ocean Ridge Basaltic Liquids. Part I. Calibration and Solubility Models. *Journal of Petrology* 36, 1607-1630.
- Elliott, T., Plank, T., Zindler, A., White, W. & Bourdon, B. (1997). Element transport from slab to volcanic front at the Mariana arc. *Journal of Geophysical Research* 102, 14991-15019.
- Frost, B. R. (1985). On the Stability of Sulfides, Oxides, and Native Metals in Serpentine. *Journal of Petrology* 26, 31-63.
- Frost, B. R. (1991). Introduction to oxygen fugacity and its petrologic importance. *Reviews in Mineralogy and Geochemistry*, 25, 1-9.
- Frost, B. R. & Ballhaus, C. (1998). Comment on "Constraints on the origin of the oxidation state of mantle overlying subduction zones: An example from Simcoe, Washington, USA". *Geochimica et Cosmochimica Acta* 62, 329-331.
- Fryer, P. (1996). Evolution of the Mariana convergent plate margin system. *Reviews of Geophysics* 34, 89-125.
- Gaetani, G.A., Grove, T.L., & Bryan, W.B. (1993) The influence of water on the petrogenesis of subduction related rocks. *Nature* 365, 332-334.
- Gaetani, G. A., O'Leary, J. A., Shimizu, N., Bucholz, C. E. & Newville, M. (2012). Rapid reequilibration of H₂O and oxygen fugacity in olivine-hosted melt inclusions. *Geology* 40, 915-918.
- Hacker, B. R. (2008). H₂O subduction beyond arcs. *Geochemistry, Geophysics, Geosystems* 9, 10.1029/2007gc001707.
- Hall, P. S. & Kincaid, C. (2001). Diapiric flow at subduction zones: a recipe for rapid transport. *Science* 292, 2472-2575.

Hickey-Vargas, R. & Reagan, M. (1987). Temporal variations of isotope and rare earth element abundances in volcanic rocks from Guam: implications for the evolution of the Mariana Arc.

Contributions to Mineralogy and Petrology 97, 497-508.

Irvine, T. N. & Baragar, R. A. (1971). A guide to the chemical classification of the common volcanic rocks. *Canadian Journal of Earth Sciences* 8, 523-548.

Ivandic, M., Grevemeyer, I., Berhorst, A., Flueh, E. R. & McIntosh, K. (2008). Impact of bending related faulting on the seismic properties of the incoming oceanic plate offshore of Nicaragua. *Journal of Geophysical Research* 113, 1253-1264.

Jarosewich, E., Nelen, J. & Norberg, J. (1980). Reference samples for electron microprobe analysis. *Geostandards Newsletter* 4, 43-47.

Jenner, F. E., O'Neill, H. S. C., Arculus, R. J. & Mavrogenes, J. A. (2010). The Magnetite Crisis in the Evolution of Arc-related Magmas and the Initial Concentration of Au, Ag and Cu. *Journal of Petrology* 51, 2445-2464.

Jochum, K. P., B., D. D., Rocholl, A., Stoll, B., Becker, S., Besmehn, A., Bessette, D., Dietze, H. J., Dulski, P., Erzinger, J., Hellbrand, E., P, H., Horn, I., Janssens, K., Jenner, G. A., Klein, M., McDonough, W. F., Maetz, M., Mezger, K., Munker, C., Nikogosian, I. K., Pickhardt, C., Raczek, I., Rhede, D., Seufert, H. M., Simalkin, S. G., Sobolev, A. V., Spettel, B., Straub, S., Vincze, L., Wallianos, A., Weckwerth, G., Weyer, S., Wolf, D. & Zimmer, M. (2006). The preparation and preliminary characterisation of eight geological MPI-DING reference glasses for in-situ microanalysis. *Geostandards and Geoanalytical Research* 24, 97-133.

Johnson, M.C. & Plank, T. (1999) Dehydration and melting experiments constrain the fate of subducted sediments. *Geochemistry Geophysics Geosystems* 1, doi: 10.1029/1999GC000014.

Jugo, P. J. (2009). Sulfur content at sulfide saturation in oxidized magmas. *Geology* 37, 415-418.

- Jugo, P. J., Wilke, M. & Botcharnikov, R. E. (2010). Sulfur K-edge XANES analysis of natural and synthetic basaltic glasses: Implications for S speciation and S content as function of oxygen fugacity. *Geochimica et Cosmochimica Acta* 74, 5926-5938.
- Kelley, K. A. & Cottrell, E. (2009). Water and the oxidation state of subduction zone magmas. *Science* 325, 605-607.
- Kelley, K. A. & Cottrell, E. (2012). The influence of magmatic differentiation on the oxidation state of Fe in a basaltic arc magma. *Earth and Planetary Science Letters* 329-330, 109-121.
- Kelley, K. A., Plank, T., Ludden, J. & Staudigel, H. (2003). Composition of altered oceanic crust at ODP Sites 801 and 1149. *Geochemistry Geophysics Geosystems* 4, doi: 10.1029/2002gc000435.
- Kelley, K. A., Plank, T., Newman, S., Stolper, E. M., Grove, T. L., Parman, S. & Hauri, E. H. (2010). Mantle melting as a function of water content beneath the Mariana arc. *Journal of Petrology* 51, 1711-1739.
- Kessel, R., Schmidt, M., Ulmer, P. & Pettke, T. (2005) Trace element signature of subduction-zone fluids, melts and supercritical liquids at 120-180 km depth. *Nature* 437, 724-727.
- Kincaid, C. & Hall, P. (2003). Role of back arc spreading in circulation and melting at subduction zones. *Journal of Geophysical Research* 108, 1-14.
- Klein, E. M. & Langmuir, C. H. (1987). Global correlations of ocean ridge basalt chemistry with axial depth and crustal thickness. *Journal of Geophysical Research* 94, 4241-4253.
- Kress, V. C. & Carmichael, I. S. E. (1991). The compressibility of silicate liquids containing Fe_2O_3 and the effect of composition, temperature, oxygen fugacity and pressure on their redox states. *Contributions to Mineralogy and Petrology* 108, 82-92.

- Langmuir, C. H., Bezos, A., Escrig, S. & Parman, S. W. (2006). Chemical systematics and hydrous melting of the mantle in back-arc basins. *Geophysical Monograph Series* 166, 87-146.
- Lecuyer, C. & Ricard, Y. (1999). Long-term fluxes and budget of ferric iron: implication for the redox states of the Earth's mantle and atmosphere. *Earth and Planetary Science Letters* 165, 197-211.
- Lee, C.-T. A., Leeman, W. P., Canil, D. & Li, Z.-X. A. (2005). Similar V/Sc Systematics in MORB and Arc Basalts: Implications for the Oxygen Fugacities of their Mantle Source Regions. *Journal of Petrology* 46, 2313-2336.
- Lee, C.-T. A., Luffi, P., Plank, T., Dalton, H. & Leeman, W. P. (2009). Constraints on the depths and temperatures of basaltic magma generation on Earth and other terrestrial planets using new thermobarometers for mafic magmas. *Earth and Planetary Science Letters* 279, 20-33.
- Lee, C. T., Luffi, P., Chin, E. J., Bouchet, R., Dasgupta, R., Morton, D. M., Le Roux, V., Yin, Q. Z. & Jin, D. (2012). Copper systematics in arc magmas and implications for crust-mantle differentiation. *Science* 336, 64-68.
- Lee, C. T., Luffi, P., Le Roux, V., Dasgupta, R., Albarede, F. & Leeman, W. P. (2010). The redox state of arc mantle using Zn/Fe systematics. *Nature* 468, 681-685.
- Liu, Y., Samaha, N.-T. & Baker, D. R. (2007). Sulfur concentration at sulfide saturation (SCSS) in magmatic silicate melts. *Geochimica et Cosmochimica Acta* 71, 1783-1799.
- Lloyd, A. S., Plank, T., Ruprecht, P., Hauri, E. H. & Rose, W. (2012). Volatile loss from melt inclusions in pyroclasts of differing sizes. *Contributions to Mineralogy and Petrology*.
- Luhr, J. F. (2001). Glass inclusions and melt volatile contents at Parícutin Volcano, Mexico. *Contributions to Mineralogy and Petrology* 142, 261-283.

Lytle, M. L., Kelley, K. A., Hauri, E. H., Gill, J. B., Papia, D. & Arculus, R. J. (2012). Tracing mantle sources and Samoan influence in the northwestern Lau back-arc basin. *Geochemistry, Geophysics, Geosystems* 13, 10.1029/2012gc004233.

Marchall, H. R. & Schumacher, J. C. (2012). Arc magmas sourced from melange diapirs in subduction zones. *Nature Geoscience* 5, 862-867.

Martindale, M., Skora, S., Pickles, J., Elliott, T., Blundy, J. & Avanzinelli, R. (2013). High pressure phase relations of subducted volcanoclastic sediments from the west pacific and their implications for the geochemistry of Mariana arc magmas. *Chemical Geology* 342, 94-109.

McCulloch, M. T. & Gamble, A. J. (1991). Geochemical and geodynamical constraints on subduction zone magmatism. *Earth and Planetary Science Letters* 102, 358-374.

Meijer, A. & Reagan, M. (1981). Petrology and geochemistry of the island of Sarigan in the Mariana Arc; Calc-alkaline volcanism in an oceanic setting. *Contributions to Mineralogy and Petrology* 77, 337-354.

Métrich, N., Berry, A. J., O'Neill, H. S. C. & Susini, J. (2009). The oxidation state of sulfur in synthetic and natural glasses determined by X-ray absorption spectroscopy. *Geochimica et Cosmochimica Acta* 73, 2382-2399.

Miyashiro, A. (1974). Volcanic rock series in island arcs and active continental margins. *American Journal of Science* 274, 321-355.

Mungall, J. (2002). Roasting the mantle: slab melting and the genesis of major Au and Au-rich Cu deposits. *Geology* 30, 915-918.

Newman, S. & Lowenstern, J. B. (2002). VolatileCalc: a silicate melt-H₂O-CO₂ solution model written in Visual Basic for excel. *Computers & Geosciences* 28, 597-604.

- Newman, S., Stolper, E. M. & Stern, R. J. (2000). H₂O and CO₂ in magmas from the Mariana arc and back arc systems. *Geochemistry Geophysics Geosystems* 1, doi: 10.1029/1999gc000027.
- Niu, Y. & Batiza, R. (1997). Trace element evidence from seamounts for recycled oceanic crust in the eastern Pacific mantle. *Earth and Planetary Science Letters* 148, 471-484.
- Nozaka, T. (2005). Metamorphic history of serpentinite mylonites from the Happo ultramafic complex, central Japan. *Journal of Metamorphic Geology* 23, 711-723.
- Osborn, E. F. (1959). Role of oxygen pressure in the crystallization and differentiation of basaltic magma. *American Journal of Science* 257, 609-647.
- Parkinson, I. J. & Arculus, R. J. (1999). The redox state of subduction zones: insights from arc-peridotites. *Chemical Geology* 160, 409-424.
- Parman, S. W., Grove, T. L., Kelley, K. A. & Plank, T. (2010). Along-Arc Variations in the Pre-Eruptive H₂O Contents of Mariana Arc Magmas Inferred from Fractionation Paths. *Journal of Petrology* 52, 257-278.
- Pearce, J. A. & Parkinson, I. J. (1993). Trace element models for mantle melting: application to volcanic arc petrogenesis. *Geological Society, London, Special Publications* 76, 373-403.
- Pearce, J. A., Stern, R. J., Bloomer, S. H. & Fryer, P. (2005). Geochemical mapping of the Mariana arc-basin system: Implications for the nature and distribution of subduction components. *Geochemistry Geophysics Geosystems* 6, doi: 10.1029/2004gc000895.
- Plank, T. (2005). Constraints from Thorium/Lanthanum on Sediment Recycling at Subduction Zones and the Evolution of the Continents. *Journal of Petrology* 46, 921-944.
- Plank, T., Kelley, K. A., Murray, R. W. & Stern, L. Q. (2007). Chemical composition of sediments subducting at the Izu-Bonin trench. *Geochemistry, Geophysics, Geosystems* 8, doi: 10.1029/2006gc001444.

- Plank, T. & Langmuir, C. H. (1993). Tracing trace elements from sediment input to volcanic output at subduction zones. *Nature* 362, 739-742.
- Plank, T. & Langmuir, C. H. (1998). The chemical composition of subducting sediment and its consequences for the crust and mantle. *Chemical Geology* 145, 325-394.
- Putirka, K. D., Perfit, M., Ryerson, F. J. & Jackson, M. G. (2007). Ambient and excess mantle temperatures, olivine thermometry, and active vs. passive upwelling. *Chemical Geology* 241, 177-206.
- Ranero, C. R., Phipps Morgan, J., McIntosh, K. & Reichert, C. (2003). Bending-related faulting and mantle serpentinization at the Middle America trench. *Nature* 425, 367-373.
- Ribeiro, J. M., Stern, R. J., Martinez, F., Ishizuka, O., Merle, S. G., Kelley, K., Anthony, E. Y., Ren, M., Ohara, Y., Reagan, M., Girard, G. & Bloomer, S. (2013). Geodynamic evolution of a forearc rift in the southernmost Mariana Arc. *Island Arc* 22, 453-476.
- Roeder, P. L. & Emslie, R. F. (1970). Olivine-Liquid Equilibrium. *Contributions to Mineralogy and Petrology* 29, 275-290.
- Rohrbach, A. & Schmidt, M. W. (2011). Redox freezing and melting in the Earth's deep mantle resulting from carbon-iron redox coupling. *Nature* 472, 209-212.
- Rowe, M. C., Kent, A. J. R. & Nielsen, R. L. (2009). Subduction Influence on Oxygen Fugacity and Trace and Volatile Elements in Basalts Across the Cascade Volcanic Arc. *Journal of Petrology* 50, 61-91.
- Ryan, W. B. F., Carbotte, S. M., Coplan, J. O., O'Hara, S., Melkonian, A., Arko, R., Weissel, R. A., Ferrini, V., Goodwillie, A., Nitsche, F., Bonczkowski, J. & Zemsky, R. (2009). Global Multi-Resolution Topography synthesis. *Geochemistry, Geophysics, Geosystems* 10, doi: 10.1029/2008gc002332.

- Savage, B. (2012). Seismic constraints on the water flux delivered to the deep Earth by subduction. *Geology* 40, 235-238.
- Schmidt, M. W. & Poli, S. (1998). Experimentally based water budgets for dehydrating slabs and consequences for arc magma generation. *Earth and Planetary Science Letters* 163, 361-379.
- Shaw, A. M., Hauri, E. H., Fischer, T. P., Hilton, D. R. & Kelley, K. A. (2008). Hydrogen isotopes in Mariana arc melt inclusions: Implications for subduction dehydration and the deep-Earth water cycle. *Earth and Planetary Science Letters* 275, 138-145.
- Sisson, T. W. & Grove, T. L. (1993). Experimental investigations of the role of H₂O in calc-alkaline differentiation and subduction zone magmatism. *Contributions to Mineralogy and Petrology* 113, 143-166.
- Sisson, T. W. & Layne, G. D. (1993). H₂O in basalt and basaltic andesite glass inclusions from four subduction-related volcanoes. *Earth and Planetary Science Letters* 117, 619-635.
- Spandler, C., Pettke, T. & Hermann, J. (2014) Experimental study of trace element release during ultrahigh-pressure serpentinite dehydration. *Earth and Planetary Science Letters* 391, 296-306.
- Spulber, S. & Rutherford, M. J. (1983). The origin of rhyolite and plagiogranite in oceanic crust: an experimental study. *Journal of Petrology* 24, 1-25.
- Stern, R. J. (1979). On the origin of andesite in the northern Mariana Island arc: Implications from Agrihan. *Contributions to Mineralogy and Petrology* 68, 207-219.
- Stolper, E. & Newman, S. (1994). The role of water in the petrogenesis of Mariana trough magmas. *Earth and Planetary Science Letters* 121, 293-325.

Syracuse, E. M. & Abers, G. A. (2006). Global compilation of variations in slab depth beneath arc volcanoes and implications. *Geochemistry, Geophysics, Geosystems* 7,doi:

10.1029/2005gc001045.

Tamura, Y., Ishizuka, O., Stern, R. J., Nichols, A. R. L., Kawabata, H., Hirahara, Y., Chang, Q., Miyazaki, T., Kimura, J. I., Embley, R. W. & Tatsumi, Y. (2013). Mission Immischible: Distinct subduction components generate two primary magmas at Pagan volcano, Mariana Arc. *Journal of Petrology*, 1-39.

Tamura, Y., Ishizuka, O., Stern, R. J., Shukuno, H., Kawabata, H., Embley, R. W., Hirahara, Y., Chang, Q., Kimura, J. I., Tatsumi, Y., Nunokawa, A. & Bloomer, S. H. (2011). Two Primary Basalt Magma Types from Northwest Rota-1 Volcano, Mariana Arc and its Mantle Diapir or Mantle Wedge Plume. *Journal of Petrology* 52, 1143-1183.

Tollstrup, D. L. & Gill, J. B. (2005). Hafnium systematics of the Mariana arc: Evidence for sediment melt and residual phases. *Geology* 33, 737-740.

Trail, D., Watson, E. B. & Tailby, N. D. (2011). The oxidation state of Hadean magmas and implications for early Earth's atmosphere. *Nature* 480, 79-82.

Ulmer, P. & Trommsdorff, V. (1995). Serpentine stability to mantle depths and subduction-related magmatism. *Science* 12, 858-861.

Van Avendonk, H. J. A., Holbrook, W. S., Lizarralde, D. & Denyer, P. (2011). Structure and serpentinization of the subducting Cocos plate offshore Nicaragua and Costa Rica.

Geochemistry, Geophysics, Geosystems 12, doi: 10.1029/2011gc003592.

van Keken, P. E., Hacker, B. R., Syracuse, E. M. & Abers, G. A. (2011). Subduction factory: 4. Depth-dependent flux of H₂O from subducting slabs worldwide. *Journal of Geophysical Research* 116, B01401.

Wade, J. A., Plank, T., Melson, W. G., Soto, G. J. & Hauri, E. H. (2006). The volatile content of magmas from Arenal volcano, Costa Rica. *Journal of Volcanology and Geothermal Research* 157, 94-120.

Wade, J. A., Plank, T., Stern, R. J., Tollstrup, D. L., Gill, J. B., O'Leary, J. C., Eiler, J. M., Moore, R. B., Woodhead, J. D., Trusdell, F., Fischer, T. P. & Hilton, D. R. (2005). The May 2003 eruption of Anatahan volcano, Mariana Islands: Geochemical evolution of a silicic island-arc volcano. *Journal of Volcanology and Geothermal Research* 146, 139-170.

Wallace, P. J. & Carmichael, I. S. E. (1991). Sulfur in basaltic magmas. *Geochimica et Cosmochimica Acta* 56, 1863-1874.

Wood, B. J., Bryndzia, L. T. & Johnson, K. E. (1990). Mantle oxidation state and its relationship to tectonic environment and fluid speciation. *Science* 248, 337-345.

Woodhead, J., Eggins, S. & Gamble, J. (1993). High field strength and transition element systematics in island arc and back-arc basin basalts; evidence for multi-phase melt extraction and a depleted mantle wedge. *Earth and Planetary Science Letters* 114, 491-504.

Woodhead, J. D. (1989). Geochemistry of the Mariana arc (western Pacific): Source composition and processes. *Chemical Geology* 1989, 1-24.

Zimmer, M. M., Plank, T., Hauri, E. H., Yogodzinski, G. M., Stelling, P., Larsen, J., Singer, B., Jicha, B., Mandeville, C. & Nye, C. J. (2010). The Role of Water in Generating the Calc-alkaline Trend: New Volatile Data for Aleutian Magmas and a New Tholeiitic Index. *Journal of Petrology* 51, 2411-2444.

Fig. 1

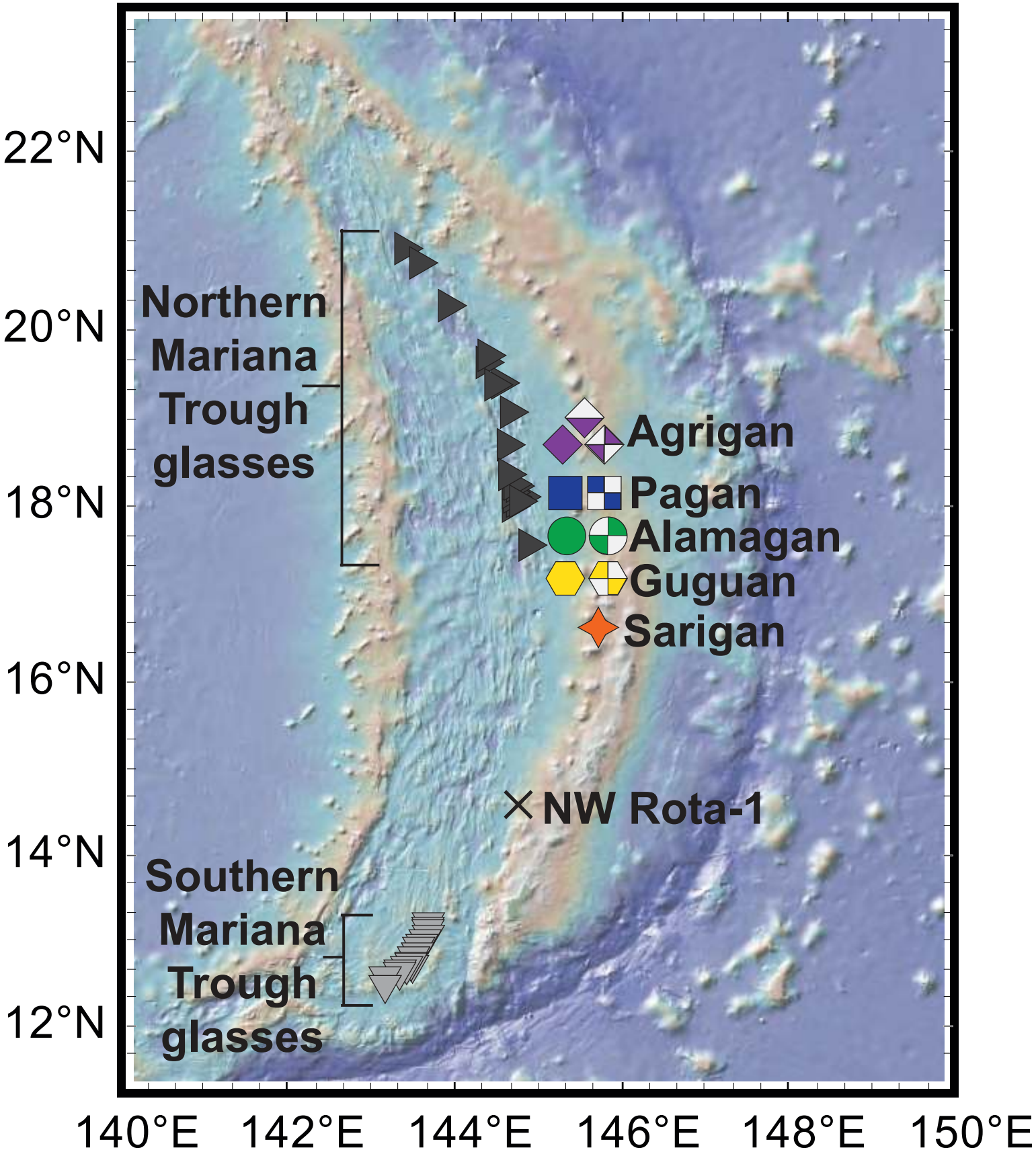


Fig. 2



1 mm

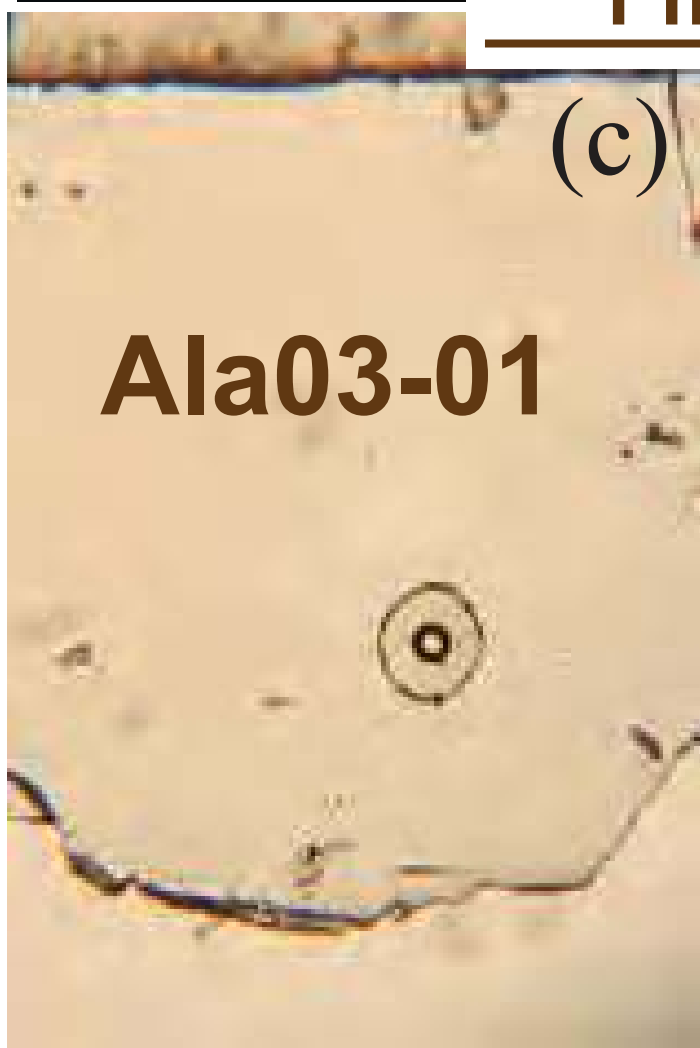


Fig. 3

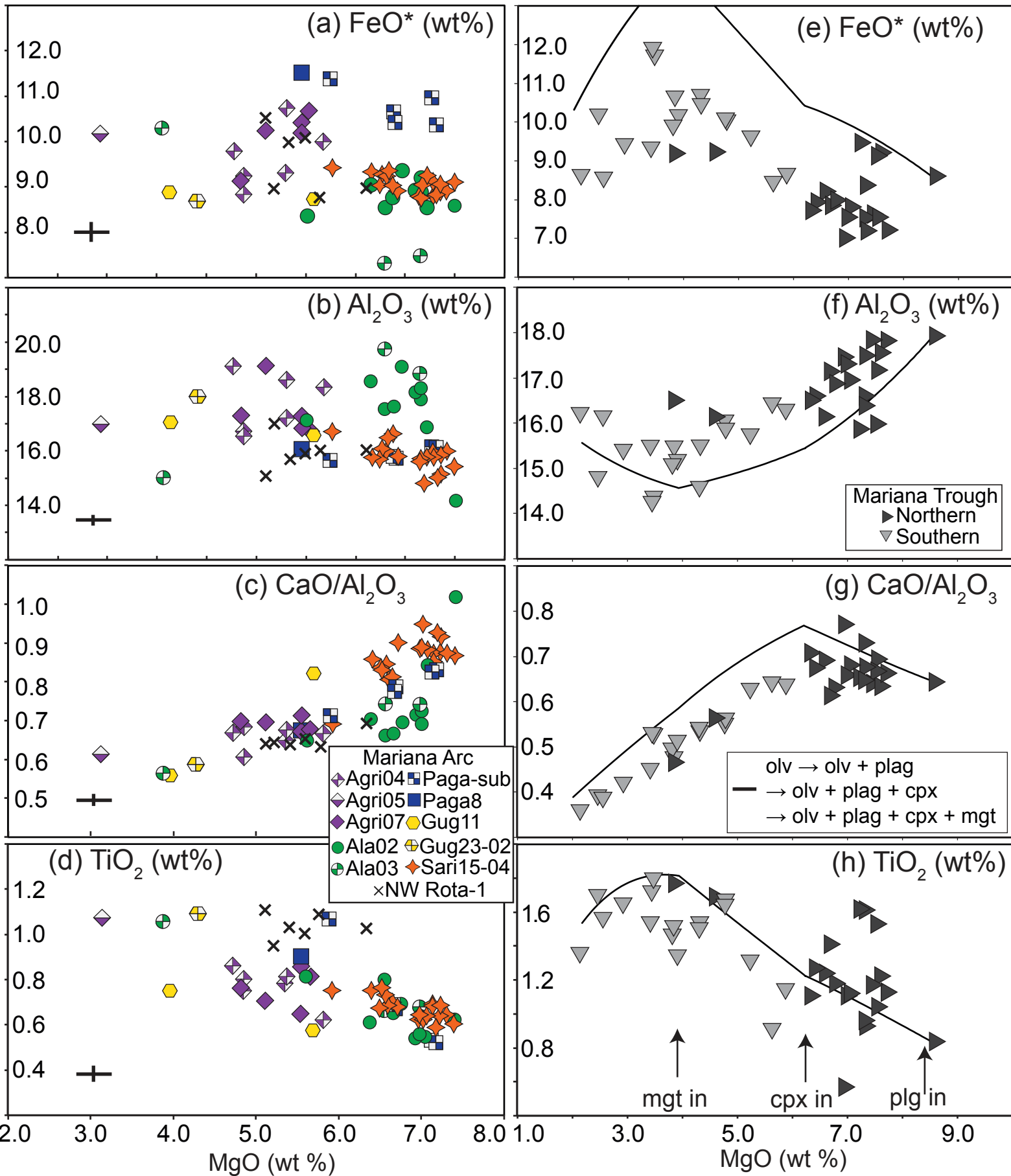


Fig. 4

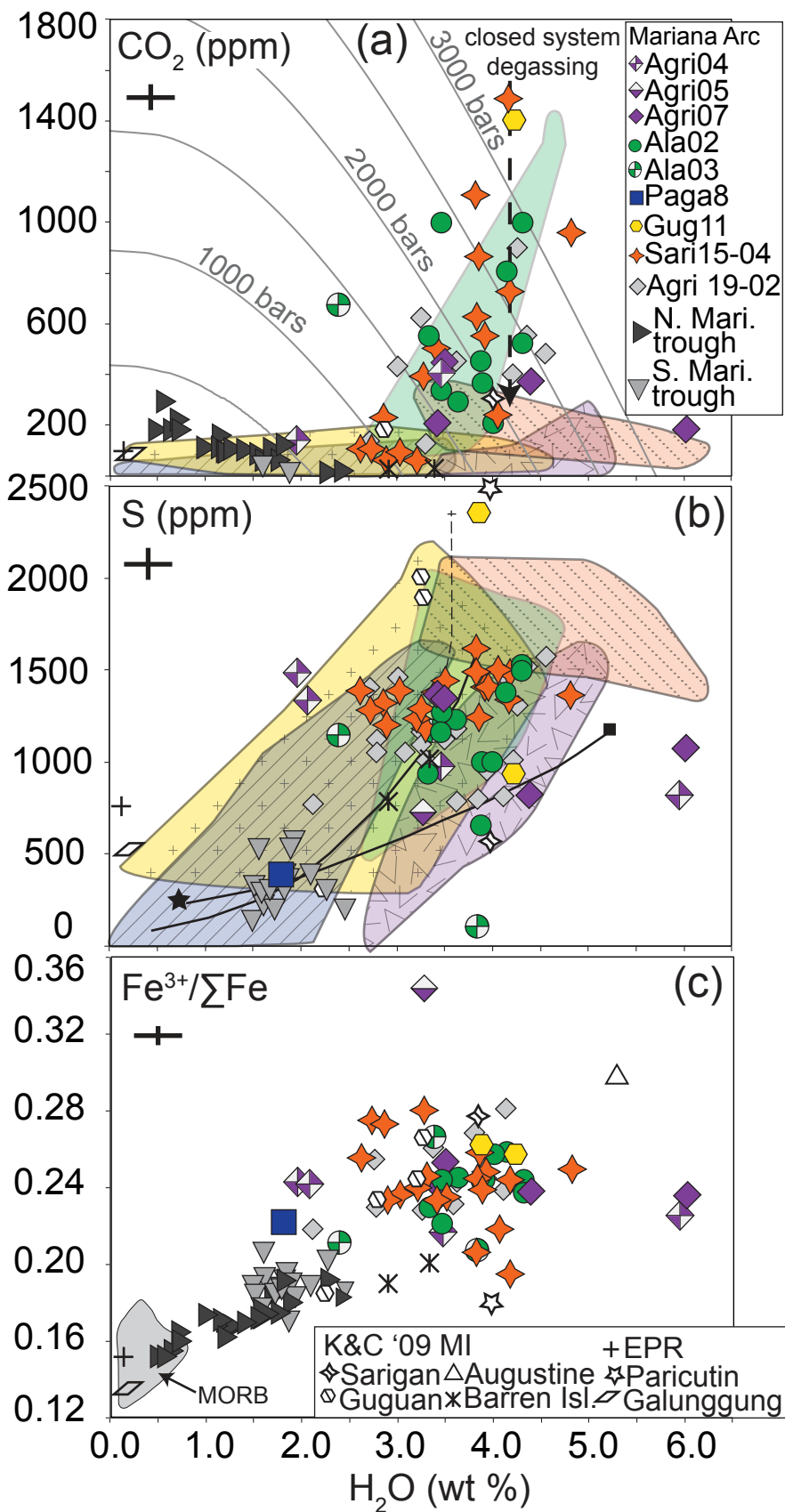


Fig. 5

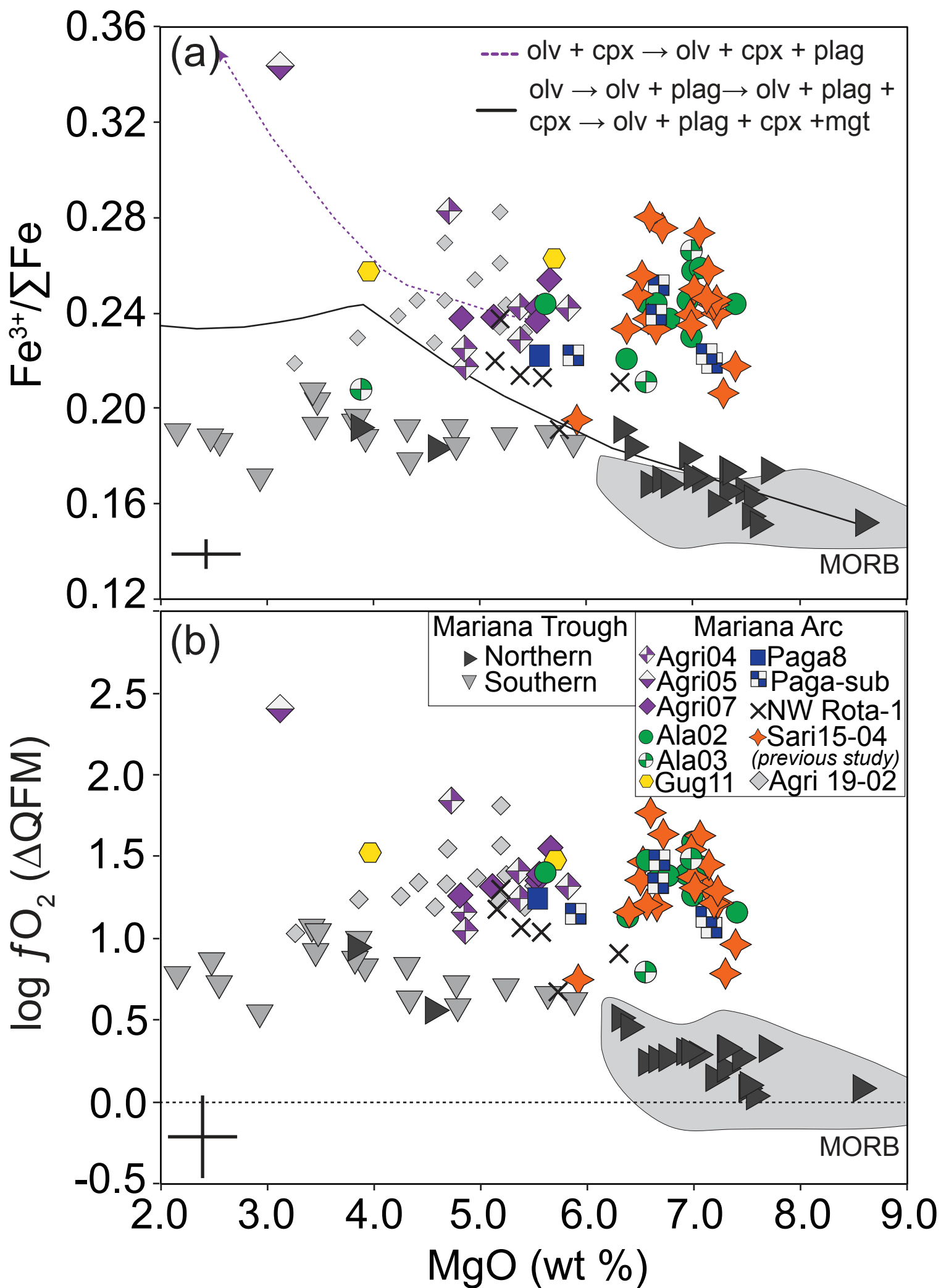


Fig. 6

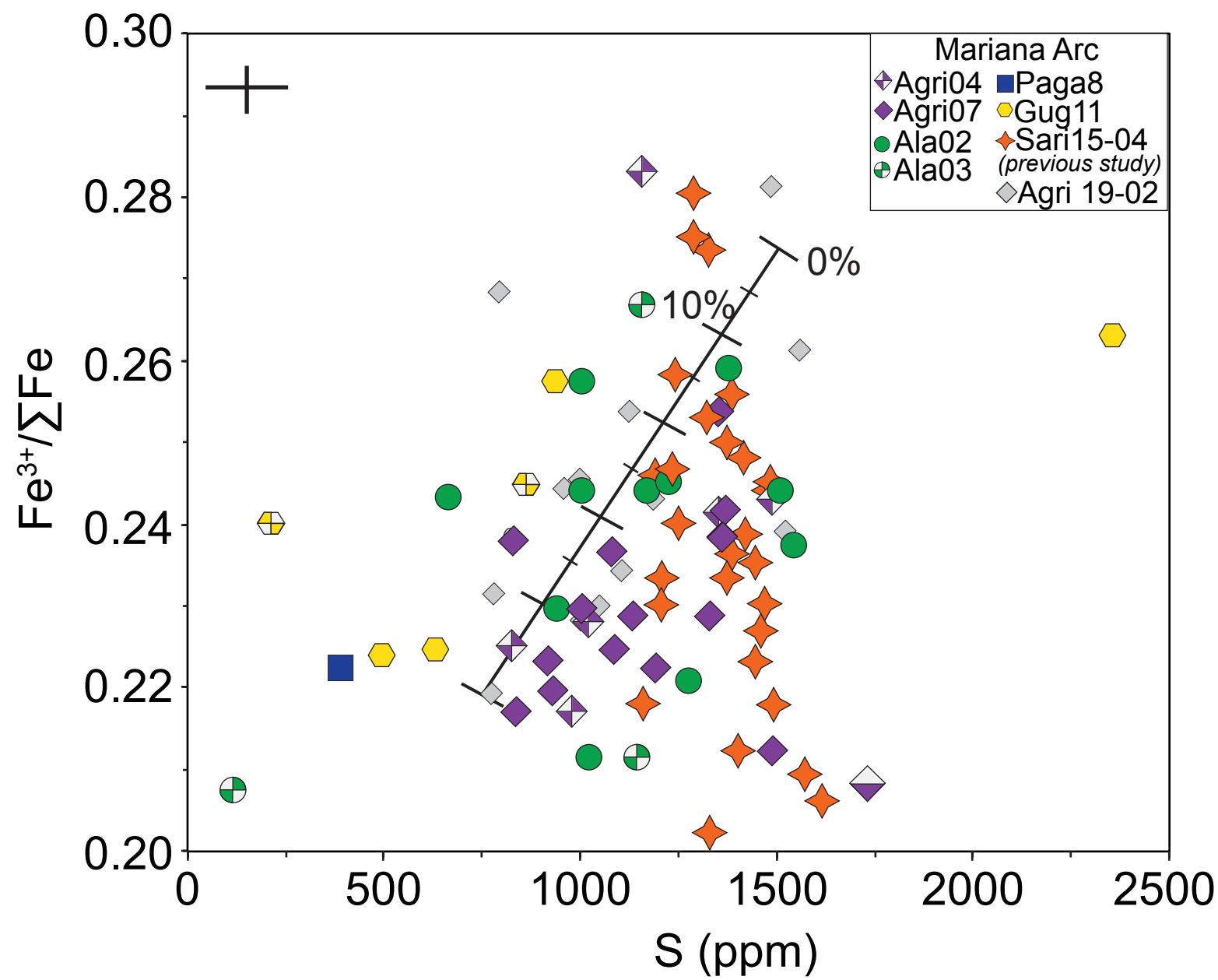


Fig. 7

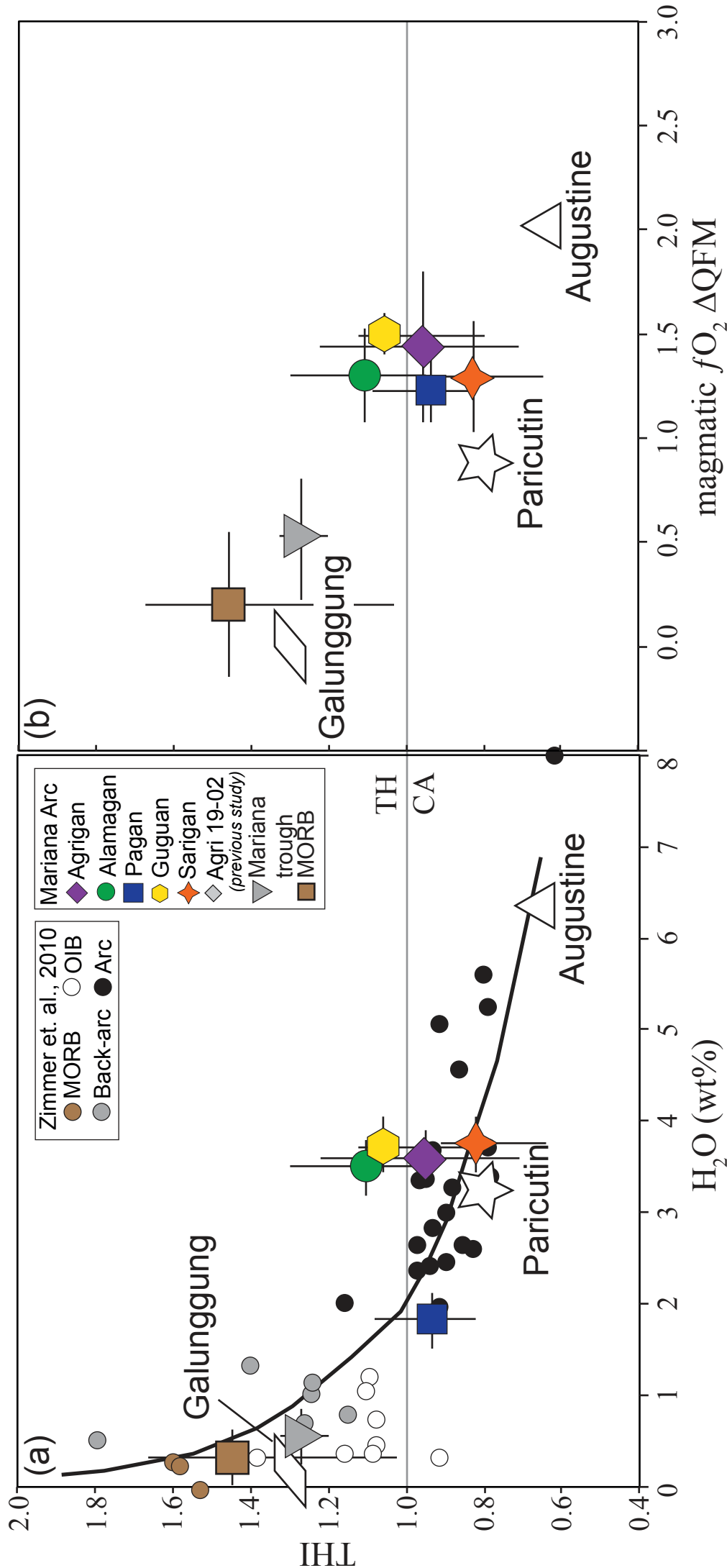


Fig. 8

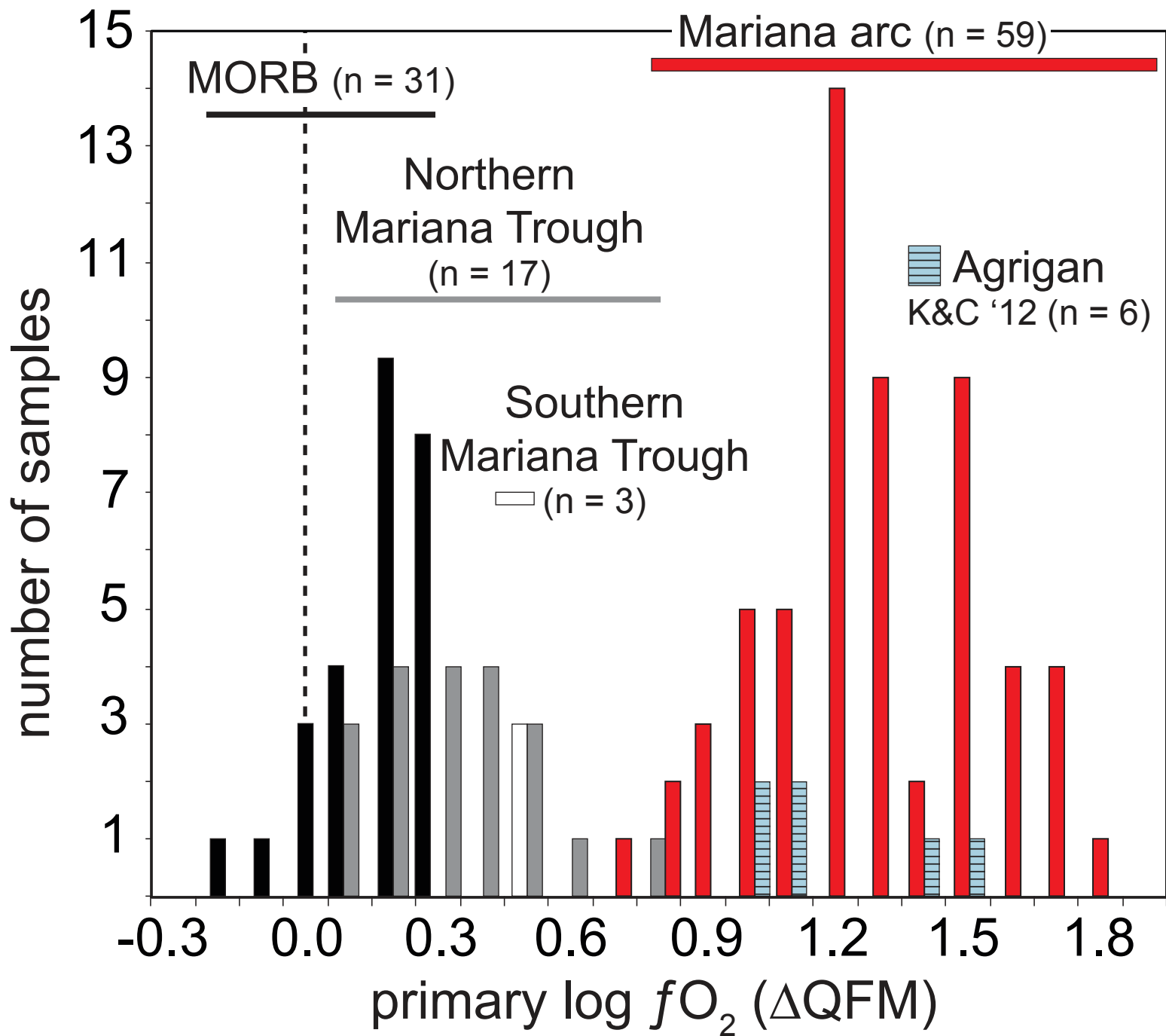


Fig. 9

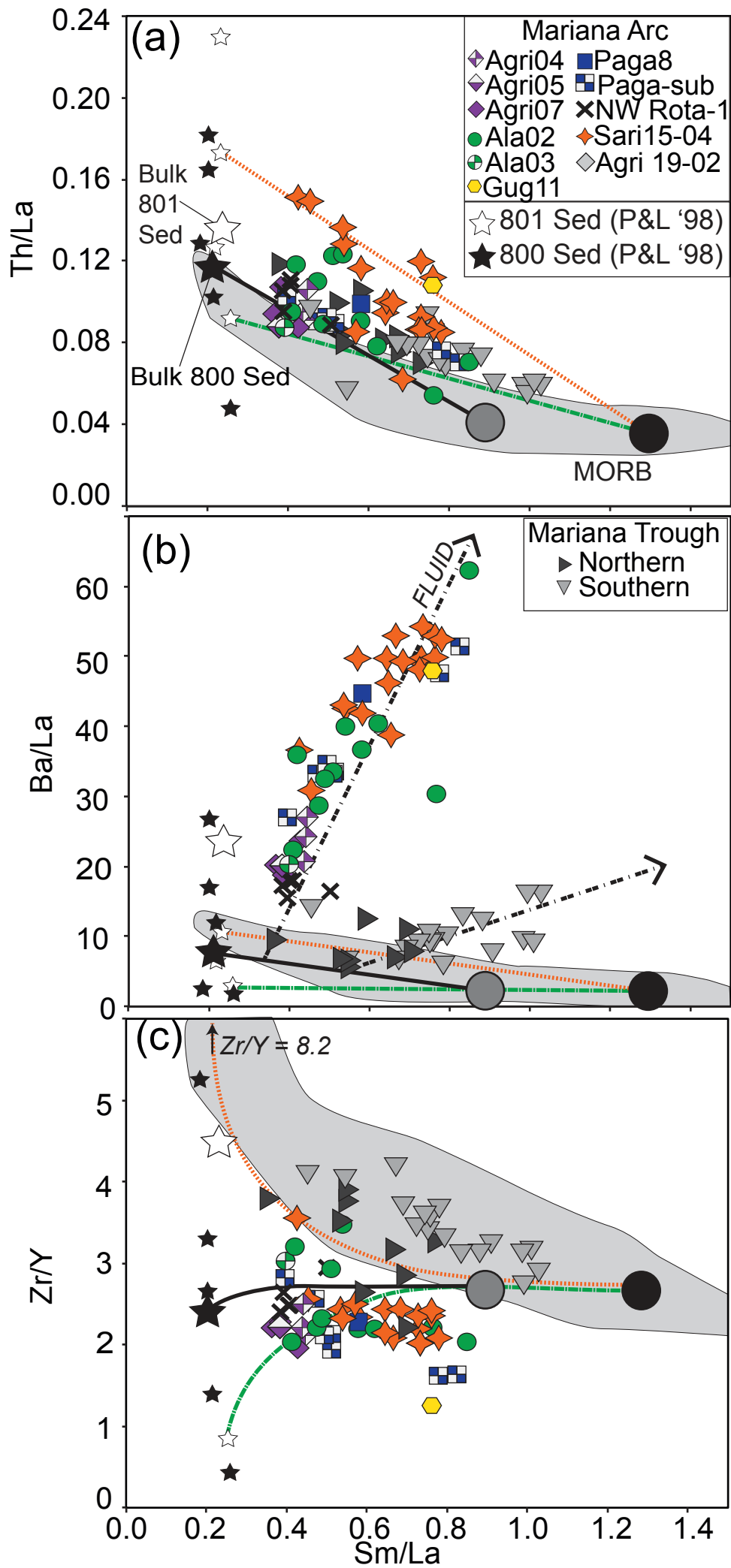
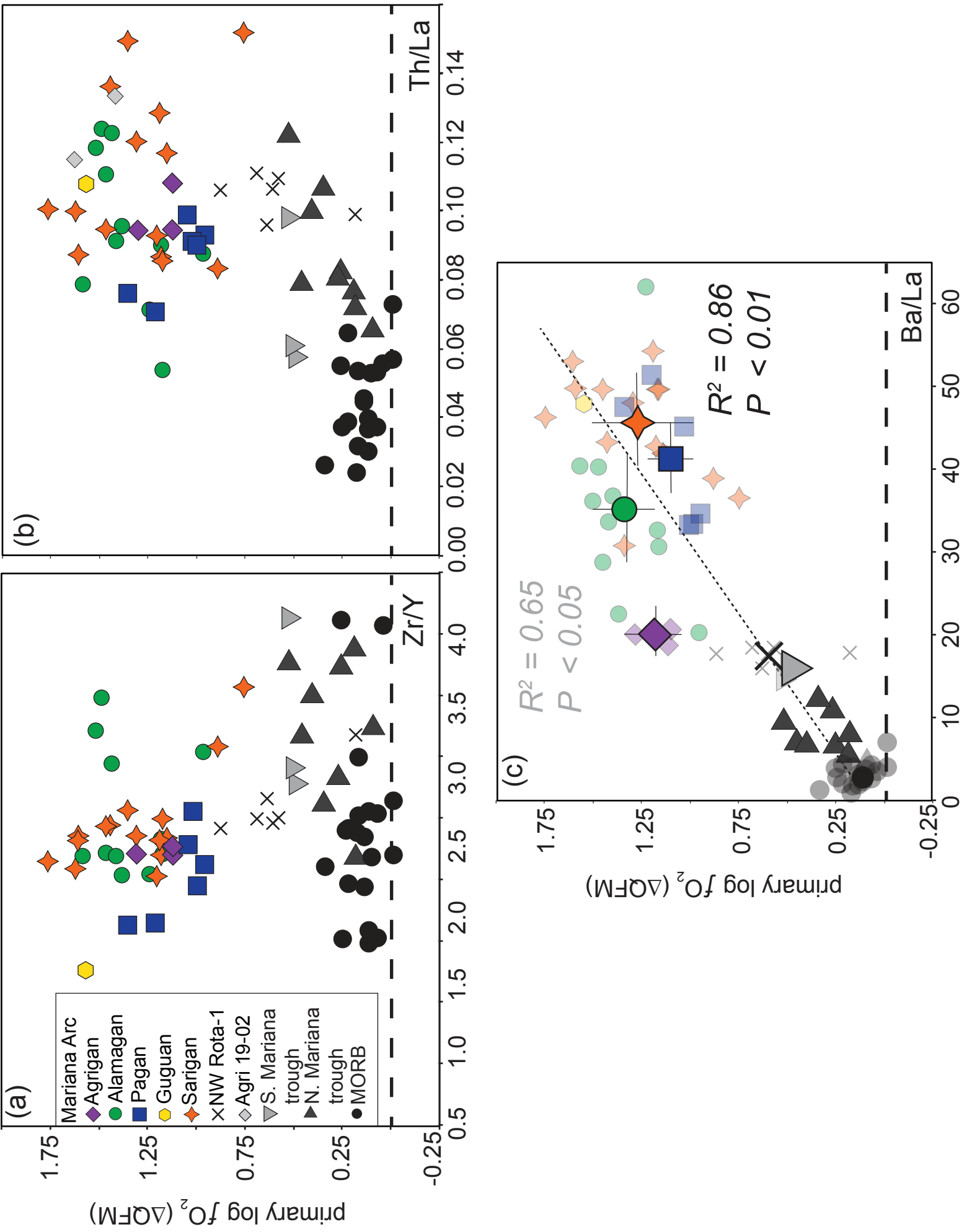


Fig. 10



Screening for olivine interference in Fe-μ-XANES spectra

When collecting Fe-μ-XANES spectra on olivine-hosted melt inclusions, it is important to avoid hitting the olivine crystal with the beam during analysis. Olivine contains several weight percent of Fe²⁺ and even a very small amount of olivine interference will “contaminate” the pre-edge structure of Fe-μ-XANES spectra collected for melt inclusions and bias the result towards more reduced values. The region of XANES spectra at higher energies than the Fe-Kα absorption edge contains information related to Fe-coordination and can be used to distinguish glass structure (random and on average, uncoordinated) from olivine signal (strong coordination, Fig. A1). All melt inclusion and seafloor glass spectra were visually inspected and compared to spectra taken on San Carlos olivine and standard glasses from Cottrell *et al.* (2009) in order to screen for crystal contamination. Any spectra demonstrating signs of spectral features similar to those observed in San Carlos olivine were not considered in this study and additional spectra were collected to accommodate for this elimination.

Model liquid lines of descent

To constrain the effects of fractional crystallization on magmatic Fe³⁺/ΣFe ratios, model liquid lines of descent that match the observed major element variations were generated using PetroLog3 (Danyushevsky & Plechov, 2011). The mineral-melt models that most closely replicate the natural data were chosen for each location, resulting in some variation in the models used from volcano to volcano. Individual model parameters

chosen to generate each LLD are provided in the figure captions to Fig A2-A6. If crystal fractionation is the main control on magmatic Fe redox, each model is meant to assess the extent to which Fe redox ratios may vary as a result of the relative incompatibility of Fe^{3+} in each fractionating phase. Implicit in this assessment is the assumption that fractional crystallization proceeds in a system closed to oxygen. Evidence from a global study of MORB glass suggests that closed system fractionation of olivine \pm plagioclase \pm clinopyroxene explains variations in $\text{Fe}^{3+}/\Sigma\text{Fe}$ ratios (Cottrell & Kelley, 2011). In our present study, each modeled LLD assumes a $D^{\text{Fe}^{3+}} = 0$ and a $D^{\text{Fe}^{2+}}$ that varies according to the mineral-melt models chosen, for olivine \pm clinopyroxene \pm plagioclase fractionation. Magnetite mineral-melt models use a non-zero $D^{\text{Fe}^{3+}}$ that depend upon the composition of the melt. Each model was generated using a starting composition from a measured sample in this study.

Agrigan

Agrigan tephra samples Agri7, Agri04, and Agri05 all contain crystals of olivine, plagioclase, clinopyroxene, and magnetite. The clasts are red-brown, rounded and slightly weathered. In tephra sample Agri04, there are occasional clay fragments present. In tephra sample Agri05, there are occasional clasts of country rock that are red in color. The largest size fraction observed in these tephra samples is ~ 0.5 cm in diameter.

The modeled LLD begins with sample Agri-04-05 as the parental composition. The model crystallizes olivine isobarically at 1 kbar, then saturates clinopyroxene at 4.3 wt% MgO and then saturates plagioclase at 4.2 wt% MgO (Fig. 3a-d, A2). The whole rock and melt inclusion data for Agrigan from the literature and this study are broadly consistent with this model and in the case of all major elements except for $\text{FeO}^{\text{actual}}$ and

$\text{Fe}_2\text{O}_3^{\text{actual}}$, the fractionation slope defined by the modeled LLD between 5-7 wt% MgO was used to correct for the effects of fractional crystallization (Electronic Appendix E). For $\text{FeO}^{\text{actual}}$ and $\text{Fe}_2\text{O}_3^{\text{actual}}$, an empirical fractionation slope constrained by the trend in the melt inclusion data from this study was used (Electronic Appendix E).

Pagan

Tephra sample Paga8 is black in color and fresh. The largest size fraction observed in this tephra sample is ~1 cm in diameter. This tephra sample contains plagioclase, olivine, and clinopyroxene. Submarine pillow basalts are vesicular and have a glassy pillow rind. Pillow interiors contain plagioclase, clinopyroxene, and olivine.

The modeled LLD begins with sample HDP1147-R06 as the parental composition. Starting at 2.5 kbar and decompressing at a constant rate of 5 bar per 1°C, the model crystallizes olivine and clinopyroxene, and then saturates plagioclase at 7.0 wt% MgO, and then magnetite at 6.5 wt% MgO (Fig. 3a-d, A3). The whole rock and melt inclusion data for Pagan from the literature and this study are broadly consistent with this model, except for TiO_2 and SiO_2 (Fig. A3). This may result from magnetite saturation too early or in too great abundance in the modeled LLD. It is also important to note that whole rock data may contain accumulated crystals that pull the whole rock compositions away from the true liquid compositions. Systematic offsets between melt inclusions and whole rock compositions in Al_2O_3 or $\text{CaO}/\text{Al}_2\text{O}_3$ variations with MgO are evidence for this phenomenon. In the case of all major elements except for TiO_2 , SiO_2 , $\text{FeO}^{\text{actual}}$ and $\text{Fe}_2\text{O}_3^{\text{actual}}$, the fractionation slope defined by the modeled LLD between 5-7 wt% MgO was used to correct for the effects of fractional crystallization (Electronic Appendix E). For TiO_2 , SiO_2 , $\text{FeO}^{\text{actual}}$ and $\text{Fe}_2\text{O}_3^{\text{actual}}$, an empirical fractionation slope constrained by

the trend in the melt inclusion and submarine glass data from this study was used (blue line on TiO₂ panel, Fig. A3; Electronic Appendix E).

Alamagan

Tephra samples Ala02 and Ala03 both contain olivine, plagioclase, clinopyroxene, and magnetite. Both tephra samples have vesiculated tephra fragments. The largest size fraction in Ala03 is ~2 cm in diameter, and ~1 cm in diameter in Ala02. Tephra sample Ala03 is altered, brown-red in color. Tephra sample Ala02 is black-brown in color.

The modeled LLD begins with sample Ala02-01 as the parental composition. Starting at 2 kbar and decompressing at a constant rate of 15 bar/°C, this model crystallizes olivine, then saturates clinopyroxene at 4.6 wt% MgO and then saturates plagioclase at 4.5 wt% MgO (Fig. 3a-d, A4). The whole rock and melt inclusion data for Alamagan from the literature and this study are broadly consistent with this model and in the case of all major elements except for FeO^{actual} and Fe₂O₃^{actual}, the fractionation slope defined by the modeled LLD between 5-7 wt% MgO was used to correct for the effects of fractional crystallization (Electronic Appendix E). For FeO^{actual} and Fe₂O₃^{actual}, an empirical fractionation slope constrained by the trend in the melt inclusion data from this study was used (Electronic Appendix E).

Guguan

Tephra samples Gug11 and Gug23-02 are black in color and are fresh. The largest size fraction in both tephra is ~0.5 cm in diameter. Both tephra samples contain crystals of olivine, plagioclase, and clinopyroxene.

The modeled LLD begins with sample SD46-1-1 as the parental composition (Stern *et al.*, 2006). Starting at 2 kbar and decompressing at a constant rate of 5 bar/°C, this model crystallizes olivine, then saturates clinopyroxene at 6.3 wt% MgO, then saturates plagioclase at 5.3 wt% MgO, and magnetite at 4.4 wt% MgO (Fig. 3a-d, A5). The whole rock and melt inclusion data for Guguan from the literature and this study are broadly consistent with this model. Some melt inclusions from this study and those from previous work have higher FeO* concentrations than do whole rock samples from Guguan, suggesting that melt inclusions from Guguan tephras frequently gain Fe. The careful screening procedures in this study eliminate any melt inclusion compositions that deviate significantly from the whole rock compositions, in order to avoid interpreting melt inclusion compositions that have experienced complicated magmatic histories in this work. Another important observation is that the model LLD does not fit the absolute variation between TiO₂ and MgO because the starting composition, chosen as such because of its elevated MgO content, happens to have higher TiO₂ than other whole rock samples from Guguan volcano. Though the line is offset from the data array, the slope of the line however is a good match. In the case of all major elements except for FeO^{actual} and Fe₂O₃^{actual}, the fractionation slope defined by the modeled LLD between 5-7 wt% MgO was used to correct for the effects of fractional crystallization (Electronic Appendix E). For FeO^{actual} and Fe₂O₃^{actual}, an empirical fractionation slope constrained by the trend in the melt inclusion data from this study was used (Electronic Appendix E).

Sarigan

Tephra sample Sari15-04 is brown in color and show signs of slight alteration. The largest size fraction observed in this tephra sample is ~0.25 cm in diameter. This tephra sample contains crystals of olivine, clinopyroxene, plagioclase, and magnetite.

The modeled LLD begins with sample Sari15-04-27 as the parental composition. Starting at 1.8 kbar and decompressing at a constant rate of 0.9 bar/°C, this model crystallizes olivine, then saturates clinopyroxene at 7.1 wt% MgO, then saturates magnetite at 6.8 wt% MgO, and then saturates plagioclase at 4.1 wt% MgO (Fig. 3a-d, A6). The whole rock and melt inclusion data for Sarigan from the literature and this study are broadly consistent with this model, with a few exceptions. While the model LLD is a good match for the variation in FeO* and TiO₂ with decreasing MgO in the compositional range of the melt inclusions in this study, whole rock compositions that extend to lower MgO concentrations are not well fit by the model. This may be because magnetite does not saturate in this model and the fractionation of plagioclase drives FeO* and TiO₂ contents to increasingly higher values, opposite to the trends observed in the natural whole rock data. If magnetite is allowed to saturate in the model, it saturates too early and the LLD is inconsistent with the natural data in the compositional range of melt inclusions in this study. Because none of our Sarigan melt inclusions have MgO < 5.0 wt%, we chose the model that better describes the compositional range of samples at higher MgO concentrations. For melt inclusion compositions in this study, in the case of all major elements except for FeO^{actual} and Fe₂O₃^{actual}, the fractionation slope defined by the modeled LLD between 5-7 wt% MgO was used to correct for the affects of fractional crystallization (Electronic Appendix E). For FeO^{actual} and Fe₂O₃^{actual}, an empirical

fractionation slope constrained by the trend in the melt inclusion data from this study was used (Electronic Appendix E).

NW Rota-1

Submarine pillows from NW Rota-1 are vesicular and have glassy pillow rinds. The pillow interiors have crystals of plagioclase, clinopyroxene, and olivine.

The modeled LLD begins with sample HD488-R11 as the parental composition. This model crystallizes olivine isobarically at 0.1 kbar, then saturates plagioclase at 7.2 wt% MgO, and then saturates clinopyroxene at 6.1 wt% MgO (Fig. 3a-d, A7). Though there is a paucity of data for NW Rota-1, the submarine glass data from this study are broadly consistent with this model and in the case of all major elements except for $\text{FeO}^{\text{actual}}$ and $\text{Fe}_2\text{O}_3^{\text{actual}}$, the fractionation slope defined by the modeled LLD between 5-7 wt% MgO was used to correct for the effects of fractional crystallization (Electronic Appendix E). For $\text{FeO}^{\text{actual}}$ and $\text{Fe}_2\text{O}_3^{\text{actual}}$, an empirical fractionation slope constrained by the trend in the submarine glass data from this study was used (Electronic Appendix E).

Northern and Southern Mariana Trough

Northern Mariana trough glasses discussed here were provided only as chipped glass fragments. These glass fragments are fresh and some are vesicular. Southern Mariana trough pillow basalts are vesicular and have glassy pillow rinds. The interior of some vesicle walls are lined with small sulfide crystals. The pillow interiors have olivine \pm plagioclase \pm clinopyroxene.

Northern Mariana trough samples range in H_2O contents, from 0.5 to 2.5 wt% (Fig. 4d). Water effects magmatic differentiation by suppressing the saturation of plagioclase and clinopyroxene and parental magmas with the same major element

composition but different H₂O concentrations may have different model LLDs (e.g., Lytle *et al.*, 2013). However, the major element variations in the Mariana trough samples are similar and so will be described by a single LLD. The modeled LLD begins with sample 80-1-3 from Stolper and Newman (1994) as the parental composition. This model crystallizes olivine isobarically at 1.5 kbar, then saturates plagioclase at 8.5 wt% MgO, then saturates clinopyroxene at approximately 6.1 wt% MgO, then saturates magnetite at 3.9 wt% MgO (Fig. 3e-h). The submarine glass data from this study are broadly consistent with this model and in the case of all major elements except for FeO^{actual} and Fe₂O₃^{actual}, the fractionation slope defined by the modeled LLD between 5-7 wt% MgO was used to correct for the effects of fractional crystallization (Electronic Appendix E). For FeO^{actual} and Fe₂O₃^{actual}, an empirical fractionation slope constrained by the trend in the submarine glass data from this study was used (Electronic Appendix E).

Diffusive re-equilibration of melt inclusions

To assess whether melt inclusion suites in this study are significantly changed by diffusive re-equilibration, we compare the trace element variability recorded in suites of melt inclusions from Sarigan, Agrigan, and Alamagan volcanoes to submarine glasses from the southern Mariana trough (Fig. A10; i.e., Cottrell *et al.*, 2002, Kent 2008). There is a simple relationship between the variability in trace element compositions within a population of basaltic glasses and the bulk partition coefficient of the element (peridotite/melt); more incompatible elements show greater dynamic range in concentration (Hoffman, 1988). The same correlations should be recorded in suites of melt inclusions if diffusive re-equilibration has not significantly modified the trace

element compositions of the population. To apply this principle to subduction related magmas, we look only at elements that are not recycled from the subducting slab in the Marianas (Fig. A10, Pearce *et al.*, 2005) because addition of an element to the mantle wedge by an aqueous fluid, for example, will mask relationships between the element's abundance and variability and the partitioning behavior of the element during simple mantle melting. As expected, there is a correlation between bulk partition coefficient and the percent standard deviation of trace element concentrations measured in southern Mariana trough glasses (Fig. A10, $R^2=0.81$). Melt inclusion suites from Sarigan and Alamagan are also correlated (Fig. A10, $R^2=0.77$ and 0.70 , respectively), suggesting that their trace element concentrations are not significantly affected by diffusive re-equilibration on the timescales relevant to trace element diffusion in olivine. Melt inclusions from Agrigan volcano, however, do not show this correlation and may thus have experienced some amount of diffusive equilibration (Fig. A10).

We also examine the relationship between the sizes of melt inclusion and their major element composition and Fe redox, to test whether smaller diameter melt inclusions have re-equilibrated and larger diameter melt inclusions have not. There is no relationship between the size of melt inclusion and the major element composition, measured $\text{Fe}^{3+}/\Sigma\text{Fe}$ ratios in the inclusions, or the amount of disequilibrium between melt inclusion and olivine host (Fig. A11). The exception to this is the apparent disequilibrium between four Agrigan melt inclusions and their olivine hosts, where the smallest diameter melt inclusions appear to have undergone more post-entrapment crystallization than larger inclusions. These melt inclusions require more than 2% post-entrapment crystallization correction to reach equilibrium with its olivine host and are not considered

in this study. These results suggest either that diffusive re-equilibration (a) has not occurred in melt inclusions used in this study, or (b) has gone to completion such that even slow diffusing elements in olivine (e.g., Ca) have completely re-equilibrated in melt inclusions with 50-300 μm diameter.

Trace element heterogeneity and magma mixing

Melt inclusions and submarine glasses from a single arc volcano commonly record significant heterogeneity in trace element compositions that potentially reflect contributions and mixing between several parental magmas (e.g., Figure 9 in the main text, Fig. A13). If the parent magmas are also heterogeneous in their major element compositions, major element relationships could reflect magma mixing rather than crystal fractionation and this would introduce error into our method for calculating the $f\text{O}_2$ of primary magmas in the Marianas. Figure A13 shows the La/Yb ratios of melt inclusions and submarine glasses versus the Fo# of olivine host (for melt inclusions), SiO_2 content, measured $\text{Fe}^{3+}/\Sigma\text{Fe}$ ratios, Na_2O content, TiO_2 content, and K_2O content. The variation in La/Yb ratio versus the Fo# of the olivine host demonstrates the heterogeneity in trace element composition of melt inclusions in this study (vertical dashed line), which is greater than can be expected by simple fractionation of La from Yb during differentiation. Neither La nor Yb are thought to be a significant component slab fluids or sediment melts in the Marianas, and the variation observed here likely reflects heterogeneity in the mantle source and/or variations in the extent of melting at each location. The wide variation in La/Yb ratios (1 to >4) observed within a single suite of melt inclusions occurs in a relatively narrow range of SiO_2 concentrations (44-49 wt%).

There is no correlation between SiO_2 , Na_2O , and TiO_2 concentrations, or Fe redox ratios and La/Yb ratios, suggesting that magma is not evident in the major element compositions of the melt inclusions. The exception to this is K_2O concentrations in melt inclusions from Sarigan volcano, in which four melt inclusions with high K_2O concentrations (>0.30) also have La/Yb ratios that are a factor of two higher than the main melt inclusion population (>2.0). However, the high K_2O concentrations of these samples did not influence the choice of the fractionation model used for calculating primary melt compositions. Instead, these inclusions were corrected back to $\text{MgO} = 7.0$ wt% along a shallow slope that fit the main melt inclusion population best, creating a range in primary melt compositions used to calculate primary $f\text{O}_2$. We note that these inclusions cannot be readily distinguished from the main melt inclusion population in other major elements, and that changing the K_2O concentrations of primary melts by a factor of two does not impact calculated $f\text{O}_2$. Additionally, the same trace element heterogeneity recorded by melt inclusion populations is also recorded in submarine glasses from the Mariana trough, Pagan volcano, and NW Rota-1 volcanoes, suggesting that this observation is not simply a melt inclusion phenomenon. We conclude that the major element relationships observed in Figure 3 in the main text, as well as in Figures A2-A7 in the electronic appendix can be reasonably described by simple crystal fractionation.

Sensitivity test of primary melt model results

The method used to calculate primary melt compositions and $f\text{O}_2$ has many sources of error, uncertainty in the inputs, and calculation constraints. Here, we present the results of sensitivity tests of the model results for a subset of samples.

The calculations in the main text reference all primary melt compositions to a mantle olivine at Fo90. If the mantle is more depleted by melt extraction, as might be the case under the volcanic arc, or more fertile, the final endpoint of the calculation may reasonably be Fo91 or Fo89, respectively. Figure A12, panel a, demonstrates the sensitivity of the final calculation to mantle olivine Fo#. The difference between primary $f\text{O}_2$ calculated for arc and back-arc primary melts in equilibrium with Fo89 and Fo90 olivine, or Fo90 and Fo91 olivine, is equal to ~ 0.07 log units relative to the QFM oxygen buffer. This is an order of magnitude smaller than the observed offset between MORB, Mariana trough, and Mariana arc magmas.

The calculations in the main text correct the major element compositions of samples with MgO between 5 and 7 wt% to a reference MgO = 7.0 wt%, after which the calculation assumes that olivine is the only liquidus phase back to a melt composition in equilibrium with Fo90 olivine. For the arc samples, it is possible that clinopyroxene remains a liquidus phase to higher MgO concentrations. Figure A12, panel b shows the sensitivity of the final calculation to (1) the choice of MgO reference value (blue stars use a reference MgO = 8.0 wt%) and (2) the inclusion of clinopyroxene as a liquidus phase back to equilibrium with Fo90 olivine (pink stars include olivine and clinopyroxene as liquidus phases back to equilibrium with Fo90 olivine). Increasing the MgO reference value to 8.0 wt% increases the primary melt $f\text{O}_2$ by 0.17 log units. If clinopyroxene is included along with olivine as a liquidus

phase, primary melt fO_2 is reduced by 0.23-0.42 log units. Each of these outcomes is less than the difference of primary melt fO_2 between MORB, the Mariana trough, and the Mariana arc.

Finally, there are several model inputs that have some uncertainty associated with them. To assess the total impact of these uncertainties, we have performed a Monte Carlo error analysis. The error analysis uses an uncertainty of 0.5%, 1%, 3%, 2%, and 5% on the raw concentrations of Al_2O_3 , FeO^* , CaO , Na_2O , K_2O in the glasses associated with electron probe micro analysis and an uncertainty of 3% on the determination of $Fe^{3+}/\Sigma Fe$ ratios. It uses a 10% uncertainty in the slope of the lines used to calculate the reference compositions for these same elements to MgO7.0. We assign a 20% uncertainty to the constraints on primary melt T and P and a 15% uncertainty in the raw concentrations of Ba and La measured in the glasses by LA-ICPMS. The error simulation for calculating primary melt fO_2 was run through 100 iterations, allowing each variable to vary randomly within the limits of uncertainty described here. The 95 intermediate solutions are shown as error ellipses around the model calculations presented in the main text and shown in Figure A12, panel c. The error ellipses are much smaller than the variation between MORB, Mariana trough and Mariana arc constraints in either Ba/La ratio or primary melt fO_2 , indicating that the model results for each point are distinct.

Figure Captions

Figure A1: Example Fe- μ -XANES spectra for San Carlos olivine (green line), standard glass LW+1.0 (brown line; Cottrell *et al.*, 2009), melt inclusion sample Ala03-01 with olivine interference (solid black line) and melt inclusion sample Ala03-01 without olivine

interference (dashed black line). Inset shows the pre-edge feature for all spectra in greater detail. All spectra are normalized to an arbitrary absorption intensity of 1.0 for the region between 7205 and 7210 eV.

Figure A2: Major element variations (FeO^* , $\text{CaO}/\text{Al}_2\text{O}_3$, Al_2O_3 , and TiO_2) vs. MgO for Agrigan melt inclusions from tephtras Agri04, Agri05, and Agri07, compared to the available literature data for Agrigan melt inclusions and lavas. Large diamonds are melt inclusions used in this study. Small diamonds are olivine hosted melt inclusions that have been eliminated from this study due to $\text{Fo}_{\text{host}}\text{-Fo}_{\text{melt inclusion}}$ disequilibrium. The light gray diamonds, dotted diamonds, and open diamonds are olivine hosted melt inclusions from Kelley and Cottrell (2012), Kelley *et al.*, (2010), and Shaw *et al.* (2008), respectively. The white circles are whole rock data for tephtras collected at Agrigan volcano (Plank, unpublished data). Black circles are whole rock data for lavas collected at Agrigan volcano, compiled using GeoROC (Electronic appendix J). The black line is the Petrolog3 fractionation model, using a starting composition equal to Agri04-05 and fractionating olivine, clinopyroxene, and plagioclase at 1 kbar, using mineral melt models of Roeder and Emslie (1970) and Danyushevsky (2001), treating $\text{Fe}^{2+}/\text{Fe}^{3+}$ as a closed system (Danyushevsky & Plechov, 2011).

Figure A3: Major element variations (FeO^* , $\text{CaO}/\text{Al}_2\text{O}_3$, Al_2O_3 , and TiO_2) vs. MgO for Pagan melt inclusions from tephtra Paga8 and submarine glasses, compared to the available literature data for Pagan melt inclusions and lavas. Large squares are a melt inclusion (solid blue) and submarine glasses (checkered) used in this study. The dotted

squares and open squares are olivine hosted melt inclusions from Kelley *et al.* (2010) Shaw *et al.* (2008), respectively. Black circles are whole rock data for lavas collected at Pagan volcano, compiled using GeoROC (Electronic appendix J). The black line is the Petrolog3 fractionation model, using a starting composition equal to HDP1147-R06 and fractionating olivine, plagioclase, clinopyroxene, and magnetite at 3 kbar and decompressing at a rate of 5 bar/°C. Mineral melt models of Roeder and Emslie (1970), Danyushevsky (2001), and Ariskin and Barmina (1999) were used, treating $\text{Fe}^{2+}/\text{Fe}^{3+}$ as a closed system (Danyushevsky & Plechov, 2011).

Figure A4: Major element variations (FeO^* , $\text{CaO}/\text{Al}_2\text{O}_3$, Al_2O_3 , and TiO_2) vs. MgO for Alamagan melt inclusions from tephras Ala02 and Ala03, compared to the available literature data for Alamagan melt inclusions and lavas. Large circles are melt inclusions used in this study. Small circles are olivine hosted melt inclusions that have been eliminated from this study due to $\text{Fo}_{\text{host}}\text{-Fo}_{\text{melt inclusion}}$ disequilibrium (light green) and to elevated FeO^* relative to the literature data (dark green). The open, thick lined circles are olivine hosted melt inclusions from Shaw *et al.* (2008). The open, thin lined circles are whole rock data for tephras collected at Alamagan volcano (Plank, unpublished data). Black circles are whole rock data for lavas collected at Alamagan volcano, compiled using GeoROC (Electronic appendix J). The black line is the Petrolog3 fractionation model, using a starting composition equal to Ala02-01 and fractionating olivine, plagioclase, and clinopyroxene at 2 kbar and decompressing at a rate of 15 bar/°C. Mineral melt models of Roeder and Emslie (1970) and Danyushevsky (2001) were used, treating $\text{Fe}^{2+}/\text{Fe}^{3+}$ as a closed system (Danyushevsky & Plechov, 2011).

Figure A5: Major element variations (FeO^* , $\text{CaO}/\text{Al}_2\text{O}_3$, Al_2O_3 , and TiO_2) vs. MgO for Guguan melt inclusions from tephtras Gug11 and Gug23-02, compared to the available literature data for Guguan melt inclusions and lavas. Large hexagons are melt inclusions used in this study. Small hexagons are olivine hosted melt inclusions that have been eliminated from this study due to $\text{Fo}_{\text{host}}\text{-Fo}_{\text{melt}}$ inclusion disequilibrium (solid and checkered light yellow). The dotted hexagons, slashed hexagons, and open hexagons are olivine hosted melt inclusions from Kelley *et al.* (2010), Kelley and Cottrell (2009), and Shaw *et al.* (2008), respectively. The white circles are whole rock data for tephtras collected at Guguan volcano (Plank, unpublished data). Black circles are whole rock data for lavas collected at Guguan volcano, compiled using GeoROC (Electronic appendix J). The black line is the Petrolog3 fractionation model, using a starting composition equal to SD46-1-1 and fractionating olivine, plagioclase, clinopyroxene, and magnetite at 2 kbar and decompressing at a rate of 5 bar/ $^{\circ}\text{C}$. Mineral melt models of Roeder and Emslie (1970), Danyushevsky (2001), and Ariskin and Barmina (1999) were used, treating $\text{Fe}^{2+}/\text{Fe}^{3+}$ as a closed system (Danyushevsky & Plechov, 2011).

Figure A6: Major element variations (FeO^* , $\text{CaO}/\text{Al}_2\text{O}_3$, Al_2O_3 , and TiO_2) vs. MgO for Sarigan melt inclusions from tephra Sari15-04, compared to the available literature data for Sarigan melt inclusions and lavas. Large stars are melt inclusions used in this study. Small stars are olivine hosted melt inclusions that have been eliminated from this study due to $\text{Fo}_{\text{host}}\text{-Fo}_{\text{melt}}$ inclusion disequilibrium (light orange) and to elevated FeO^* relative to the literature data (dark orange). The dotted stars and open stars are olivine hosted melt

inclusions from Kelley *et al.* (2010) and Shaw *et al.* (2008), respectively. The white circles are whole rock data for tephras collected at Alamagan volcano (Plank, unpublished data). Black circles are whole rock data for lavas collected at Sarigan volcano, compiled using GeoROC (Electronic appendix J). The black line is the Petrolog3 fractionation model, using a starting composition equal to Sari15-04-27 and fractionating olivine, plagioclase, and clinopyroxene at 1.8 kbar and decompressing at a rate of 9 bar/°C. Mineral melt models of Roeder and Emslie (1970), Danyushevsky (2001), and (Nielsen, 1988) were used, treating $\text{Fe}^{2+}/\text{Fe}^{3+}$ as a closed system (Danyushevsky & Plechov, 2011).

Figure A7: Major element variations (FeO^* , $\text{CaO}/\text{Al}_2\text{O}_3$, Al_2O_3 , and TiO_2) vs. MgO for NW Rota-1 submarine glasses. The black line is the Petrolog3 fractionation model, using a starting composition equal to HD288-R11 and fractionating olivine, plagioclase, and clinopyroxene at 0.1 kbar. Mineral melt models of Roeder and Emslie (1970), and Danyushevsky (2001) were used, treating $\text{Fe}^{2+}/\text{Fe}^{3+}$ as a closed system (Danyushevsky & Plechov, 2011).

Figure A8: Calculated Fo# of an equilibrium olivine host for each melt inclusion included in this study, using an $\text{FeO}/\text{MgO } K_D = 0.3$ (Roeder & Emslie, 1970) vs. the measured Fo# of the olivine host. Solid black line is a 1:1 relationship. Dashed black lines represent the error envelope of the equilibrium Fo# calculation. This error envelope is calculated by propagating average analytical error for FeO^* and MgO through the equations for

calculating equilibrium Fo#. Any melt inclusion that falls below the 1:1 line is subject to the PEC correction described in the main text, until the melt inclusion composition is in equilibrium with the composition of its olivine host. Any melt inclusion composition that falls above the 1:1 line, but lies within the error envelope, is left uncorrected.

Figure A9: Plots of V vs. MgO variation for Mariana trough samples (southern Mariana trough, this study; white circles are Mariana trough data from Pearce *et al.*, 2005). The arrow shows the general expectation of the effect of magnetite fractionation on V concentrations in a magma.

Figure A10: A plot of percent standard deviation of select trace element concentrations within a population of samples versus bulk $D^{\text{perid/melt}}$ for melt inclusions from Sarigan, Agrigan, and Alamagan volcanoes, as well as submarine glasses from the southern Mariana trough. Bulk $D^{\text{perid/melt}}$ are from Cottrell *et al.*, (2002).

Figure A11: Plots of the size of melt inclusions versus CaO, $\text{Fe}^{3+}/\Sigma \text{Fe}$ ratios, and the apparent disequilibrium between melt inclusion and olivine host pairs. Melt inclusion shapes vary between circular and oblate. In the cases where the melt inclusions are oblate, the left hand panels use the short axis and the right hand panels use the long axis of the inclusions. In the bottom panels, the gray dashed line marks the position of $\text{Fo}_{\text{EQ}} - \text{Fo}_{\text{host}}$ equal to 0, or apparent equilibrium between melt inclusion and olivine host. Any melt inclusion within the gray box are those that are used in this study.

Figure A12: Plots demonstrating the results of sensitivity tests for the calculations in this study (panels a and b) and a Monte Carlo error simulation demonstrating the effects of accumulated errors on the final calculation (panel c).

Figure A13: Plots of La/Yb ratios in melt inclusions and submarine glasses versus (a) Fo# of the olivine host, (b) SiO₂, (c) Fe³⁺/ΣFe ratios, (d) Na₂O, (e) TiO₂, and (f) K₂O. The vertical dashed line emphasizes the heterogeneity in La/Yb ratio at fixed values for Fo#, SiO₂, or Fe³⁺/ΣFe ratio that is unrelated to crystal fractionation. The solid line illustrates the direction that crystal fractionation drives the variables.

References for Appendix A

- Ariskin, A. & Barmina, G. (1999). An empirical model for the calculation of spinel-melt equilibria in mafic igneous systems at atmospheric pressure: 2. Fe-Ti oxides. *Contributions to Mineralogy and Petrology* **134**, 12.
- Cottrell, E. & Kelley, K. A. (2011). The oxidation state of Fe in MORB glasses and the oxygen fugacity of the upper mantle. *Earth and Planetary Science Letters* **305**, 270-282.
- Cottrell, E., Kelley, K. A., Lanzirotti, A. & Fischer, R. A. (2009). High-precision determination of iron oxidation state in silicate glasses using XANES. *Chemical Geology* **268**, 167-179.
- Cottrell, E., Spiegelman, M. & Langmuir, C.H. (2002). Consequences of diffusive reequilibration for the interpretation of melt inclusions. *Geochemistry Geophysics Geosystems* **3**, doi: 10.1029/2001GC000205.
- Danyushevsky, L. V. (2001). The effect of small amounts of H₂O on crystallization of mid-ocean ridge and backarc basin magmas. *Journal of Volcanology and Geothermal Research* **110**, 15.
- Danyushevsky, L. V. & Plechov, P. (2011). Petrolog3: Integrated software for modeling crystallization processes. *Geochemistry Geophysics Geosystems* **12**, 1-32.

- Hoffmann, A.W. (1988). Chemical differentiation of the Earth – the relationship between mantle, continental crust, and oceanic crust. *Earth and Planetary Science Letters* **90**, 297-314.
- Kelley, K. A. & Cottrell, E. (2009). Water and the oxidation state of subduction zone magmas. *Science* **325**, 605-607.
- Kelley, K. A. & Cottrell, E. (2012). The influence of magmatic differentiation on the oxidation state of Fe in a basaltic arc magma. *Earth and Planetary Science Letters* **329-330**, 109-121.
- Kelley, K. A., Plank, T., Newman, S., Stolper, E. M., Grove, T. L., Parman, S. & Hauri, E. H. (2010). Mantle melting as a function of water content beneath the Mariana arc. *Journal of Petrology* **51**, 28.
- Kent, A.J.R. (2008). Melt inclusions in basaltic and related volcanic rocks. *Reviews in Mineralogy and Geochemistry* **69**, 273-331.
- Lytle, M., Kelley, K.A., Hauri, E.H., Gill, J.B., Papia, D., and Arculus, R.J. (2013). Tracing mantle sources and Samoan influence in the northwestern Lau back-arc basin. *Geochemistry, Geophysics, Geosystems* **13**.
- Nielsen, R. (1988). A model for the simulation of combined major and trace element liquid lines of descent. *Geochimica et Cosmochimica Acta* **52**, 27-38.
- Pearce, J., Stern, R.J., Bloomer, S.H., and Fryer, P. (2005). Geochemical mapping of the Mariana arc-basin system: Implications for the nature and distribution of subduction components. *Geochemistry, Geophysics, Geosystems* **6**, 7.
- Plank, T. (unpublished data).
- Roeder, P. L. & Emslie, R. F. (1970). Olivine-Liquid Equilibrium. *Contributions to Mineralogy and Petrology* **29**, 15.
- Shaw, A. M., Hauri, E. H., Fischer, E. H., Hilton, D. R. & Kelley, K. A. (2008). Hydrogen isotopes in Mariana arc melt inclusions: Implications for subduction dehydration and the deep-Earth water cycle. *Earth and Planetary Science Letters* **275**, 138-145.
- Stern, R. J., Kohut, E. J., Bloomer, S. H., Leybourne, M. I., Fouch, M. & Vervoort, J. (2006). Subduction factory processes beneath the Guguan cross-chain, Mariana arc: No role for sediments, are serpentinites important? *Contributions to Mineralogy and Petrology* **151**, 1711-1738.
- Stolper, E. and Newman, S. (1994). The role of water in the petrogenesis of Mariana trough magmas. *Earth and Planetary Science Letters* **121**, 392-325.

Figure A1

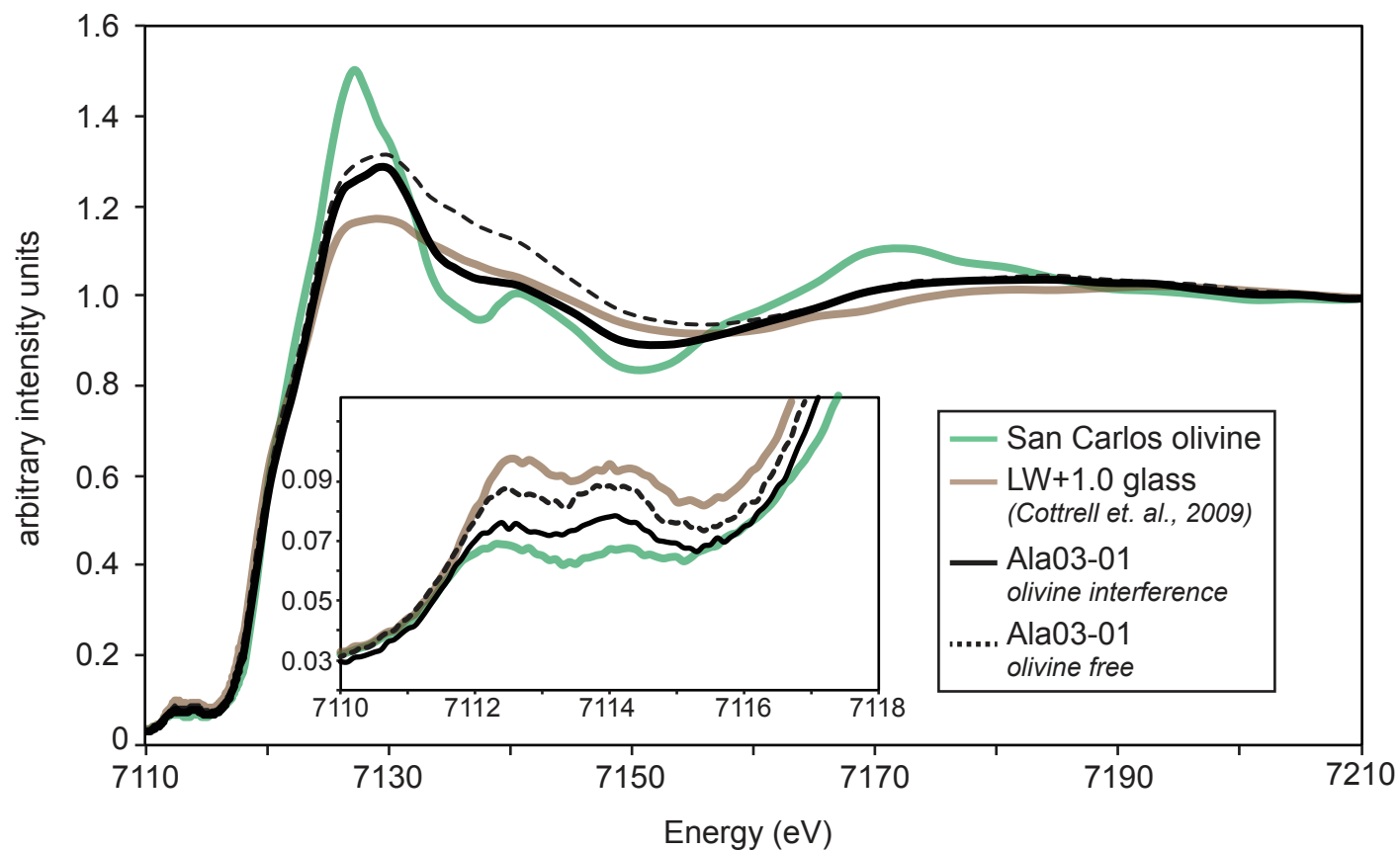


Figure A2

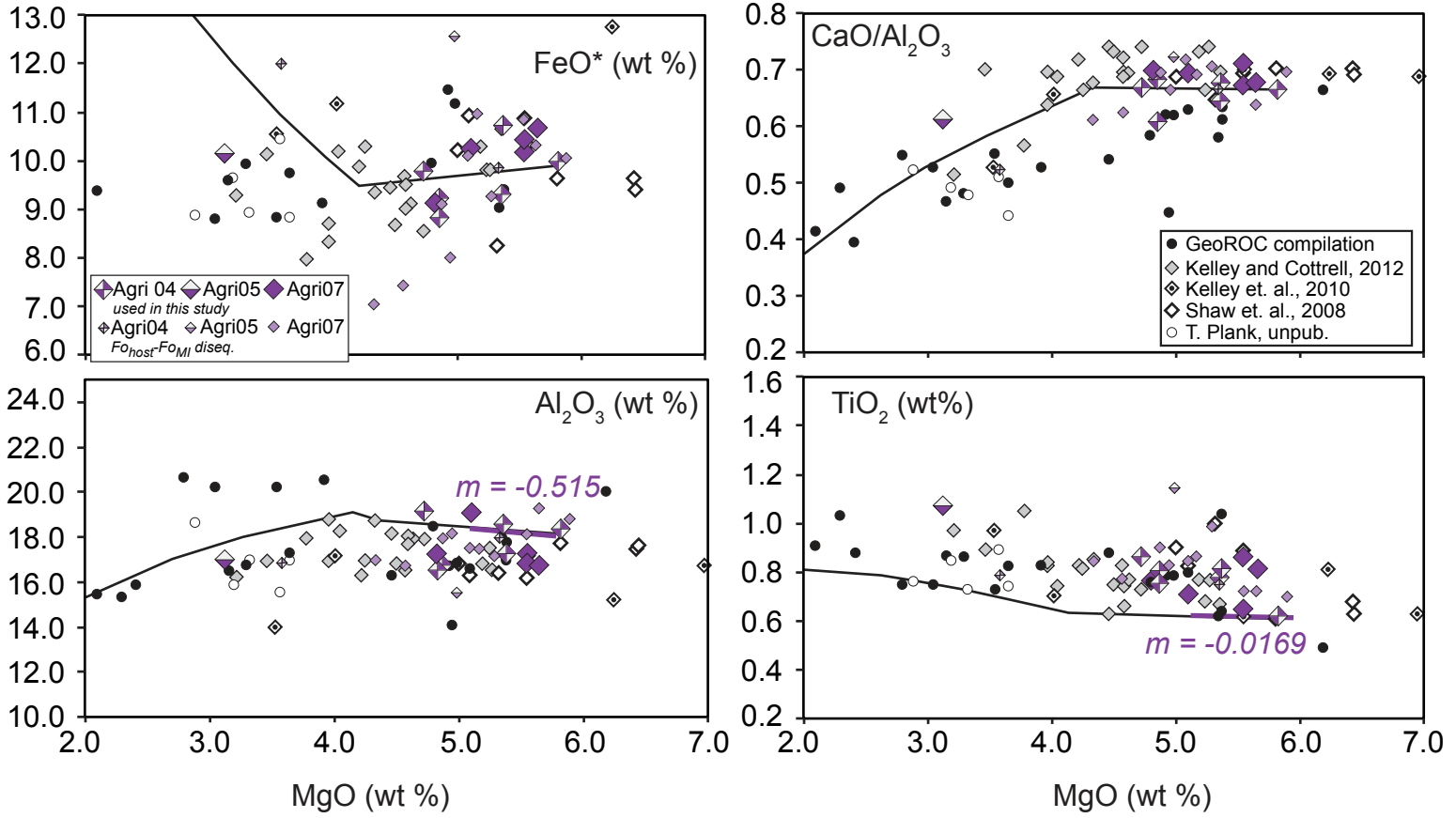


Figure A3

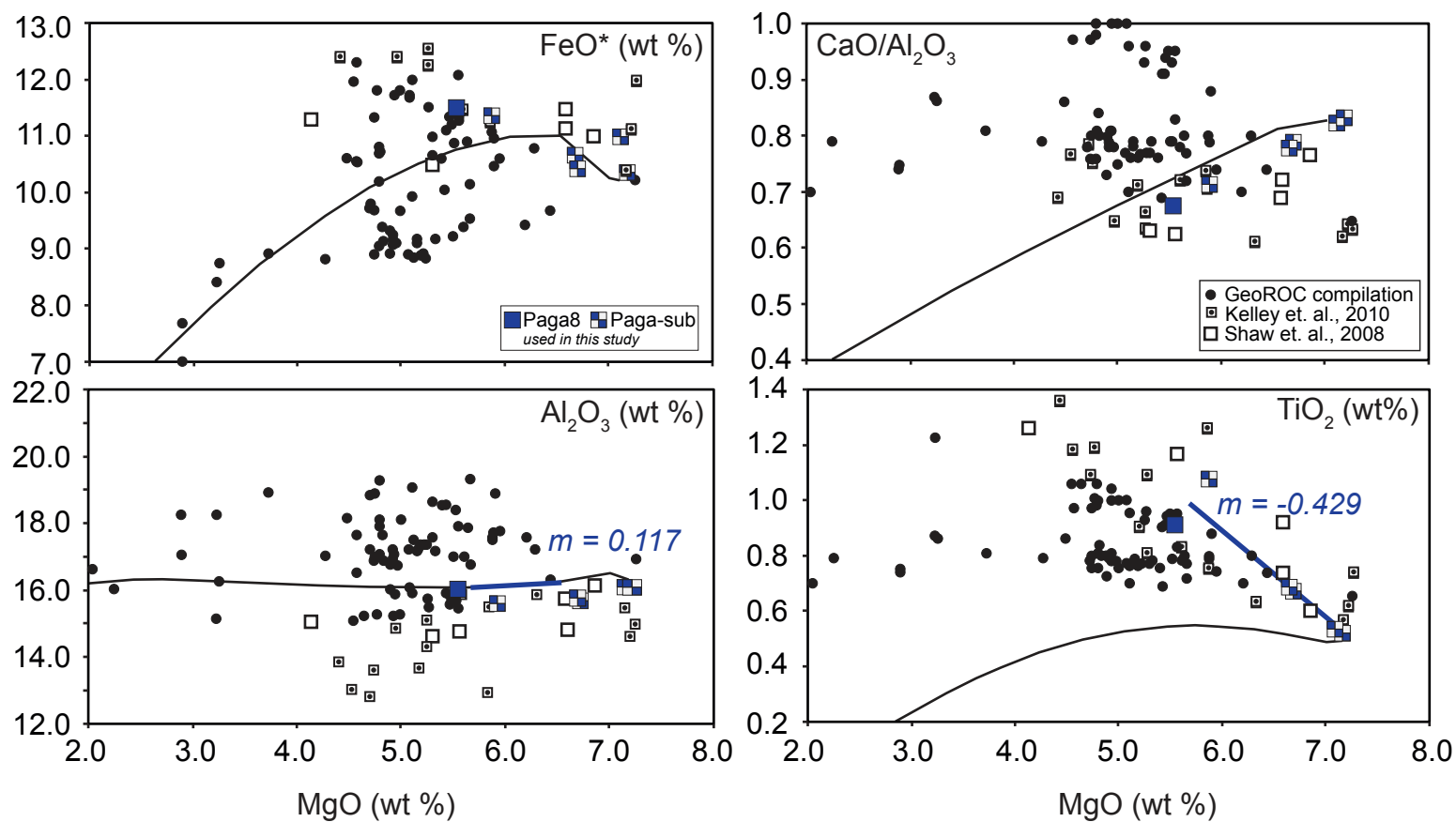


Figure A4

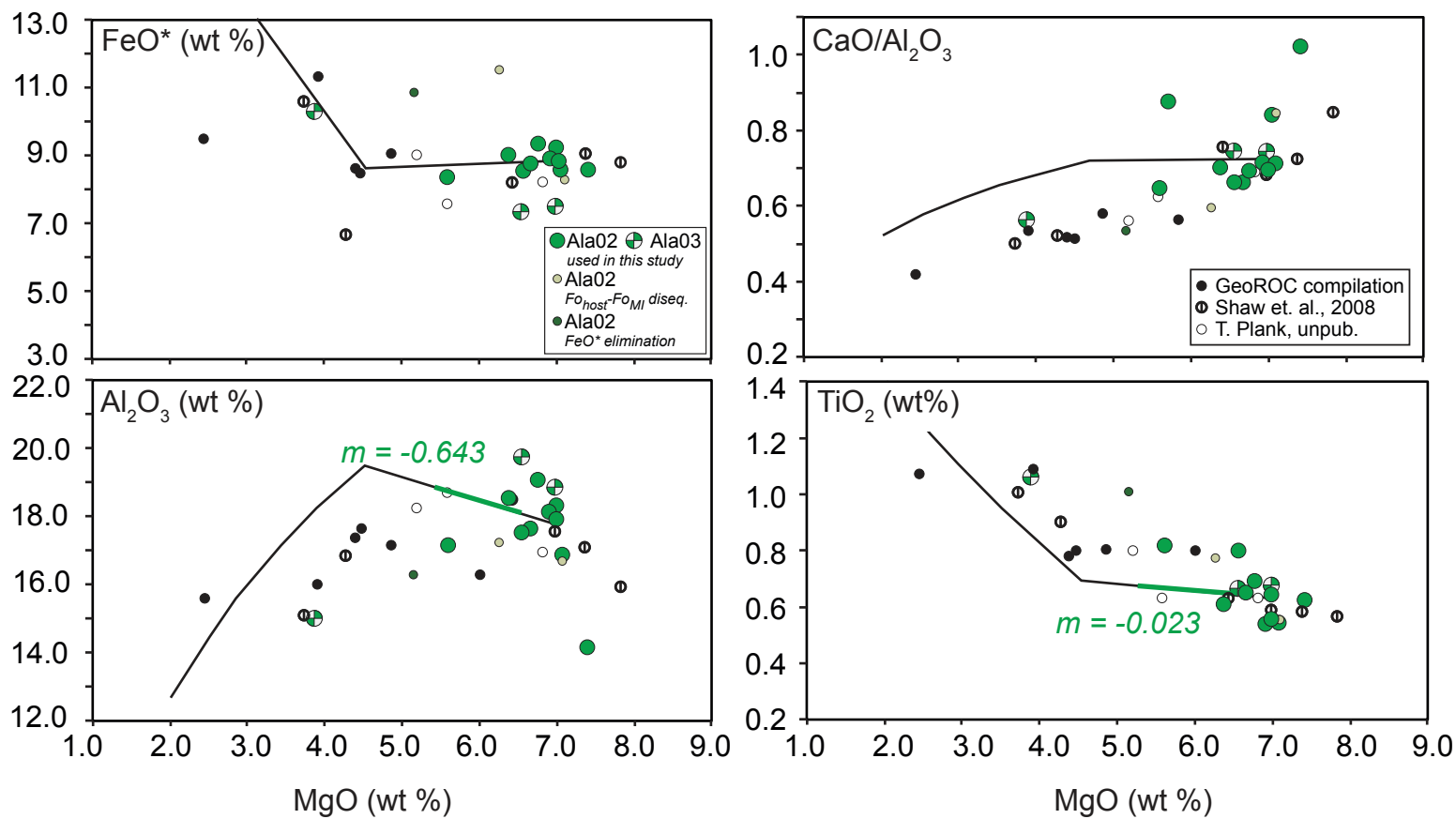


Figure A5

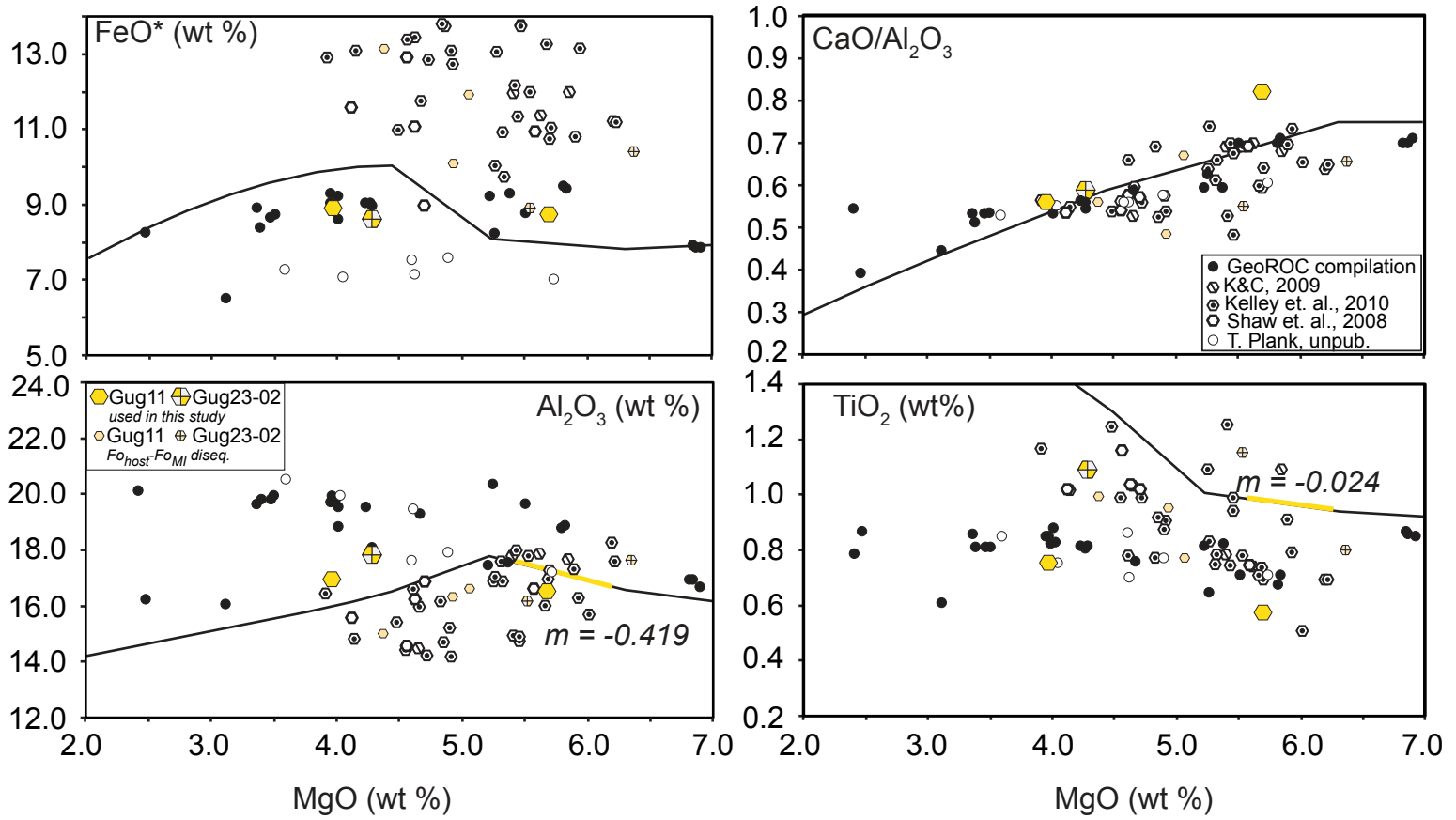


Figure A6

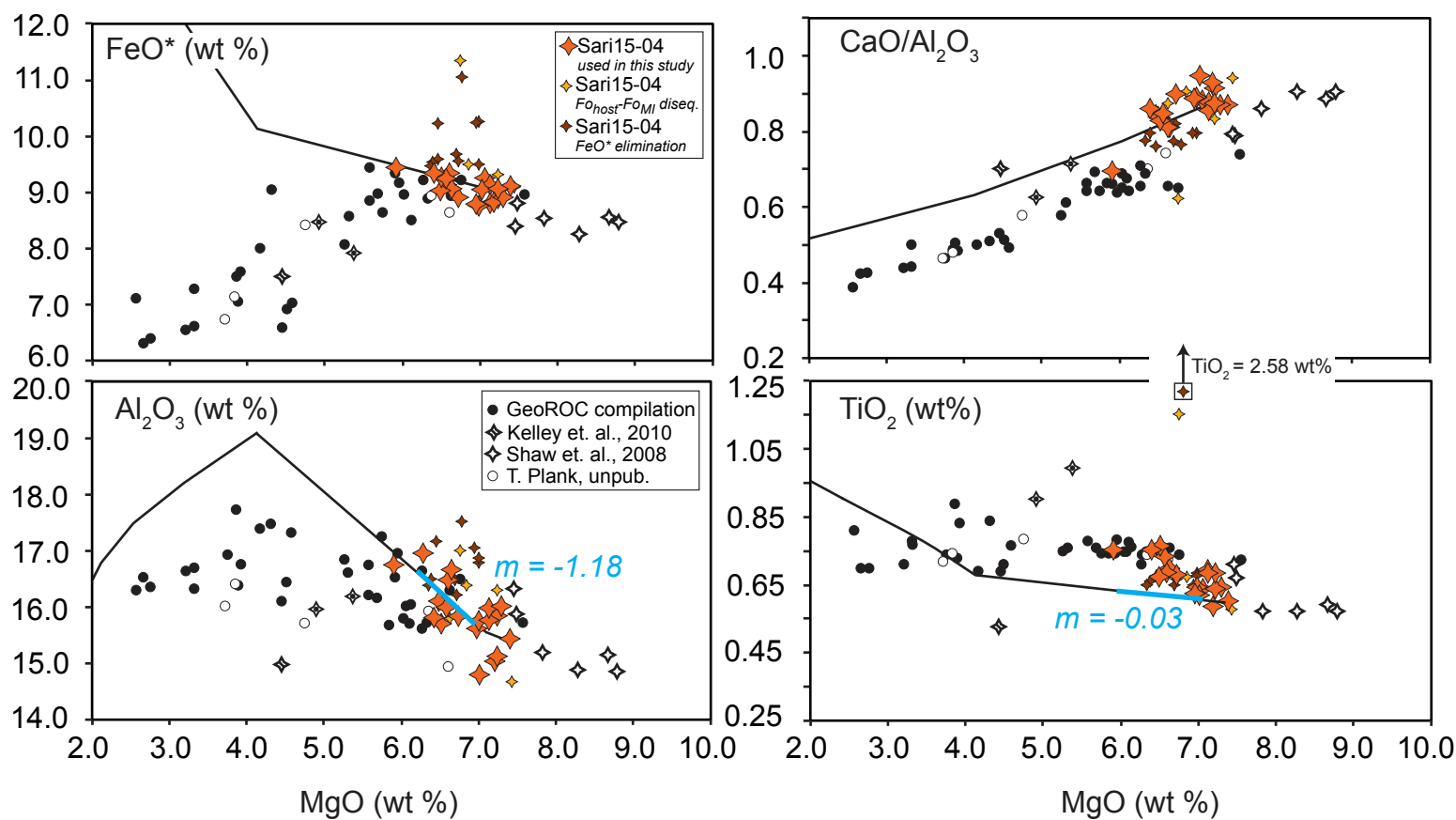


Figure A7

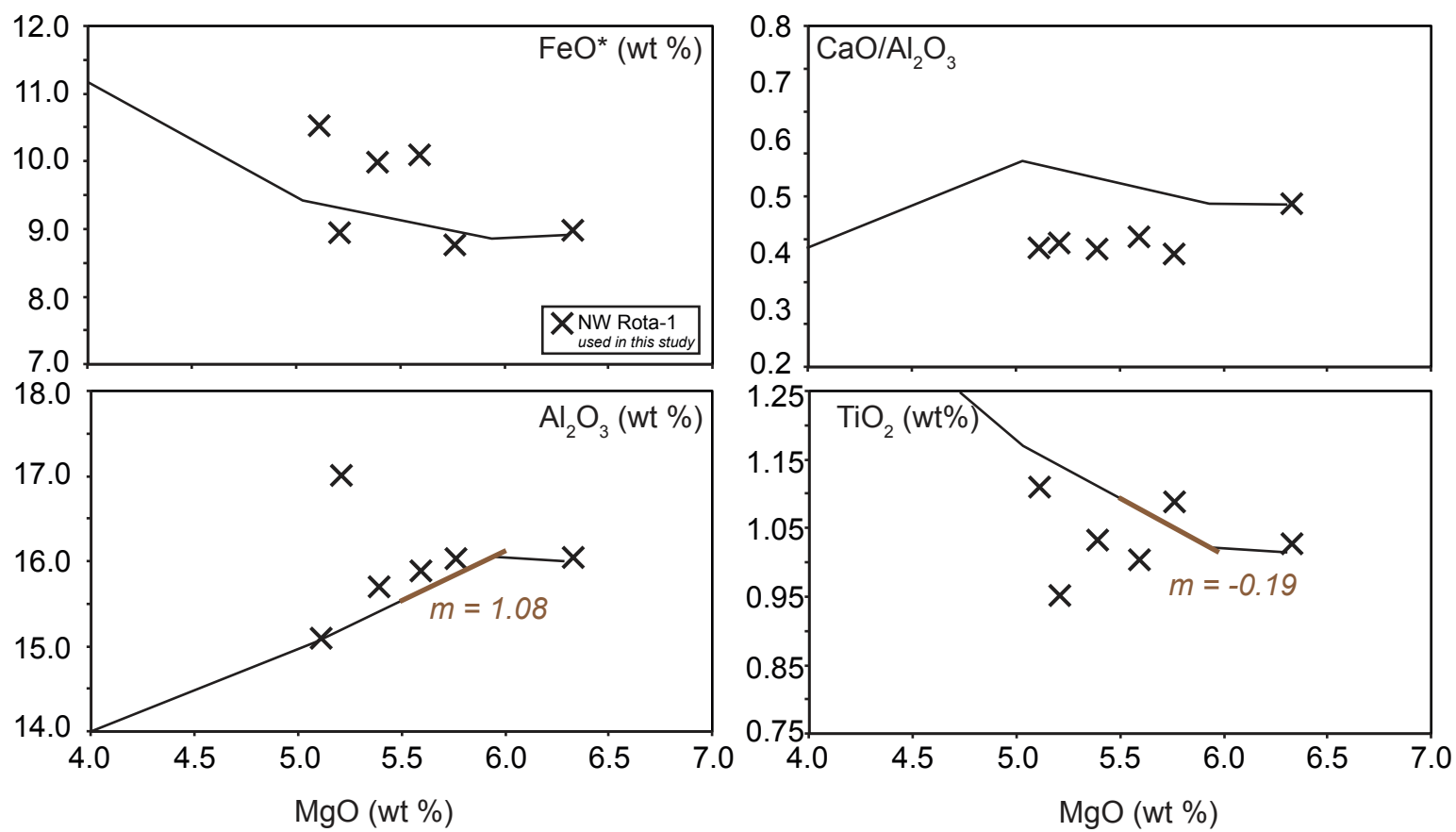
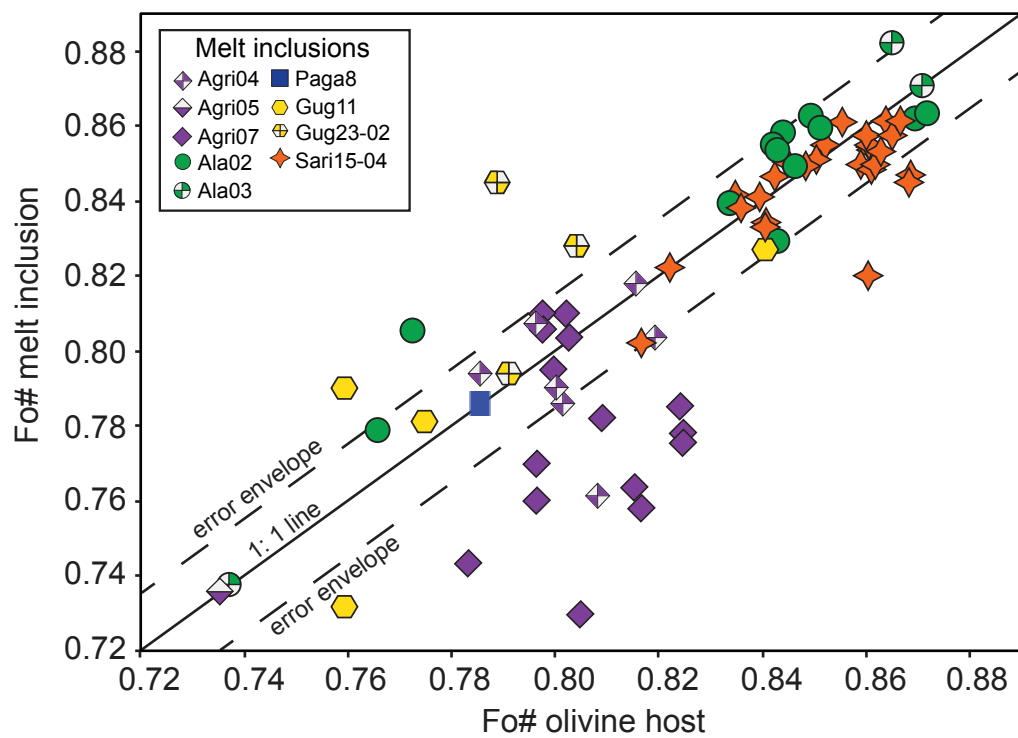


Figure A8



Brounce, Kelley and Cottrell

Figure A9

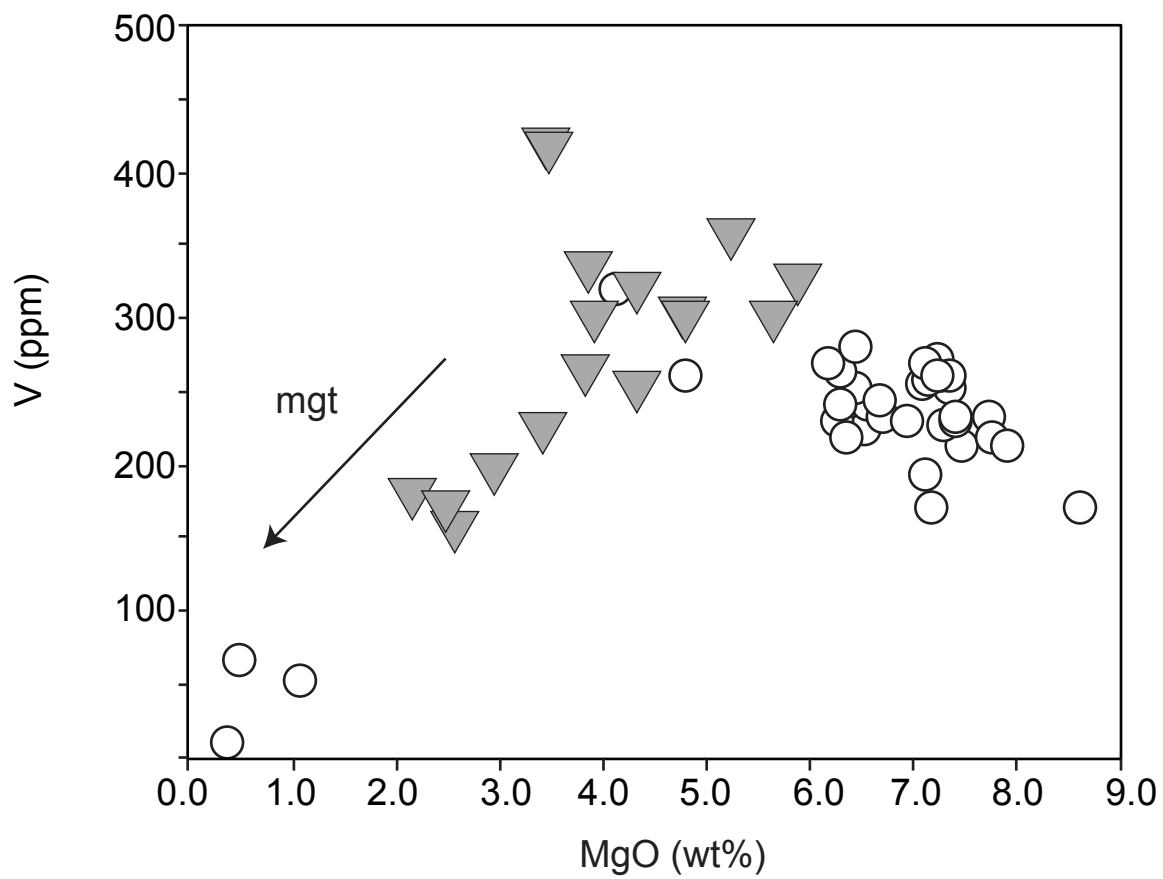


Figure A10

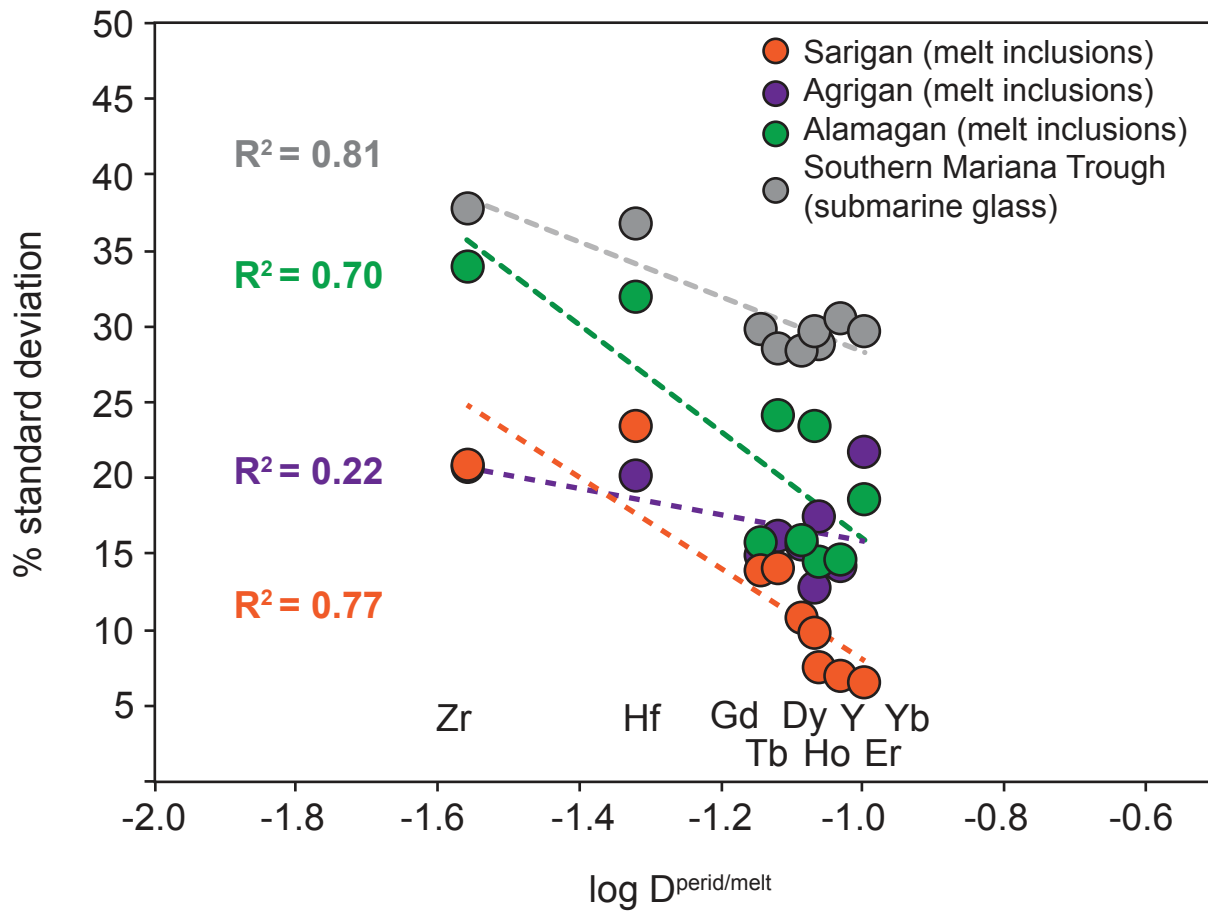


Figure A11

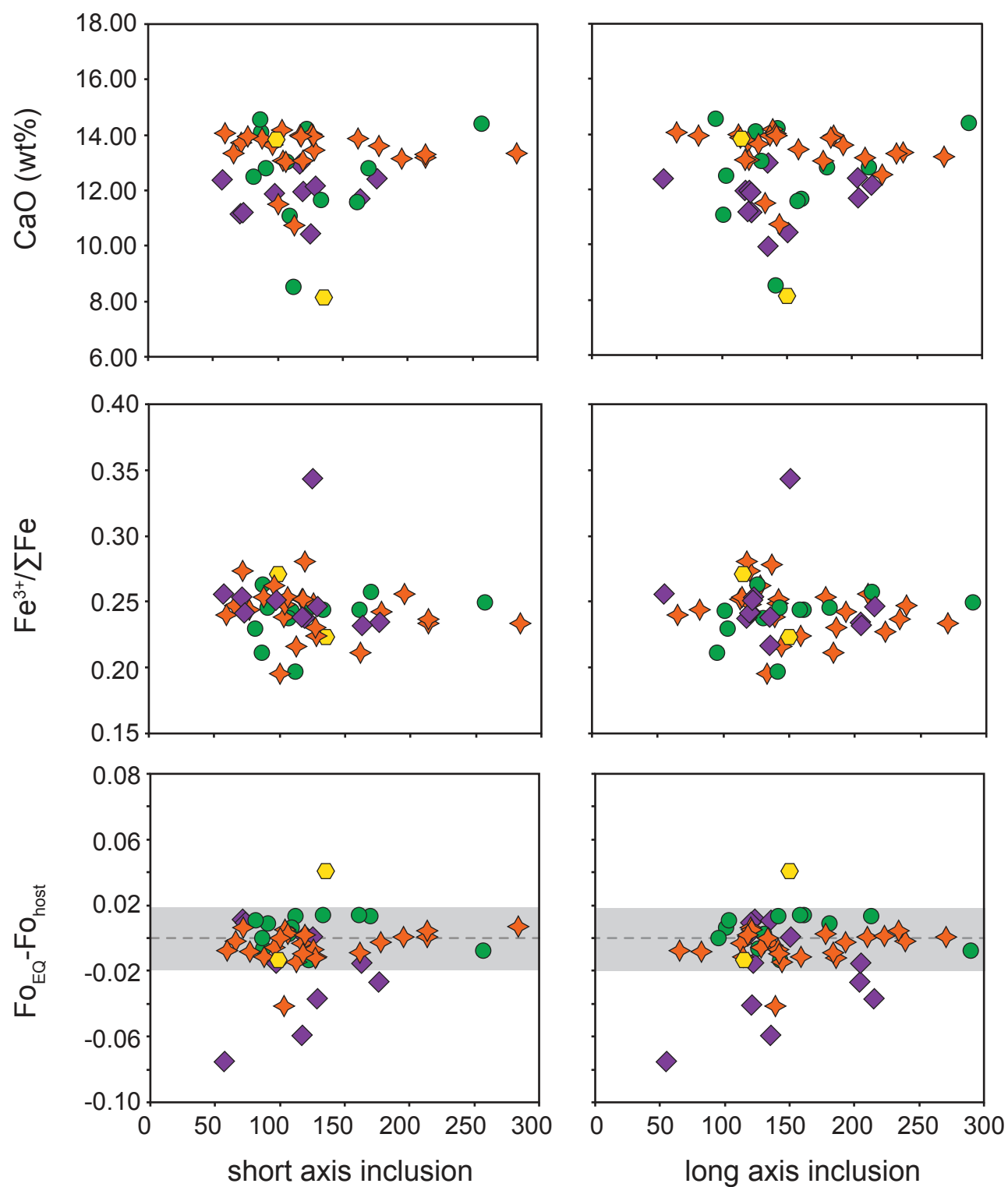
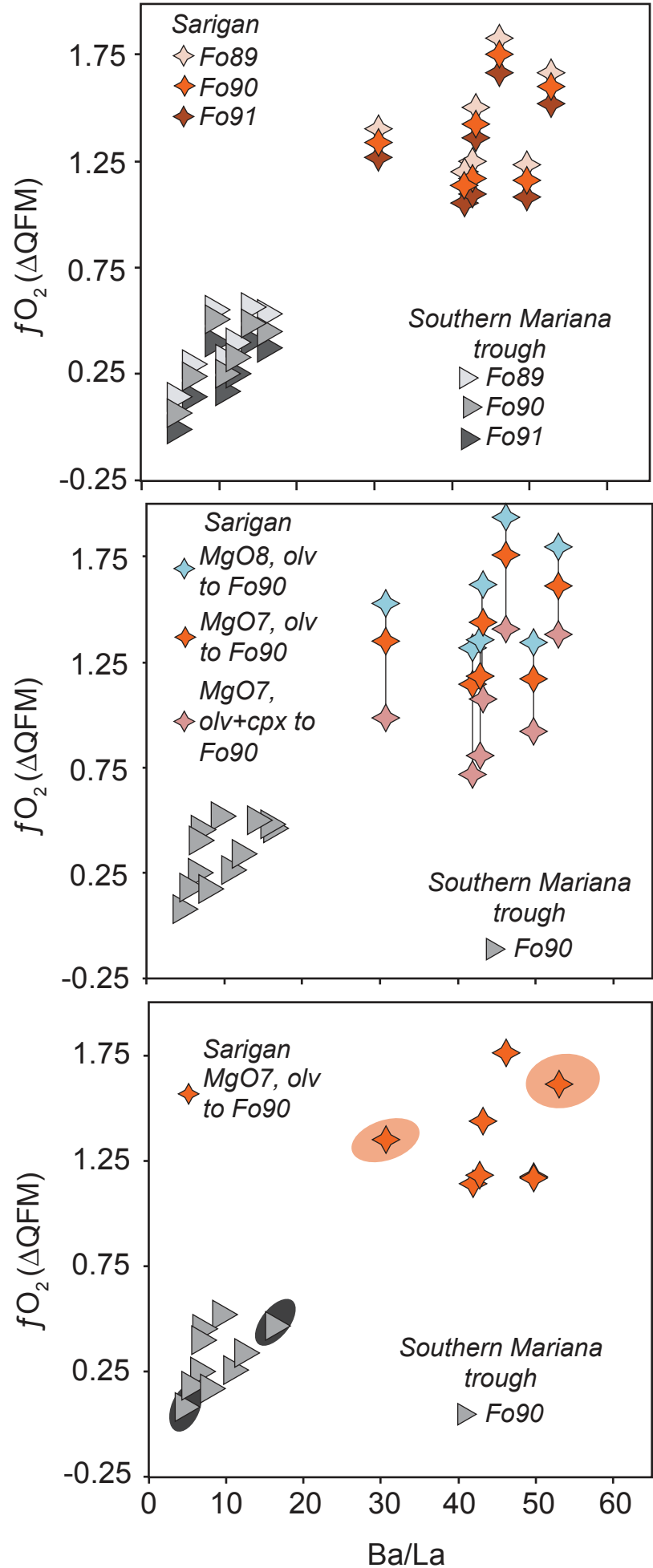


Figure A12



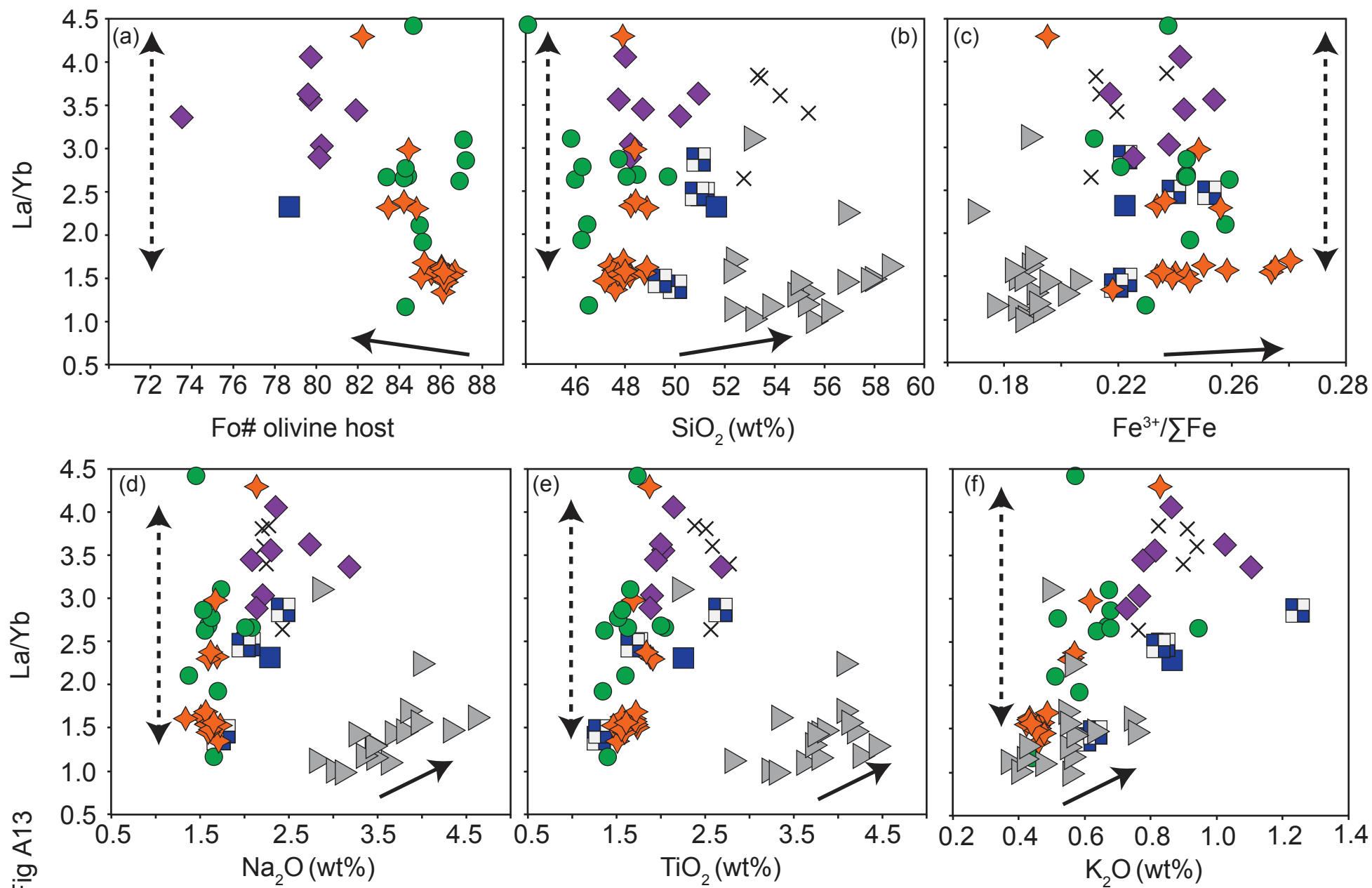


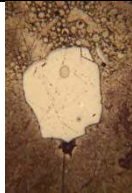













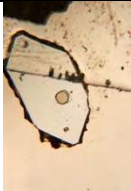
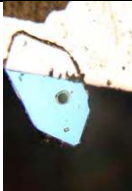
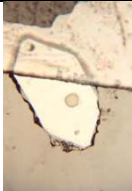
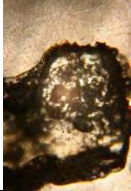
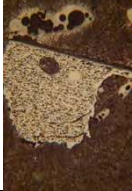

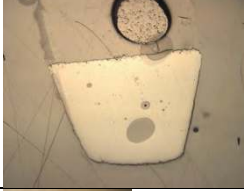
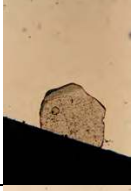








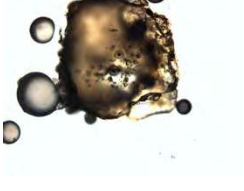
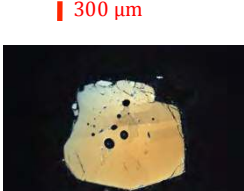

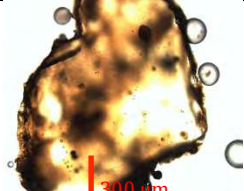

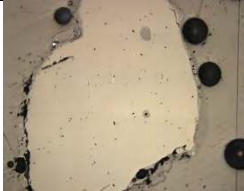




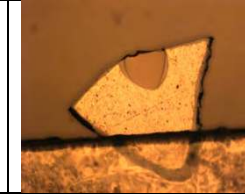
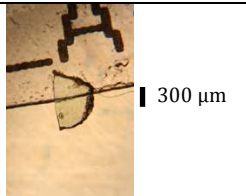
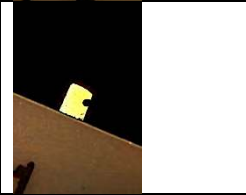

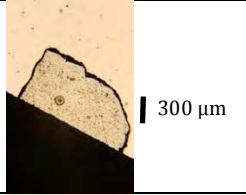
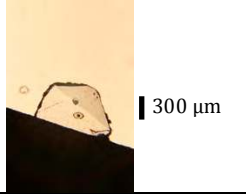
Fig A13

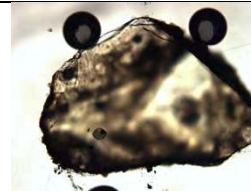
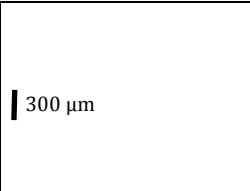
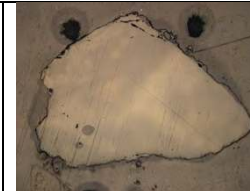

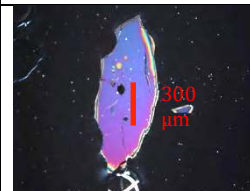

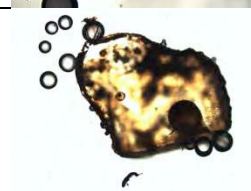
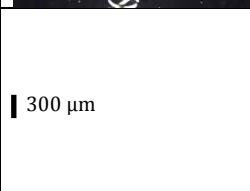
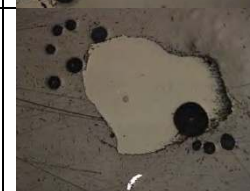

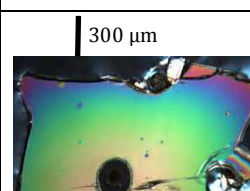
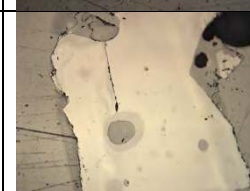

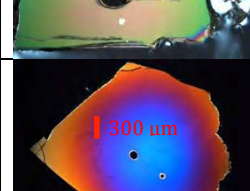
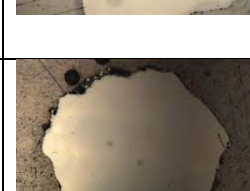
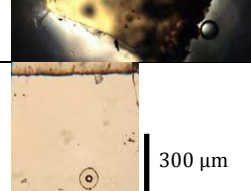
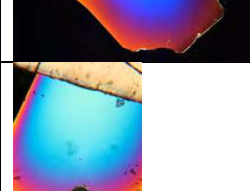


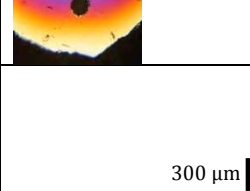

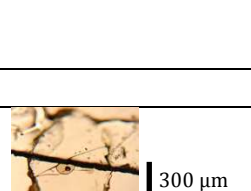


Electronic Appendix K: Photomicrographs of melt inclusions to accompany the manuscript, “ $\text{Fe}^{3+}/\Sigma\text{Fe}$ in Mariana Arc basalts and primary fO_2 ”.

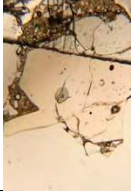
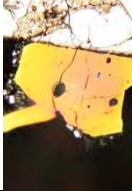
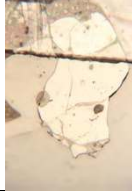

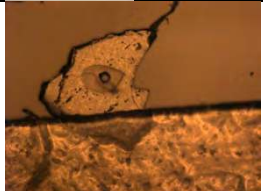

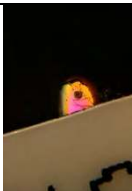



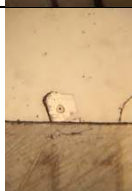
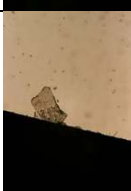






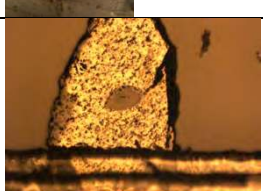
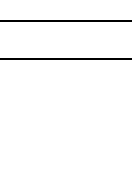
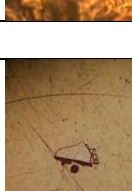
| Sample | Plane polarized | Cross polarized | Reflected |
|----------------|---|---|---|
| Sarigan | | | |
| Sari15-04-01 |  300 μm |  |  |
| Sari15-04-03 |  300 μm |  | |
| Sari15-04-04 |  300 μm |  | |
| Sari15-04-07 |  300 μm |  | |
| Sari15-04-10 |  300 μm |  | |
| Sari15-04-11 |  300 μm |  |  |
| Sari15-04-13 |  300 μm |  | |

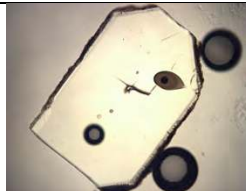
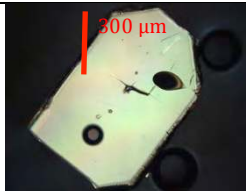


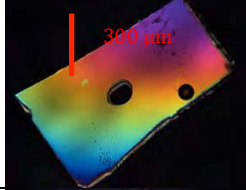

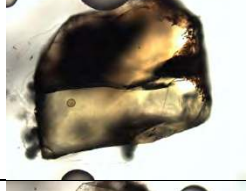


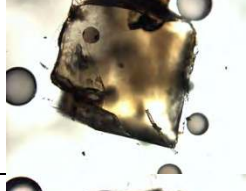
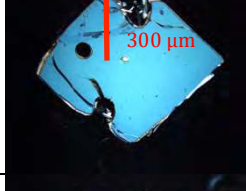

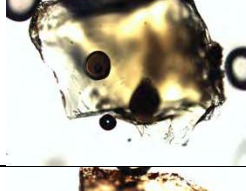
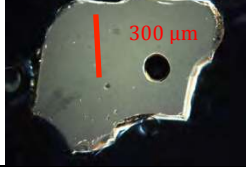

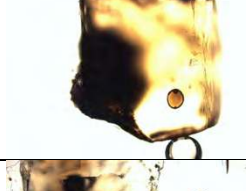
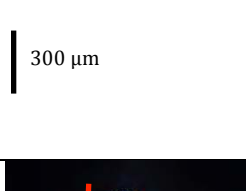

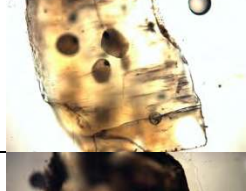


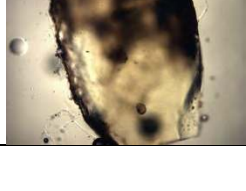


| | | | | | |
|--------------|---|--------|---|--|---|
| Sari15-04-15 |  | 300 μm |  | | |
| Sari15-04-17 |  | 300 μm |  | | |
| Sari15-04-18 |  | 300 μm |  | | |
| Sari15-04-19 |  | 300 μm |  | | |
| Sari15-04-21 |  | 300 μm |  | | |
| Sari15-04-22 |  | 300 μm |  | | |
| Sari15-04-23 |  | 300 μm |  | | |
| Sari15-04-24 |  | 300 μm |  | |  |

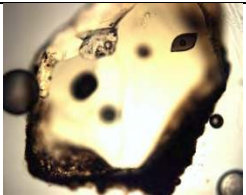
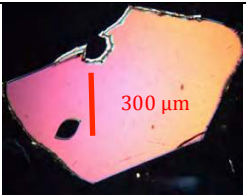
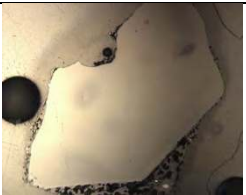
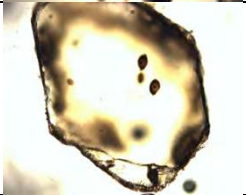


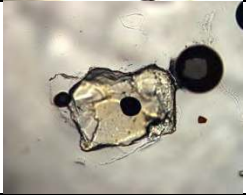
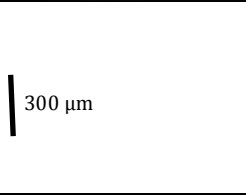


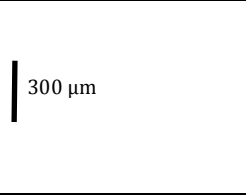

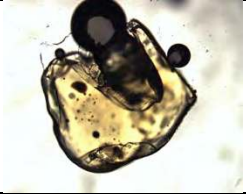
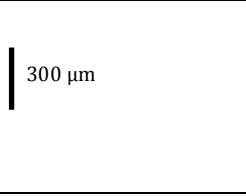


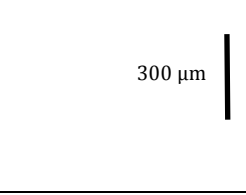


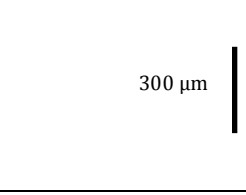
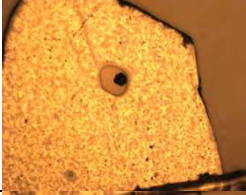

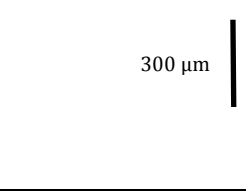
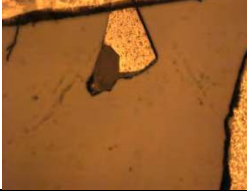
| | | | |
|--------------|---|---|---|
| Sari15-04-25 |  300 μm |  |  |
| Sari15-04-27 |  | |  300 μm |
| Sari15-04-28 |  300 μm | |  |
| Sari15-04-29 |  300 μm |  |  |
| Sari15-04-30 |  300 μm |  |  |
| Sari15-04-31 |  300 μm |  |  |
| Sari15-04-32 |  |  300 μm |  |
| Sari15-04-33 |  300 μm |  |  |

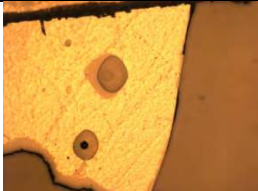
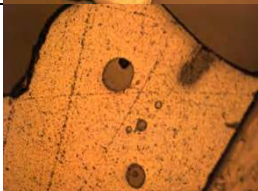
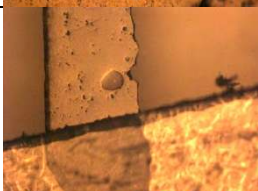

| | | | |
|------------------------|---|---|--|
| Sari15-04-34 |  |  |  |
| Sari15-04-35 |  |  |  |
| Sari15-04-36 | |  |  |
| <i>Alamagan</i> | | | |
| Ala02-01 | <i>No photos</i> | | |
| Ala02-02 | <i>No photos</i> | | |
| Ala02-03 | <i>No photos</i> | | |
| Ala02-04 |  |  |  |
| Ala02-05 |  |  |  |
| Ala02-06 |  |  |  |
| Ala02-07 |  |  |  |
| Ala02-08 |  |  |  |

| | | | |
|----------------------|---|---|--|
| Ala02-09 |  |  |  |
| Ala02-11 |  |  |  |
| Ala02-12 |  |  |  |
| Ala02-15 |  |  |  |
| Ala02-16 |  |  |  |
| Ala03-01 |  |  |  |
| Ala03-08 |  |  |  |
| <i>Guguan</i> | | | |
| Gug23-02-01 |  |  |  |

| | | | |
|-----------------------|---|---|---|
| Gug23-02-03 |  |  |  |
| Gug23-02-04 | |  |  |
| Gug11-02 |  |  |  |
| Gug11-04 |  |  |  |
| Gug11-05 |  |  |  |
| Gug11-06 |  |  |  |
| Gug11-08 | |  |  |
| <i>Pagan</i> | | | |
| Paga8-02 | |  |  |
| <i>Agrigan</i> | | | |
| Agri07-01 | <i>No photos</i> | | |
| Agri07-04 | <i>No photos</i> | | |

| | | | |
|-----------|---|---|---|
| Agri07-05 |  |  |  |
| Agri07-06 |  |  |  |
| Agri07-07 |  |  |  |
| Agri07-09 |  |  |  |
| Agri07-10 |  |  |  |
| Agri07-11 |  |  |  |
| Agri07-12 |  |  |  |
| Agri07-13 |  |  |  |

| | | | |
|-----------|---|---|---|
| Agri07-14 |  |  |  |
| Agri07-15 |  |  |  |
| Agri05-01 |  |  |  |
| Agri05-04 |  |  |  |
| Agri04-03 |  |  |  |
| Agri04-05 |  |  |  |
| Agri04-07 |  |  |  |
| Agri04-11 |  |  |  |

| | | | |
|-----------|--|-------------------|---|
| Agri04-12 | | 300 μm |  |
| Agri04-13 | | 300 μm |  |
| Agri04-14 | | 300 μm |  |
| Agri04-15 | | 300 μm |  |